5-1-2017

Analysis of the Temporal Response of Coupled Asymmetrical Zero-Power Subcritical Bare Metal Reactor Systems

Kimberly Lynn Klain
University of Nevada, Las Vegas, mtbher@gmail.com

ANALYSIS OF THE TEMPORAL RESPONSE OF COUPLED ASYMMETRICAL

ZERO-POWER SUBCRITICAL BARE METAL REACTOR SYSTEMS

By

Kimberly Lynn Klain

Bachelor of Science - Mechanical Engineering
University of Nevada, Las Vegas
2006

Master of Science - Materials and Nuclear Engineering
University of Nevada, Las Vegas
2009

A dissertation submitted in partial fulfillment
of the requirements for the

Doctor of Philosophy - Mechanical Engineering

Department of Mechanical Engineering
Howard R. Hughes College of Engineering
The Graduate College

University of Nevada, Las Vegas
May 2017

Dissertation Approval

The Graduate College
The University of Nevada, Las Vegas

May 8, 2017

This dissertation prepared by

Kimberly Lynn Klain

entitled

Analysis of the Temporal Response of Coupled Asymmetrical Zero-Power Subcritical Bare Metal Reactor Systems

is approved in partial fulfillment of the requirements for the degree of

Doctor of Philosophy - Mechanical Engineering
Department of Mechanical Engineering

William Culbreth, Ph.D.
Examination Committee Chair

Alexander Barzilov, Ph.D.
Examination Committee Member

Yi-Tung Chen, Ph.D.
Examination Committee Member

Brendan O'Toole, Ph.D.
Examination Committee Member

Steen Madsen, Ph.D.
Graduate College Faculty Representative

Kathryn Hausbeck Korgan, Ph.D.
Graduate College Interim Dean

Abstract

The behavior of symmetrical coupled-core systems has been extensively studied, yet there is a dearth of research on asymmetrical systems due to the increased complexity of the analysis of such systems. In this research, the multipoint kinetics method is applied to asymmetrical zero-power, subcritical, bare metal reactor systems. Existing research on asymmetrical reactor systems assumes symmetry in the neutronic coupling; however, it will be shown that this cannot always be assumed. Deep subcriticality adds another layer of complexity and requires modification of the multipoint kinetics equations to account for the effect of the external neutron source. A modified set of multipoint kinetics equations is derived with this in mind. Subsequently, the Rossi-alpha equations are derived for a two-region asymmetrical reactor system.

The predictive capabilities of the radiation transport code `MCNP6` for neutron noise experiments are shown in a comparison to the results of a series of Rossi-alpha measurements performed by J. Mihalczo utilizing a coupled set of symmetrical bare highly-enriched uranium (HEU) cylinders. The `ptrac` option within `MCNP6` can generate time-tagged counts in a cell (list-mode data). The list-mode data can then be processed similarly to measured data to obtain values for system parameters such as the dual prompt neutron decay constants observable in a coupled system. The results from the `ptrac` simulations agree well with the historical measured values.

A series of case studies are conducted to study the effects of geometrical asymmetry in the coupling between two bare metal HEU cylinders. While the coupling behavior of symmetrical systems has been reported on extensively, that of asymmetrical systems remains sparse. In particular, it appears that there has been no previous research in obtaining the coupling time constants for asymmetrically-coupled systems. The difficulty in observing such systems is due in part to the

inability to determine the individual coupling coefficients from measurement: unlike the symmetrical cases, only the product of the values can be obtained. A method is proposed utilizing `MCNP 6` tally ratios to separate the coupling coefficients for such systems.

This work provides insight into the behavior of asymmetrically-coupled systems as the separation distance between the two cores is changed and also as the asymmetry is increased. As the separation distance increases, the slower observable prompt neutron decay constant increases in magnitude while the faster decay constant decreases. The coupling time constants are determined from the measured decay constants. As the separation distance increases, both coupling coefficients decrease as expected. As the asymmetry increases, the difference between the faster and slower decay constants and between the coupling time constants increases as expected.

Based on these findings, an effective computational method utilizing `MCNP 6` and the Rossi-alpha technique can be applied to the prediction of asymmetrical coupled system measurements.

Acknowledgements

There have been many individuals that have supported me along my path towards the completion of my dissertation research. I would like to first thank Dr. Denis Beller for seeing the potential in me and for providing initial guidance and support. I would also like to thank Dr. William Culbreth for taking over as my advisor after Dr. Beller's retirement.

I am especially grateful to Drs. Avneet Sood and William Myers of Los Alamos National Laboratory for taking me on as a graduate research assistant and providing me mentorship during my tenure there. I am also grateful for the help and guidance of others in the XCP-3 and NEN-2 groups, including Brian Kiedrowski (now with the University of Michigan), Jesson Hutchinson, Joetta Goda, Rene Sanchez, Theresa Cutler, Travis Grove, Geordie McKenzie, and anyone else I may have forgotten to list.

I would like to thank my parents for their support and encouragement all these years. They never lost faith that I could succeed at whatever I put my mind to. I am incredibly grateful to my sister, Katie - my cheerleader, my best friend, my constant supporter. Thank you for everything (but I am still not a rocket scientist)!

Finally, I would like to thank my amazing husband, Kyle, for his patience and support during these last few years. There were times when I wanted to throw in the towel, but he provided me the push to continue and complete my work.

Table of Contents

List of Tables

List of Figures

Chapter 1

Introduction

Nuclear reactor systems vary widely in geometry, material composition, energy spectra, and many other properties, requiring different levels of detail to accurately be described. Multipoint kinetics allow a system to be divided into macroscopic regions that can be individually described by point-kinetics-like equations that include an extra term to describe the transfer of neutrons between regions. This method can be applied to systems that have regional variations in neutron flux such as large power reactors or systems of coupled reactors separated by some finite distance. In this research, the multipoint kinetics equations are derived from the neutron transport equation with a modification that accounts for the external neutron source for a more accurate representation of subcritical systems.

Reactor noise experiments, which measure the statistical fluctuations of the neutron population, are becoming increasingly important for fields of study such as special nuclear material (SNM) detection for treaty verification in which nondestructive assay is essential. The Rossi-alpha method, a measurement technique that analyzes the time response of a system, was chosen for the present analysis due to its simplicity in execution. The Rossi-alpha equations for both a symmetrical and an asymmetrical two-region system are derived, revealing the sum-of-two-exponentials response of the system.

This research focuses on a spatial problem that has had little attention: that of asymmetrical loosely-coupled cores. In particular, it applies the multipoint kinetics method to small, bare metal systems characterized by fast neutrons; i.e., neutrons having energies of 1 keV to 10 MeV. Such

systems are used to perform benchmark measurements that aid in the development of radiation transport codes and for nuclear data validation. "Loosely-coupled" refers to the fact that while each individual core or region in a system operates almost independently, there is some small amount of neutronic coupling between the regions that affects the overall response of the system. These systems are characterized by the presence of multiple observable prompt neutron decay constants. One of the challenges with such systems is the measurement of the prompt neutron decay constants at higher levels of subcriticality, even for systems described by single-point kinetics. As a system becomes more subcritical, the magnitude of the prompt neutron decay constant(s) increases and becomes more difficult to observe. Part of this research is devoted to observing those faster decay constants within simulated data that mimic measured data. The ability to simulate list-mode data (the time and location of a detection event) allows for a more accurate predictive tool to be developed that can help in the design of reactor noise experiments and in the determination of the optimum measurement parameters. The data are analyzed using the Rossi-alpha method with the post-processing code `MPKRA` developed for this research. The limitations of current measurement capabilities will be explained. Finally, the limits of the multipoint kinetics model and the point at which the single-point kinetics regime is reached will be shown using simulated experiments.

The computational capabilities will be tested against measurements to be performed later this year. The Rocky Flats shells, a set of highly enriched uranium metal hemishells, will be stacked in two sets and placed on the Planet vertical lift machine in one symmetrical and two asymmetrical configurations. The vertical lift machine will allow the two stacked halves to be situated at various separation distances so that both weak and strong coupling can be observed.

1.1   Reactor Physics

When the field of reactor physics emerged in the twentieth century, researchers borrowed from gas dynamics to develop a detailed mathematical description of the behavior of neutrons in a system. The neutron transport equation, also referred to as the Boltzmann equation, describes

the change in the neutron population in a system over time by comparing neutron production and loss rates. The equation contains seven independent variables (three in position, two in direction, one in energy and one in time) which makes it very difficult to solve. Since its development, many approximations and simplifications have been made to facilitate solving the problem of neutron transport. At the extreme end of simplification lie the point kinetics equations, which do away with the spatial, spectral, and angular components of the transport equation through variable separation and integration to focus on the rate of change of the magnitude of the neutron population.

1.1.1 Criticality

A reactor system is characterized by its state of criticality, which describes the average time-dependent behavior of the neutron population. If a system is critical, then the neutron population is exactly balanced between production and loss without the aid of an external source; i.e., the number of neutrons in the system will not change on a macroscopic level with time (steady-state). A supercritical system has an exponentially increasing neutron population and is therefore an undesirable state in most cases as it indicates a runaway reaction. A subcritical system, on the other hand, has a neutron population that decays away exponentially and thus a chain reaction cannot be sustained. Subcritical systems are desirable in many applications, including accelerator-driven subcritical systems (ADS) for transmutation of nuclear waste and some research reactors. For such systems, an external source is necessary to keep the system at a steady state.

Two types of "criticality" exist mathematically: prompt criticality and delayed criticality. At prompt critical, the system is critical on prompt neutrons alone (i.e., neutrons released within 10^{-14} seconds after fission). A system at prompt critical is inherently unstable and extremely difficult to control on realistic time scales due to the very short time between each successive generation (on the order of 10^{-5} seconds). A neutron "generation" is the average time from the birth of a neutron in a fission event to its death either via leakage from the system or by absorption within the system, including any interactions and thermalization (slowing-down) that may take place. Delayed criticality occurs when the system time response is governed by both prompt and delayed

neutrons; i.e., the small fraction of neutrons released from fission product decay at some time later (seconds to minutes) after a fission event. The much longer mean generation lifetimes (about 0.1 seconds on average) of the tiny fraction of neutrons which are delayed aids in slowing down the time response of the system.

Criticality is most often represented by a balance term called the effective multiplication factor, k_{eff}, which represents the ratio of neutron production to neutron loss. At delayed critical, k_{eff} is unity; for a subcritical system, $k_{eff} < 1.0$ and $k_{eff} > 1.0$ for a supercritical system. Prompt criticality is often represented by k_p, or the prompt multiplication factor. The prompt multiplication factor and the effective multiplication factor are related by $k_p = k_{eff}(1 - \beta)$, where β is the delayed neutron fraction.

1.1.2 Time-Dependent Reactor Analysis

The time-dependent analysis of reactor systems can be divided into two fields characterized by the length of time involved: dynamics and kinetics. Nuclear reactor dynamics focuses on behavior that occurs during normal long-term operations of a power reactor, such as poison buildup and fuel burnup, and is not always applicable to small, bare, metal research reactors such as those studied in this research. Reactor kinetics focuses on the short-term changes in the system, such as reactivity perturbations and transients. This research focuses on reactor kinetics; it is assumed that feedback effects, if they exist, are negligible for the systems analyzed here.

Transients and other short-term temporal behavior that do not exhibit much spatial or spectral dependence can be described by a set of equations known as the point kinetics equations. The basis of the formulation of point kinetics lies in the separation of the neutron flux or neutron population term into a space- and energy-dependent, time-insensitive shape function and a time-dependent but space- and energy-independent amplitude function. This allows the shape function to disappear from the left-hand-side of the equation and therefore only the time rate of change of the magnitude of the neutron population is sought. One common form of the single-point kinetics equations is

shown in Equation 1.1:

$$\frac{dn(t)}{dt} = \frac{\rho - \beta}{\Lambda} n(t) + \sum_i \lambda_i C_i(t) + q(t)$$

$$\frac{dC_i(t)}{dt} = \frac{\beta_i}{\Lambda} n(t) - \lambda_i C_i(t), i = 1, ..., m$$

(1.1)

where n is the neutron population, C_i is the delayed neutron precursor concentration, ρ is the system reactivity, β_i is the effective delayed neutron fraction for the ith group, $\beta = \sum \beta_i$ is the total effective delayed neutron fraction, Λ is the mean prompt neutron generation time, λ_i is the lifetime of the delayed neutron group i, and q is the external neutron source strength. The coefficient of the first term on the right-hand-side of the first equation represents the time rate of change of the average individual prompt neutron chain. This "prompt neutron decay constant," represented by the variable $\alpha = \frac{\rho - \beta}{\Lambda}$ and having units of inverse unit time (s^{-1}), is positive for a supercritical system, negative for subcritical and delayed critical systems, and exactly zero when a system is prompt critical.

Single-point kinetics is applicable to most tightly-coupled systems, that is, systems where one region responds rapidly to a change in reactivity in another region. "Coupling" refers to the ability of neutrons to travel from one region to another and cause a change in the response. The assumptions in single-point kinetics start to break down as coupling weakens and the system becomes loosely coupled. When a system is loosely coupled, perturbations in one region take a longer time to spread to other regions, resulting in nearly independent behavior within each region. For example, a control rod insertion or extraction in one region will quickly change the flux level in the vicinity of the control rod, but it may take a much longer amount of time for that change to propagate to another region. This is a phenomenon referred to as "flux tilting" in large power reactors. In physically separated systems, the time delay in the response may be even more pronounced. In particular, the assumption of the separation of the neutron flux term in space and time, an important part of point kinetics, is no longer valid on a system-wide scale. Examples of coupled systems include large power reactors, clustered modular reactors, accelerator-driven subcritical systems,

and fissile material storage arrays. Such systems require a more detailed method of analysis than what single-point kinetics can provide.

Several techniques are available to analyze spatial dependence without resorting to the solution of the full transport or diffusion equation, including modal expansion [7, 8, 9], nodal analysis [10, 11], and finite-difference approximations [8]. Modal analysis involves expansion of the neutron flux term into a sum of several space-dependent modes, each multiplied by a time-dependent expansion coefficient. Modal methods are inherently complex and the results are not easily interpreted as physical parameters. Nodal methods, on the other hand, treat the spatial dependence of the system by physically dividing it up into regions or "nodes." If a system is divided by a fine mesh, then finite-difference methods apply. Finite-difference methods are very thorough at the expense of being computationally intensive. This research will consider a coarse, region-based nodal method, which will be referred to here as the "multipoint" kinetics method (or as "coupled-core" kinetics for systems with two regions). Multipoint kinetics provides a coupled set of ordinary differential equations which are easily calculated with a simple computer program. This method was chosen primarily because it lends itself best to physical interpretation of the parameters. It is ideal for comparison to Rossi-alpha measurements since the coupled Rossi-alpha values can easily be derived from the multipoint kinetics equations.

The multipoint kinetics equations account for spatial dependencies on a macroscopic scale by analyzing the system parameters region-by-region and determining the magnitude of influence that neutrons leaked from one region have on the behavior of another region. This neutronic influence between regions is represented by a term called the coupling coefficient. Formally stated, the coupling coefficient represents the probability that a neutron born in one region will leak from that region, traverse a given distance, enter the region of interest and subsequently cause a fission event. A formal derivation of the multipoint kinetics equations is provided in Chapter 2.

1.2 A History of Multipoint Kinetics

In 1958, the concept of multipoint reactor kinetics was born from the mind of R. Avery to over-come shortcomings in the single-point kinetics model in describing the behavior of fast-thermal breeder reactors [10]. Avery's formulation divided the standard point kinetics model into a series of region-based equations describing the transfer of neutrons within each region and between regions. Coupling coefficients, k_{jk}, are defined as the probability that a neutron born in Region k will leak from that region, enter Region j, and subsequently cause a fission event in that region (when $k = j$, the neutron causes a fission in the region that it was born in). These values can be found by taking the ratio of the partial source to the total source in each region as shown in Equation 1.2:

$$k_{jk} = \frac{S_{jk}}{S_k} \tag{1.2}$$

where S_k is the neutron source in Region k and S_{jk} is the source of neutrons leaving Region k and entering Region j:

$$S_j = \sum_{k=1}^{N} S_{jk} \tag{1.3}$$

By setting $S_{jk} \equiv \frac{N_{jk}}{l_{jk}}$, where N_{jk} is the density of neutrons born in Region k that enter Region j and cause fissions and l_{jk} is the partial neutron lifetime for those neutrons, Avery's coupled reactor kinetics equations take on the appearance of the point kinetics equations:

$$\frac{dN_{jk}}{dt} = k_{jk} \left(1 - \beta \right) \sum_{m=1}^{N} \frac{N_{km}}{l_{km}} - \frac{N_{jk}}{l_{jk}} + k_{jk} \sum_{i=1}^{D} \lambda_i C_{ki}$$

$$\frac{dC_{ki}}{dt} = \beta_i \sum_{m=1}^{N} \frac{N_{km}}{l_{km}} - \lambda_i C_{ki} \tag{1.4}$$

Cockrell and Perez generalized Avery's formulation to account for any number of regions and expanded it to include spectral coupling [12]. For a system consisting of m regions and n energy

groups, this results in a set of $(m \times n)^2$ equations when excluding delayed neutron contributions. Cockrell also introduced new neutron lifetime terms to describe the differences between neutron lifetime in a region ($l_{jk}^{\alpha\beta}$), the lifetime of a neutron traveling between regions ($\sigma_{jm \to k}^{\alpha\beta}$), and the removal of $j - \alpha$ neutrons from energy group β in Region k ($\theta_{jk}^{\alpha\beta}$).

Avery's heuristic formulation is difficult to extract in rigorous derivation and the parameters are not intuitively linked to physical parameters. Adler et al. stated that "...a mathematically clear cut interpretation of the Cockrell and Avery parameters appears to be not always possible" [13]. Komata [14], Kobayashi [15], and most recently Wang et al. [16] took on the challenge of rigorously deriving Avery's coupled core equations from the diffusion equation. Komata assigned a partial flux and a partial adjoint flux to each region. Both Komata [17] and Pluta [18] also extended the formulation to account for a time-dependent coupling coefficient.

Pluta used Avery's equations to calculate the relative power changes that would be observed by modifying the coupling between the regions for a theoretical critical two-region system (without accounting for feedback) [18]. For a symmetrical system (i.e., where the reactivity in one region is equivalent to the reactivity in the other region), the relative power response of the passive region becomes more equivalent to that of the driver region as coupling increases. The responses become exactly equivalent at "perfect" coupling ($k_{11} = k_{22} = k_{12} = k_{21} = 0.50$); however, Pluta observed that the responses were essentially equivalent at reactivities above $k_{jk} = 0.05$. For asymmetrical systems (i.e., the reactivity in one region is higher than the reactivity in the other region), two scenarios were assumed: first, a system where the region with the higher reactivity acts as the driver region, and second, a system where the region with the lower reactivity is set as the driver region. For the first scenario, the system behaves according to the single-point model when the reactivity of the driver region is high and that of the passive region is almost zero. As the reactivity of the passive core increases, the coupling decreases. When the driver region is the region with the lower reactivity, the passive core responds more weakly to changes in the power level in the driver region. This work effectively demonstrated some of the limits of coupled-core systems; the current research will expand on such analysis.

Avery stated that there is no single definitive formulation for coupled reactor kinetics [10]. A year after Avery's publication, G. C. Baldwin developed an alternative method that considers the coupled neutrons as a separate neutron source for loosely-coupled systems [11]. The effect of the coupled neutrons, according to Baldwin, could be realized using a coupling term that describes the probability of a neutron born in one region reaching the other region and a transit time term that allows for a finite transit time between regions. Avery's equations did not necessitate the use of a transit time since the regions in the breeder reactor under consideration were adjacent. Fissile regions in loosely-coupled systems, alternatively, usually exhibit some degree of physical separation. This separation can greatly influence the coupling terms and therefore cannot be ignored in many cases. Baldwin's equations, derived from the regional diffusion equations and generalized to account for m cores by Seale [19, 13], are:

$$\frac{dN_j(t)}{dt} = \frac{k_j^{ex}}{l_j} N_j(t) - \sum_{i=1}^{6} \frac{dC_{ij}(t)}{dt} + \sum_{k=1}^{m} \frac{\epsilon_{jk}}{l_j} N_k(t - \tau_{jk})$$

$$\frac{dC_{ij}(t)}{dt} = -\lambda_i C_{ij}(t) + \frac{k_j \beta_k}{l_j} N_j(t)$$

(1.5)

where $k_j^{ex} = k_j - 1$, k_j is the k_{eff} of the isolated region, τ_{jk} is the average transit time for neutrons traveling from Region k to Region j, and ϵ_{jk} is the coupling reactivity.

G. E. Hansen developed yet another approach by separating the flux (neutron population) into that contributed by neutrons born in the region of interest (N_j) and remaining there until a specified time t, and all other neutrons residing in the region (N_j') [20, 21, 22, 13]. The coupling neutrons are described by a surface source via a leakage term. The kinetic equations derived using Hansen's

method, ignoring delayed neutrons, are:

$$\frac{dN_j(t)}{dt} = -\frac{1-k_j}{k_j}\frac{N_j(t)}{l_j} + \beta_j \int_0^t \frac{N_j}{l_j}(t-\tau)\,p(\tau)\,d\tau + \frac{N_j'}{l_j'}$$

$$+ \beta_j' \int_0^t \frac{N_j'}{l_j'}(t-\tau)\,p(\tau)\,d\tau + S_j \tag{1.6}$$

$$\frac{dN_j'(t)}{dt} = -\frac{1}{k_j}\frac{N'}{l_j'}(t) + S_j'$$

By utilizing an "either-or" approach to the neutron population, Hansen reduced the number of equations for n regions to $2n$. If it is assumed that each region is nearly critical by itself such that $\frac{N_j}{\Lambda_j} + \frac{N_j'}{\Lambda_j'} \approx \frac{N_j}{\Lambda_j}$, then Hansen's kinetics equations collapse to a form similar to the generalized Baldwin equations.

C. G. Chezem et al. derived an analytical solution to Hansen's model with transit time considerations [22]. The results clearly show that if the transit time is not ignored, then theoretically four decay modes should be present: two due to the coupling itself and two due to the transit time. However, Chezem and Helmick showed that the transit-time decay constants are too fast to be observed experimentally due to their small magnitude [23].

A few researchers applied multipoint kinetics to reflected systems [24, 25, 26]. In these papers, the multipoint kinetics equations treat the non-fissile region of the reflector. Rather than include the reflected neutrons as a second set of "delayed" neutrons [27], C. E. Cohn instead added a coupling term for neutrons returning from the reflector to the core. The core-reflector kinetics equations are:

$$\frac{dN_c}{dt} = \frac{N_c(k_c(1-\beta)-1)}{l_c} + \frac{N_r k_{rc}}{l_r} + \sum_i \lambda_i C_i + S_c$$

$$\frac{dN_r}{dt} = -\frac{N_r}{l_r} + \frac{N_c k_{cr}}{l_c} + S_r \tag{1.7}$$

$$\frac{dC_i}{dt} = \frac{N_c k_c \beta_i}{l_c} - \lambda_i C_i$$

where subscripts c and r designate the core and the reflector regions, respectively, and k_{rc} and

k_{cr} are the probability that a neutron leaving the core will be replaced by a neutron appearing in the reflector and vice versa. Cohn's model is of particular interest because it can be expanded to account for multiple fissile regions and was done so by Farinelli and Pacilio [28] and by DiFilippo and Waldman [29]. Instead of representing the neutron balance within the reflector, the second equation becomes the analog of the first equation. The equations look very similar to Baldwin's model excluding the consideration of the transit time between regions.

Upon solving for the roots of the characteristic function of the transformed kinetics equations, Farinelli and Pacilio made a few observations. Assuming that the prompt neutron decay constant of the isolated Region 2, α_2, is greater than or equal to that of Region 1, α_1,

$$|\alpha_F| \leq \alpha_1$$
$$|\alpha_S| \geq \alpha_2$$
$$|\alpha_F + \alpha_S| = \alpha_1 + \alpha_2 \tag{1.8}$$
$$|\alpha_S| - |\alpha_F| = 2\left[\frac{(\alpha_1 - \alpha_2)^2}{4} + \gamma_{12}\gamma_{21}\right]^{1/2}$$

where α_F and α_S are the measured prompt neutron decay constants of the coupled system ("F" represents the "faster" decay constant while "S" signifies the "slower" one) and γ_{jk} are the coupling time constants. These terms will be further defined in the next chapter.

1.3 Historical Coupled-Core Measurements

Historical coupled-core measurements often involved neutron noise measurements of zero-power reactor systems. Such measurements can be made in either the time or the frequency domain. Some of the more applicable measurements and relevant results are discussed here.

1.3.1 Rossi-Alpha Measurements

Several authors have developed Rossi-alpha equations for coupled-core reactors. N. Murata et al. used Pal-Bell equations and accounted for a constant transit time to derive a Rossi-alpha equation for a symmetrical two-region system [30]. If transit time is ignored, their equation reduces to that of Edelmann et al. [31]. Munoz-Cobo et al. formulated a multiregion Rossi-alpha equation for accelerator-driven subcritical systems that can account for different source types [32]. G. Kistner applied Cohn's model to the formulation of a Rossi-alpha equation for a reflected core [33]. All of the formulations reveal the sum-of-two-exponentials time behavior for two-region systems; however, none of them account for two asymmetrical regions with neutron multiplication in each region.

The Rossi-alpha method was compared to the variance/covariance method by Edelmann et al. in their study of the Argonaut Reactor Karlsruhe [31]. They performed both auto- and cross-correlation measurements and determined that the faster prompt neutron decay constant was not measurable in cross-correlation measurements. Their explanation for this was that the transit time was on the order of the channel width of the time analyzer and therefore the signal from the faster decay constant, which decays rapidly, was distorted. The results from the variance/covariance measurements do not exhibit this behavior since the response from the faster decay constant is contained within the asymptotic part of the system response. Therefore, they argued, the variance/covariance method is superior to the Rossi-alpha method for measuring the decay constants for a loosely-coupled two-region system.

Rossi-alpha and pulsed neutron measurements were performed on a pair of symmetrical, bare, highly enriched uranium (HEU) metal cylinders separated by air by J. Mihalczo [34, 1]. The experiments, shown in Figure 1.1, consisted of pairs of symmetrical cylinders of varying thicknesses, each with a diameter of 27.94 cm. The first set of experiments were performed at delayed critical and the separation distances were varied to reach that state for each set of cylinders. In the second set of experiments, the cylinders were separated by a fixed distance of 36.94 cm. A Polonium-
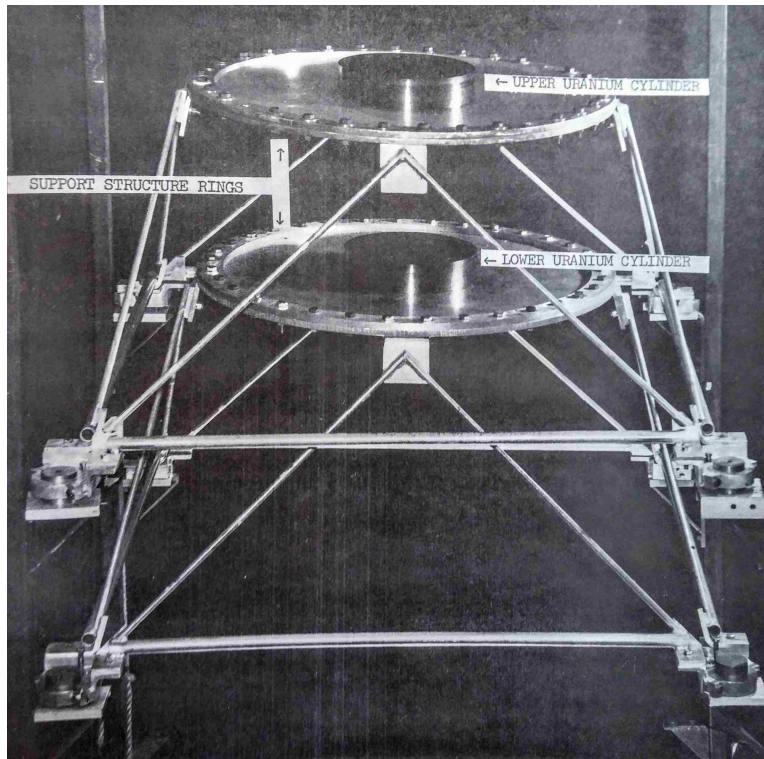
Figure 1.1: Mihalczo's coupled HEU cylinders experiment [1].

Beryllium (Po-Be) neutron source emitting approximately 10^7 neutrons per second was placed on top of the upper cylinder. Two plastic scintillation detectors were located 1.9 cm from the radial edge of the upper cylinder such that no source neutrons could reach the detectors without first entering the uranium. Mihalczo did not record the decay constants or coupling time constants for the delayed critical measurements; only the measured prompt neutron decay constant for each isolated cylinder was reported. The author assumed that only a single exponential exists for the delayed critical cases. He did state, however, that the coupling reactivities, ϵ, for the critical systems are equivalent to the magnitude at which the individual cylinder is subcritical, i.e., $\epsilon = |\rho_{iso}|$. The results for the subcritical measurements are shown in Table 1.1. The 8.255 cm case is the delayed critical configuration for the 36.94 cm separation distance. For the thinner plates (and hence lower subcritical levels), the faster prompt neutron decay constant was harder to observe. The reason for this will be addressed later in this research.

Mihalczo utilized two different methods for the Rossi-alpha analysis of the subcritical config-

Thickness	α_S (μsec^{-1})	α_F (μsec^{-1})	α_{iso} (μsec^{-1})	γ (μsec^{-1})
8.255 cm	—	—	-5.05	3.950
7.314 cm	-9.90	-20.40	-16.70	4.117
6.676 cm	-15.29	-33.90	-25.26	4.188
6.042 cm	-17.58	-36.31	-34.55	4.278

Table 1.1: Prompt neutron decay constants and coupling time constants from measurements of bare symmetrical HEU cylinders by J. Mihalczo [1].

urations. In the first method, a detector was placed on each cylinder. For the second method, both detectors were placed on one region. At a separation distance of 36.94 cm, the cylinders were very loosely coupled as shown by the small values for the coupling coefficients.

1.3.2 Other Historical Coupled-Core Neutron Noise Measurements

In a report on the coupled-reactor experiment involving two Kiwi research reactors, Chezem et al. measured the coupling at various separation distances and revealed the exponential relationship between separation distance and the coupling coefficient [22]. It should be noted, as with any of these experiments, that the coupling coefficients cannot be measured directly but are inferred via relationships with measurable parameters such as the change in reactivity or the prompt neutron decay constants.

J. R. Harries [35] performed flux tilt and correlated neutron measurements on the symmetrical AAEC Split-table Critical Facility. The author defined the two exponentials in the correlation functions differently than in other papers: according to Harries, one of the decay constants represents the decay of the isolated region without coupling, $\alpha = \frac{\beta}{\Lambda}$, and the other decay constant is a function of the coupling, $\alpha = \frac{\beta + 2\epsilon}{\Lambda}$. It was concluded that a single average value for the transit time was adequate; however, the thermal neutron wave velocity should not be chosen as it is much longer than the actual transit times measured from cross-spectra.

McDonnell and Harris studied the Universities Research Reactor, a symmetrical graphite-reflected two-slab system using the pulsed source method and compared the results to the predictions determined from models developed by Belleni-Morante, Baldwin, Chezem and Helmick,

and McDonnell and Harris [36]. The models are based off of Baldwin's original theory, but differ in the treatment of the transit time distribution. They determined that the coupling reactivities calculated from the measured prompt neutron decay constants using each model did not vary much and therefore concluded that the simplest model, that of Belleni-Morante [37], would be adequate for analysis. The authors first measured the system with a symmetrically-placed source and observed that the coupling behavior was suppressed [38]. They then moved the source to the other side of one of the slabs such that there was no direct line-of-sight between the source and the second slab. In the latter configuration, they were able to observe the two decay constants predicted by their models. They also modified the core loading and noted that at near-critical, the coupling reactivity was essentially constant [36].

Pulsed-source experiments based on Cohn's formulation were carried out by A. Waltar and L. Ruby on a reflected core [39], by Farinelli and Pacilio for a dual-core system separated by graphite [28], and by Difilippo and Waldman for a dual-core swimming pool reactor [29]. Waltar and Ruby observed the global reactivity of the system as a function of detector position and of source position. They determined that the signal becomes distorted at the core-reflector interface. The reactivity remains constant elsewhere regardless of detector position and changes only slightly between the core and reflector regions when the source is moved out of the core and into the reflector. The reason for the inability to accurately measure the decay constants, and hence the reactivity, at the interface is because of the "significantly lower intensity" of the faster decay constant and also perhaps because of a "mixing of the modes" that would prevent the individual modes from being extracted from the data, they stated. The authors also addressed the issue that the bimodal decay constants could be interpreted as "harmonic contamination:" they stated that if this were the case, then they should have observed a faster decay constant that is sensitive to the location of the source, which they did not see. The authors also noted the values of both decay constants as the system approached prompt critical, reporting that the value for the faster decay constant remained relatively flat while the slower decay constant decreased quickly as the critical level increased and it "appears to extrapolate to zero for the prompt critical condition as it should." In closing, Waltar

15

and Ruby mentioned that they believe Cohn's model would fail for "highly asymmetric systems, systems too small for diffusion theory to be valid, or in reactors constructed of such material that the spatial difference between the prompt and delayed neutron modes is appreciable."

Farinelli and Pacilio tested detector placement and observed only a single decay constant when the detector was placed at the plane of symmetry between the two cores, which they believed to be a combination of the neutron populations from both regions with "approximately identical coefficients" [28]. They cautioned against measuring a coupled system in this way, which "may lead to erroneous conclusions of equivalence between a coupled and a single system." The decay constants measured at the other two detector locations (placed on opposite sides of each core such that the detector could only see neutrons directly from one core) were identical as predicted by theory. The authors recorded the dual decay constants and the coupling multiplication, k_{jk}, of the system for several symmetrical configurations. They considered "loose coupling" to be coupling multiplications at or below 0.03.

Difilippo and Waldman similarly approached their measurements of a two-core system separated by water [29]. They theorized on the limits of coupled-core kinetics, i.e., when coupling is strong and when it is zero. When a system is strongly coupled, they said, the faster decay constant is quite large and therefore dies away quickly while the slower decay constant approaches that of a single point reactor. On the other hand, when there is no coupling, both of the decay constants approach that of the single decay constant for each core in isolation. The authors also deduced that the reactivity of a very weakly coupled core system could be determined from measuring the reactivities and the decay constants of the isolated cores. These limits will be explored for asymmetrical systems in this paper.

Other pulsed source measurements utilizing a surface coupling theory were done by Tai and Schneeberger to obtain the transit time between the asymmetrical regions of the CROCUS reactor [40]. The authors measured the prompt neutron decay constants and transit times for different reactivities and source widths. Their results for the transit times contained large errors, but they were able to show that the average transit time for neutrons traveling from Region 1 to Region

2 was not the same as those traveling from Region 2 to Region 1, as should be expected for an asymmetrical system. They, however, did not determine the coupling constants for the system.

Hashimoto et al. more recently applied the rod drop technique to the dual-slab, graphite-reflected and light-water moderated UTR-KINKI reactor to obtain the coupling coefficients [41]. In a rod-drop experiment, negative reactivity is added to the system by dropping a control rod into the core (if the control rod is a neutron absorber) or out of the core (if the control rod is a nuclear fuel). They showed that a two-point kinetic model was needed to analyze the UTR-KINKI reactor because the one-point model was dependent on detector position. The authors argued that the rod-drop method is preferable to the pulsed-source and other measurement techniques because an external neutron source (either pulsed or constant) is not needed and the data processing is much simpler. The paper reported coupling coefficients for both a symmetric and an asymmetric case; however, only a single coupling coefficient was reported for the asymmetric case, revealing an assumption that the coupling is symmetrical even if the system is not.

One of the only other analyses of an asymmetrical system found was performed on the FMRB, a swimming-pool-type reactor, by E. Viehl [42]. Viehl used Baldwin's method in the analytical analysis, deriving the auto- and cross-spectral densities in a general form to account for the system asymmetry. The asymmetry was only in the power ratios between the regions (and within the prompt neutron generation times) and not in the geometry of the system. Viehl used a calculated "symmetrical" ($\epsilon_{12} = \epsilon_{21} = \epsilon$) coupling reactivity in the analysis.

1.4   Summary

In summary, several approaches to the multi-region problem have been developed; however, not every approach lends itself to a simple computational method of solution nor do the parameters necessarily describe physical, observable attributes of the system. The "effective source" method developed by Baldwin is very similar in form to the standard point kinetics equations with the addition of a separate source term describing the coupling between regions. It best defines coefficients

that represent measurable parameters. A slightly modified version of Baldwin's kinetics equations are derived in this paper. From these results, the Rossi-alpha equation for a system composed of two asymmetrically-coupled fissile regions is derived. This equation is similar to that of Kistner's reflected-reactor Rossi-alpha equation [33].

The results from the previously described subcritical measurements performed by J. Mihalczo are used here to verify the computational methods developed to simulate a Rossi-alpha measurement. The Rossi-alpha method, along with the new predictive capability, will then be used to observe the coupling in similarly bare and subcritical, but asymmetrical, systems. Asymmetry in mass and in geometry will be observed. Even though a few measurements were performed on asymmetrical reactor systems, the researchers assumed symmetry in the coupling reactivities or constants. Part of the difficulty in determining the asymmetrical coupling terms is the fact that only the product of the two coupling time constants can be determined from measurements. In this research, not only will the coupling be observed, but a method is developed to separate the asymmetrical coupling terms.

This research will also provide a thorough analysis of the effect of separation distance on the behavior of loosely-coupled reactor cores for both symmetrical and asymmetrical configurations. The effects of detector placement will also be studied.

Chapter 2

Multipoint Kinetics Theory

This research focuses on the multipoint kinetics method, which has been shown to describe the kinetic behavior of many systems with spatial effects more accurately than the standard point kinetics method while employing only a marginal increase in computational time. The flexibility in selectively choosing macroscopic regions versus creating a uniform mesh allows for the simplification of the computation over that of the finite element method and for a naturally physical interpretation of the results. The approach taken here is that originally developed by Baldwin [11] and generalized by Seale [19].

2.1   General Formulation of the Multipoint Kinetics Equations

The multipoint kinetics equations are generally derived from either the neutron transport equation or the diffusion equation, which describe the time-dependent behavior of the neutron population within the system. To obtain the multipoint kinetic equations in their most general form, the transport equation will serve as the starting point. The following derivation utilizes subscripts to denote regions, cross-section types and delayed neutron groups and superscripts for any other identifiers such as energy. Furthermore, subscript j shall refer to the region of interest while subscript k will denote the other region(s) whose neutronic contributions affect the response of the region of interest.

The formulation of the regional neutron transport equation follows that of the general transport

equation with the exception of an additional term representing a "source" of neutrons leaking from the other region(s) and entering the region of interest. For Region j, the time rate of change of the neutron population at point $\vec{r}$, energy E, angle Ω and time t is:

$$\frac{1}{v\left(E\right)}\frac{d\varphi_j\left(\vec{r},E,\Omega,t\right)}{dt} = -\Omega\cdot\nabla\varphi_j\left(\vec{r},E,\Omega,t\right) - \Sigma_t\left(\vec{r},E,t\right)\varphi_j\left(\vec{r},E,\Omega,t\right)$$
$$+ \int dE'\int d\Omega'\Sigma_s\left(\vec{r},E',\Omega'\to E,\Omega,t\right)\varphi_j\left(\vec{r},E',\Omega',t\right)$$
$$+ \frac{\chi_p\left(E\right)}{4\pi}\int dE'\int d\Omega'\nu_p\left(E'\right)\Sigma_f\left(\vec{r},E',t\right)\varphi_j\left(\vec{r},E',\Omega',t\right) \quad (2.1)$$
$$+ \sum_i\frac{\chi_{d,i}\left(E\right)}{4\pi}\lambda_i C_{i,j}\left(\vec{r},t\right) + S_{jk}\left(\vec{r},E,\Omega,t\right) + S_j\left(\vec{r},E,\Omega,t\right)$$

and the delayed neutron precursor rate equation is given as:

$$\frac{dC_{i,j}\left(\vec{r},t\right)}{dt} = \nu_{d,i}\Sigma_f\left(\vec{r}\right)\varphi_j\left(\vec{r},t\right) - \lambda_i C_{i,j}\left(\vec{r},t\right) \quad (2.2)$$

where

$$\varphi_j = \qquad \text{neutron angular flux in Region } j$$

$$v = \qquad \text{neutron velocity}$$

$$\Sigma_t = \qquad \text{macroscopic total cross-section}$$

$$\Sigma_s = \qquad \text{macroscopic scatter cross-section}$$

$$\Sigma_f = \qquad \text{macroscopic fission cross-section}$$

$$\chi_p = \qquad \text{prompt neutron fission spectrum}$$

$$\chi_{d,i} = \qquad \text{delayed neutron fission spectrum for delayed group } i$$

$$\lambda_i = \quad \text{delayed neutron precursor decay constant for delayed group } i$$

$$C_{i,j} = \quad \text{delayed neutron precursor density in Region } j \text{ for delayed group } i$$

$$S_{jk} = \quad \text{neutron source contributed by Region } k \text{ to Region } j$$

$$S_j = \quad \text{external source applied to Region } j$$

$$\nu_p = \quad (1 - \beta)\,\nu$$

$$\nu_{d,i} = \quad \beta_i \nu$$

$$\nu = \quad \text{average number of neutrons produced per fission}$$

$$\beta_i = \quad \text{delayed neutron fraction of the } i^{\text{th}} \text{ precursor group}$$

$$\beta = \quad \sum_i \beta_i$$

The subscript i represents the ith delayed neutron group and p and d denote prompt and delayed neutrons, respectively. It is implied that the cross-sections and energy spectra are those of Region j; the subscripts have been omitted.

The source term S_{jk} represents the neutronic contribution to Region j from all of the other regions in the system. It can be equated to

$$S_{jk}\,(r, E, \Omega, t) = \sum_{\substack{k=1 \\ k \neq j}}^{m} \varepsilon_{jk}\,(r, E, \Omega, t) \int_0^\infty \phi_k\,(t - \tau_{jk})\,p\,(\tau_{jk})\,d\tau \qquad (2.3)$$

The coupling coefficient, ε_{jk}, is defined as the probability that a neutron born in Region k will leak from that region, enter Region j and cause a fission and has units of cm^{-1}. The term $\phi_k\,(t - \tau_{jk})$ is the neutron flux integrated over the phase space of Region k at some previous time $t - \tau_{jk}$, where τ_{jk} is the neutron transit time between Regions k and j. The final term, $p\,(\tau_{jk})$, is a time distribution kernel for τ_{jk}. If the transit time is negligible compared to the neutron lifetimes within the regions, then it can simply be ignored and the coupling term reduces to $\epsilon_{jk} n_k\,(t)$.

The appearance of the regional transport equation can be simplified via conversion to operator

notation. It can be rewritten as

$$\frac{1}{v}\frac{d\phi_j}{dt} = (F_{p,j} - M_j)\varphi_j\,(r, E, \Omega, t) + S_{d,j}\,(r, E, \Omega, t) + S_{jk}\,(r, E, \Omega, t)$$
$$+ S_j\,(r, E, \Omega, t) \tag{2.4}$$

where

$$F_{p,j} = \frac{\chi_p\,(E)}{4\pi}\int dE'\int d\Omega'\nu_p\,(E')\,\Sigma_f\,(r, E', t) \tag{2.5}$$

$$M_j = \Omega\cdot\nabla + \Sigma_t\,(r, E, t) - \int dE'\int d\Omega'\Sigma_s\,(r, E', \Omega' \to E, \Omega, t) \tag{2.6}$$

$$S_{d,j} = \sum_i \frac{\chi_{d,i}\,(E)}{4\pi}\lambda_i C_{j,i}\,(r, t) \tag{2.7}$$

It is conventional to rewrite the prompt fission operator in terms of the total and delayed fission operators as such [43]:

$$F_{p,j} = F_j - F_{d,j} \tag{2.8}$$

where

$$F_{d,j} = \sum_i \frac{\chi_{d,i}\,(E)}{4\pi}\int dE'\int d\Omega'\nu_{d,i}\Sigma_f\,(r, E', t) \tag{2.9}$$

$F_{d,j}\varphi$ describes the delayed neutrons that would be produced at some steady-state instance in time t. This term is not the same as the delayed neutron source $S_{d,j}$.

Point kinetics relies on the ability to separate the neutron flux term in time and space. In multipoint analysis, this assumption is only valid for loosely-coupled systems in which each region operates nearly independently. According to Baldwin, "the observation that a single stable period exists, the relative smallness of the interaction term, and the fact that $[\varphi_j]$ does not vary widely throughout the... cores justify the assumption of separability" [11]. Thus if it can be assumed that the shape of the flux in each region varies very little over time, the flux function can be separated into a phase-space dependent shape function, ψ_j, and a purely time-dependent amplitude function, n_j:

$$\varphi_j\,(r, E, \Omega, t) \simeq n_j\,(t)\,\psi_j\,(r, E, \Omega) \tag{2.10}$$

Similarly, the coupled flux term can be separated:

$$\phi_k (t - \tau_{jk}) \simeq n_k (t - \tau_{jk}) \psi_k (t - \tau_{jk}) \tag{2.11}$$

And the delayed precursor concentration can be separated:

$$C_{j,i} (r, t) \simeq c_{j,i} (t) \psi_j (r) \tag{2.12}$$

The variable separation results in some amount of error; therefore, a weighting function is introduced. The derivation of the multi-point kinetics equations is performed in the same manner as that of the standard point kinetics equations [44, 43]; however, instead of integrating over the phase space of the entire system, the weighted transport and precursor equations are integrated over the phase space of the region of interest, as shown in Equation 2.13.

$$\begin{aligned}
\left\langle w, \frac{1}{v} \frac{d\varphi_j}{dt} \right\rangle &= \langle w, (F_j - M_j) \varphi_j \rangle - \langle w, F_{d,j} \varphi_j \rangle + \langle w, S_{d,j} \rangle \\
&\quad + \langle w, S_{jk} \rangle + \langle w, S_j \rangle
\end{aligned} \tag{2.13}$$

where w is a weighting function and $\langle . , . \rangle$ represents integration over phase space.

Replacing the flux with Equation 2.10, the left side of Equation 2.13 can be rewritten as:

$$\left\langle w, \frac{1}{v} \frac{d\varphi_j}{dt} \right\rangle = \frac{dn_j (t)}{dt} \left\langle w, \frac{\psi_j}{v} \right\rangle + n_j (t) \frac{d}{dt} \left\langle w, \frac{\psi_j}{v} \right\rangle \tag{2.14}$$

Since the shape function is assumed to vary slowly with time to the point of negligible time dependence, the second term on the right hand side of Equation 2.14 disappears.

The weighting function should be chosen such that the error in the kinetics calculations due to the choice of the shape function is minimized, primarily with respect to errors in the reactivity. The steady-state (pre-perturbation) adjoint flux is generally used as the weighting function for systems at or close to critical, which results in second order accuracy. The adjoint flux effectively details the "importance" of a neutron; in other words, it describes how much a neutron contributes to the

overall response of the system. For loosely-coupled systems, application of a regional adjoint flux rather than a systemwide adjoint flux is more appropriate because of the nearly independent flux behavior within each region described earlier.

Not all systems of interest operate at or near critical. In deeply subcritical systems (i.e., systems with a $k_{eff} < 0.95$), the importance of the source neutrons should be taken into account along with that of the neutrons generated from fissions within the region of interest. Not only does this require a new definition of the importance function, it also leads to new definitions of the kinetics parameters.

Several researchers have formulated adjoint functions for deeply subcritical single-point systems [45, 46, 47, 48]. These formulations commonly simplify to the standard (critical) definition as the system nears criticality: the influence of the external source is reduced as the system approaches a critical state. The differences in each formulation lie in the definition of the adjoint source term. While the adjoint function for a critical system is uniquely defined, it is not for a subcritical system. The choice of an adjoint formulation, then, depends on the ease of calculation, comparison to experimental results, and on whether the resulting kinetics parameters can be physically defined.

The regional adjoint equation for a time-independent reference system defined for the subcritical state is given as:

$$M_{0,j}^{\dagger}\varphi_{s,j}^{\dagger} + F_{0,j}^{\dagger}\varphi_{s,j}^{\dagger} + S_{0,j}^{\dagger} = 0 \tag{2.15}$$

where $S_{0,j}^{\dagger}$ is the adjoint source term and $\varphi_{s,j}^{\dagger}$ can be defined as the likelihood that a neutron originating from anywhere in the system will cause a fission in Region j. Following from [46], an adequate definition of the adjoint source is the fission productivity, $\nu\Sigma_{f,0}$. The weighting function, w, for the multipoint kinetics equations is thus chosen to be the adjoint function, i.e., the solution to Equation 2.15:

$$w = \varphi_{s,j}^{\dagger} \tag{2.16}$$

By algebraically rearranging the resulting equations, the multi-point kinetics equations are

found:

$$\frac{dn_j(t)}{dt} = \frac{\rho_j(t) - \beta_j}{\Lambda_j} n_j(t) + \sum_{\substack{k=1 \\ k \neq j}}^{m} \frac{\epsilon_{jk}}{\Lambda_j} \int_0^t n_k(t - \tau_{jk}) \, p(\tau_{jk}) \, d\tau_{jk}$$

$$+ \sum_{i=1}^{6} \lambda_{j,i} C_{j,i}(t) + s_j \tag{2.17}$$

$$\frac{dc_{j,i}(t)}{dt} = \frac{\beta_{j,i}}{\Lambda_j} n_j(t) - \lambda_{j,i} C_{j,i}(t), \qquad i = 1, ..., 6 \tag{2.18}$$

The kinetics equations describe the time rate of change of the prompt neutron amplitude response, $n_j(t)$, and the delayed neutron precursor amplitude response, $c_{j,i}(t)$, of the region of interest.

2.1.1 Definitions of the Kinetics Parameters

The kinetics parameters are defined as follows:

Local reactivity:

$$\rho_j = \frac{\left\langle \varphi_{s,j}^\dagger, (F_j - M_j) \psi_j \right\rangle}{\left\langle \varphi_{s,j}^\dagger, P_j \right\rangle} \tag{2.19}$$

Effective prompt neutron generation time:

$$\Lambda_j = \frac{\left\langle \varphi_{s,j}^\dagger, \frac{1}{v} \psi_j \right\rangle}{\left\langle \varphi_{s,j}^\dagger, P_j \right\rangle} \tag{2.20}$$

Effective delayed neutron fraction:

$$\beta_{eff,j} = \frac{\left\langle \varphi_{s,j}^\dagger, \sum_i F_{di,j} \psi_j \right\rangle}{\left\langle \varphi_{s,j}^\dagger, P_j \right\rangle} \tag{2.21}$$

Spatial coupling reactivity:

$$\epsilon_{jk} = \frac{\left\langle \varphi_{s,j}^\dagger, \varepsilon_{jk}\psi_k \right\rangle}{\left\langle \varphi_{s,j}^\dagger, P_j \right\rangle} \tag{2.22}$$

Effective source strength:

$$s_j = \frac{\left\langle \varphi_{s,j}^\dagger, S_j \right\rangle}{\left\langle \varphi_{s,j}^\dagger, P_j \right\rangle} \tag{2.23}$$

where

$$P_j = F_j\psi_j \tag{2.24}$$

is an arbitrary normalization function. The choice of P_j is purely dependent on the desired physical descriptions of the kinetics parameters. It can be seen in the formulation that this term cancels out when the ratios $\frac{\rho}{\Lambda}$ and $\frac{\beta}{\Lambda}$, the measurable quantities, are analyzed, and therefore it has no effect on the kinetic behavior of the system.

The kinetics parameters should describe physical aspects of the system if they are to be of any practical usefulness. The local reactivity, ρ_j, is defined as the ratio of the weighted excess neutron production to the total neutron production within the region of interest under isolation (i.e., when the other region or regions are not present). It reveals the region's time-dependent or -independent degree of departure from the critical state.

The prompt neutron generation time, Λ_j, represents the average time between the birth of a neutron from a fission event and the birth of a next-generation neutron in Region j.

The effective delayed neutron fraction, $\beta_{eff,j}$, describes the amount of influence of the delayed neutrons in Region j. It differs from the actual delayed neutron fraction: while the actual delayed neutron fraction is generally an unchanging property of the region, the effective delayed neutron fraction changes with respect to the level of subcriticality. As the region becomes more subcritical, the value of the effective delayed neutron fraction will decrease as the effectiveness of the source neutrons increases since the role of reactor control moves further over to the source neutrons. Conversely, as a reactor approaches criticality, the effective delayed neutron fraction will increase as the role of delayed neutrons in the overall behavior of the system becomes more important.

The ϵ_{jk} parameter is unique to coupled multi-region problems. Here it has been termed the "spatial coupling reactivity" and it describes the positive reactivity contribution of neutrons from the other regions in the system to Region j. The term "spatial" reflects the fact that it does not contain any spectral coupling information as defined in this research. For a coupled system at critical, ϵ_{jk} is just the reactivity by which the individual region is subcritical; i.e., $\epsilon_{jk} = |\rho_j|$.

The final parameter is the effective source strength, s_j, of the external neutron source entering Region j. This term is only present for subcritical systems. For critical systems in which the neutron production and loss are balanced without the aid of an external neutron source, this term disappears.

The coefficients of the first term on the right-hand-side of the kinetics equation can be rewritten as:

$$\frac{\rho_j - \beta_{eff,j}}{\Lambda_j} = \alpha_j \tag{2.25}$$

This parameter is the prompt neutron decay constant for Region j and it represents the time behavior of the prompt neutron population within only that region. The coupling term can also be simplified into a time constant:

$$\frac{\epsilon_{jk}}{\Lambda_j} = \gamma_{jk} \tag{2.26}$$

It will be referred to as the "coupling time constant" in this research to distinguish it from the coupling reactivity term. Both the decay constant and the coupling time constant have units of inverse time.

2.2 Solutions of the Multipoint Kinetics Equations

The multipoint kinetics equations for two regions with an external source present in Region 1 and ignoring delayed neutrons are:

$$\frac{dn_1(t)}{dt} = \alpha_1 n_1(t) + \gamma_{12} \int_0^t n_2(t - \tau) \, p_{12}(\tau) \, d\tau + s_1(t)$$

$$\frac{dn_2(t)}{dt} = \alpha_2 n_2(t) + \gamma_{21} \int_0^t n_1(t - \tau) \, p_{21}(\tau) \, d\tau \tag{2.27}$$

The solutions to Equations 2.27 can be found via Laplace transformation:

$$sN_1(s) - n_1(0) = \alpha_1 N_1(s) + \gamma_{12} \left[P_{12}(s) \, N_2(s) \right] + S_1(s)$$

$$sN_2(s) - n_2(0) = \alpha_2 N_2(s) + \gamma_{21} \left[P_{21}(s) \, N_2(s) \right] \tag{2.28}$$

It is assumed that at time $t = 0$, $n_1(0) = n_{1,0}$ and $n_2(0) = n_{2,0}$. Applying this and solving for N_1 and N_2:

$$N_1(s) = \frac{(s - \alpha_2) \, S_1(s)}{(s - \alpha_1)(s - \alpha_2) - \gamma_{12}\gamma_{21} P_{12}(s) \, P_{21}(s)}$$

$$N_2(s) = \frac{\gamma_{21} P_{21}(s) \, S_1(s)}{(s - \alpha_1)(s - \alpha_2) - \gamma_{12}\gamma_{21} P_{12}(s) \, P_{21}(s)} \tag{2.29}$$

The denominators in both equations are equivalent and represent the characteristic equation of the system:

$$(s - \alpha_1)(s - \alpha_2) - \gamma_{12}\gamma_{21} P_{12}(s) \, P_{21}(s) = 0 \tag{2.30}$$

Negligible Transit Time Assumption

If it can be assumed that the transit time between regions can be ignored, the P_{jk} terms can be omitted, allowing for a simple solution to the roots of Equation 2.30. The roots will be called α_F and α_S so as to differentiate them from the traditional prompt neutron decay constants of the

individual regions, α_1 and α_2:

$$\alpha_{S,F} = \frac{1}{2}(\alpha_1 + \alpha_2) \pm \frac{1}{2}\sqrt{(\alpha_1 - \alpha_2)^2 + 4\gamma_{12}\gamma_{21}} \qquad (2.31)$$

Equation 2.31 are the general equations for the fundamental and the first higher modes, which are the "slower" and the "faster" prompt neutron decay constants, respectively, of the multipoint kinetics equations for asymmetrical systems. If the system is symmetrical, the equations can be simplified by setting $\alpha_1 = \alpha_2 = \alpha$ and $\gamma_{12} = \gamma_{21} = \gamma$:

$$\alpha_{S,F} = \alpha \pm \gamma \qquad (2.32)$$

It can be seen from Equations 2.31 and 2.32 that the same prompt neutron decay constants will be seen regardless of which region is observed, even for an asymmetrical system, revealing that they are parameters of the system as a whole. This means that theoretically detector position should not matter and the decay constants can be determined from detectors placed on either region. The physical effect of detector location will be explored in Chapter 4.

Equation 2.31 can be rearranged to solve for the coupling coefficients as shown in Equation 2.33. It is immediately noticeable that for the asymmetrical case, the individual coupling coefficients cannot be determined from these equations alone.

$$\gamma_{12}\gamma_{21} = (\alpha_S - \alpha_1)(\alpha_S - \alpha_2) = (\alpha_F - \alpha_1)(\alpha_F - \alpha_2) \qquad (2.33)$$

However, the relationship between the coupled and the isolated prompt neutron decay constants can be seen when Equations 2.33 are equated:

$$\alpha_1 + \alpha_2 = \frac{\alpha_F^2 - \alpha_S^2}{\alpha_F - \alpha_S} \qquad (2.34)$$

A rearrangement of Equation 2.33 allows for the determination of α_F if the other prompt neu-

tron decay constants are known but the coupling coefficients are unknown:

$$\alpha_F = \frac{1}{2}\left(\alpha_1 + \alpha_2\right) - \frac{1}{2}\sqrt{\left(\alpha_1 + \alpha_2\right)^2 + 4\alpha_S\left(\alpha_S - \alpha_1 - \alpha_2\right)} \tag{2.35}$$

For a symmetrical system, this simplifies to

$$\alpha_F = 2\alpha - \alpha_S \tag{2.36}$$

Completing the solution for a symmetrical system, the equations for the amplitudes of the neutron population in Regions 1 and 2 are (ignoring the source term):

$$n_1\left(t\right) = \frac{1}{2}\left(n_{1,0} - n_{2,0}\right)e^{\alpha_S t} + \frac{1}{2}\left(n_{1,0} - n_{2,0}\right)e^{\alpha_F t}$$

$$n_2\left(t\right) = \frac{1}{2}\left(n_{1,0} - n_{2,0}\right)e^{\alpha_S t} - \frac{1}{2}\left(n_{1,0} - n_{2,0}\right)e^{\alpha_F t} \tag{2.37}$$

and for an asymmetrical system:

$$n_1\left(t\right) = \frac{\gamma_{12}}{D}\left[\left(n_{2,0} - \frac{B}{\gamma_{12}}n_{1,0}\right)e^{\alpha_S t} - \left(n_{2,0} - \frac{A}{\gamma_{12}}n_{1,0}\right)e^{\alpha_F t}\right] \tag{2.38}$$

$$n_2\left(t\right) = \frac{A}{D}\left(n_{2,0} - \frac{B}{\gamma_{12}}n_{1,0}\right)e^{\alpha_S t} - \frac{B}{D}\left(n_{2,0} - \frac{A}{\gamma_{12}}n_{1,0}\right)e^{\alpha_F t} \tag{2.39}$$

where

$$A = \alpha_S - \alpha_1$$
$$B = \alpha_F - \alpha_1 \tag{2.40}$$
$$D = \alpha_S - \alpha_F$$

The full derivation for an asymmetrical system is provided in Appendix A.

Transit Time Considerations

If the transit time cannot be ignored, then the solution to the characteristic equation is quite involved. A full transit time distribution as described in Baldwin's model allows for an infinite number of roots. This is of course unrealistic in practice and therefore various estimates of the time distribution have been made by others. If the time distribution function is chosen to be constant, $p_{jk}(t) = \delta(t - \tau_{jk})$, the Laplace transforms are $P_{jk}(s) = e^{-\tau_{jk}s}$. For this scenario, the characteristic equation is

$$(s - \alpha_1)(s - \alpha_2) - \gamma_{12}\gamma_{21}e^{-(\tau_{12}+\tau_{21})s} = 0 \tag{2.41}$$

Since the exponential term is a function of s, the solution requires some form of linear approximation. It is obvious without finding the exact roots that theoretically there should be four decay constants: two due to the spatial coupling and two as a result of the transit time.

Chezem and Helmick assumed a time distribution of the form

$$p_{jk}(t) = \frac{1}{\tau_{jk}}e^{\frac{-t}{\tau_{jk}}} \tag{2.42}$$

and, using the Laplace method to solve for the roots, determined that the equations for the prompt neutron decay constants for a two-region system are

$$
\begin{aligned}
\alpha_S &= \alpha_1 + \frac{\gamma_{12}\gamma_{21}}{(\alpha_1 - \alpha_2)\left(\alpha_1 + \dfrac{1}{\tau_{12}}\right)\left(\alpha_1 + \dfrac{1}{\tau_{21}}\right)} \\[2mm]
\alpha_F &= \alpha_1 - \frac{\gamma_{12}\gamma_{21}}{(\alpha_1 - \alpha_2)\left(\alpha_2 + \dfrac{1}{\tau_{12}}\right)\left(\alpha_2 + \dfrac{1}{\tau_{21}}\right)} \\[2mm]
\alpha_{\tau_{12}} &= -\frac{1}{\tau_{12}} + \frac{\gamma_{12}\gamma_{21}}{\left(\alpha_1 + \dfrac{1}{\tau_{12}}\right)\left(\alpha_2 + \dfrac{1}{\tau_{21}}\right)\left(\dfrac{1}{\tau_{21}} - \dfrac{1}{\tau_{12}}\right)} \\[2mm]
\alpha_{\tau_{21}} &= -\frac{1}{\tau_{21}} + \frac{\gamma_{12}\gamma_{21}}{\left(\alpha_1 + \dfrac{1}{\tau_{21}}\right)\left(\alpha_2 + \dfrac{1}{\tau_{12}}\right)\left(\dfrac{1}{\tau_{21}} - \dfrac{1}{\tau_{12}}\right)}
\end{aligned}
\tag{2.43}
$$

However, it was shown by the authors that the decay constants due to transit time are too small to be observable in experiments [23].

2.2.1 Explanation of the Dual Mode Decay Constants

The solutions in the previous section reveal the composition of the two observable prompt neutron decay constants: that they are a combination of the prompt neutron decay constants of each region in isolation and the coupling time constants. It will be shown later that for strong coupling, the faster decay mode dies off rapidly and only the slower mode persists, i.e., $\alpha_F \to \infty$ and $\alpha_S \to \alpha$. On the other hand, for very weak coupling, the decay constants approach the values of the isolated region decay constants. For a symmetrical system, this means that when the system is nearly uncoupled, $\alpha_S \simeq \alpha_F \simeq \alpha$.

Chapter 3

Rossi-Alpha Measurement Theory

3.1 Neutron Noise Measurements

Neutron noise measurements are performed to observe the fluctuations in the neutron population due to variability in individual neutron chains within a multiplying system. It is assumed that other factors that can cause noise such as temperature and mechanical and hydraulic effects are not dominant. From these measurements, kinetic parameters such as the prompt neutron decay constant, the mean neutron generation time, the delayed neutron fraction, and the reactivity can be directly obtained or inferred. Such measurements can be achieved by a number of methods in both the time and frequency domains. Frequency-domain measurements tend to focus on obtaining the transfer function of the system through spectral frequency measurements. Time domain measurement techniques are more often used for determining parameters such as the prompt neutron decay constant and include the pulsed-source [49], rod-drop [50], Rossi-alpha [51], and the Feynman-alpha methods [50]. Both the time- and frequency-domain techniques can ultimately be used to infer the coupling of a multipoint system.

The Rossi-alpha method was selected because it measures the dual-mode prompt neutron decay constants from which the coupling terms can be extracted while not requiring the complexity of a pulsed-source experiment. Secondly, the faster alpha is expected to be difficult to measure and within a time scale where a neutron pulse may be too wide to observe it at all (the typical pulse width of the Los Alamos National Laboratory's (LANL) pulsed-neutron source used in such mea-

surements is on the order of $10\,\mu s$). The primary drawback to a Rossi-alpha measurement versus a pulsed-source measurement is the length of counting time needed to obtain adequate statistics.

3.1.1 The Prompt Neutron Decay Constant

Fission reactors rely on neutron multiplication to sustain a nuclear reaction. Each neutron that enters the system, whether originating from an external source, fission event, or some other neutron-producing reaction, can start a chain reaction that propagates for some amount of time depending on the critical state of the system. The prompt neutron decay constant, α, that was derived in the previous chapter represents the rate of growth or decay of the average individual neutron chain in inverse unit time. At prompt critical, α is zero, indicating that the average length a single neutron chain is essentially infinite and the prompt neutron population does not change over time. As the system becomes more subcritical, the magnitude of α increases, indicating that the neutron chains die off more quickly. The prompt neutron decay constant below prompt critical is negative, revealing that the neutron chains die off and cannot sustain a chain reaction. Above prompt critical, α is positive, representing a chain reaction that increases exponentially. For a loosely-coupled two-region system, two observable prompt neutron decay constants exist instead of one, each representing a combination of the decay constants of the individual regions and the coupling time constants between the regions.

3.1.2 Correlation of Neutron Counts

Neutrons can be produced by decay events, (α, n) events, by spontaneous or induced fission, or by (n,xn) events. A neutron chain is created when a starting neutron causes a fission event and some of those neutrons born from that event go on to cause other fissions. This process is repeated for an average amount of time or average number of generations characterized by the prompt neutron decay constant. Each fission event produces ν_p prompt neutrons that are born at the same time. If a system provided only uncorrelated neutron counts, the Rossi-alpha response would be constant in time. The presence of neutron multiplication creates a response that is biased towards time $t = 0$

and decays exponentially according to α as t increases.

Correlated neutron measurements are generally done on zero-power systems so that individual neutron chains can be observed without much overlap from other chains; otherwise, the signal would be lost in the background counts. It is also important that the system does not have a count rate that changes with time.

3.2 Rossi-Alpha Theory

The Rossi-alpha measurement technique, described by J. Orndoff [51] and based on the theory of correlated count pairs by B. Rossi and the techniques of Feynman, de Hoffmann and Serber [52], relies on the fact that prompt neutrons originating from the same initial fission event are correlated in time. Delayed neutrons are emitted at a rate slow enough that they can be considered part of the uncorrelated or "accidental" counts along with source neutrons, background neutrons, neutrons from (α,n) events and any other neutrons not produced by fission. Prompt neutrons originating from a different neutron chain are also considered accidental pairs.

A plot of the time distribution of correlated count pairs within a time window on the order of the average chain length will give a decay curve that is nearly equivalent to the average decay of a single neutron chain. A curve fit is performed on the histogram from which the prompt neutron decay constant(s) can be extracted.

3.2.1 Derivation of the Rossi-alpha Formula for a Two-Region System

The derivation process of a Rossi-alpha equation for a two-region system is nearly identical to that of a single-region system as explained by Orndoff. First, the probability of a fission event occurring at t_0 in Region 1 is considered:

$$p_0\left(t_0\right) dt_0 = \dot{F}_0 dt_0 \tag{3.1}$$

where $\dot{F}_0$ is the average fission rate in neutrons per second. The probability of a count occurring at t_1 due to the fission at t_0 is:

$$p_1(t_1)\, dt_1 = \frac{E}{\tau_f} n_1(t_1 - t_0)\, dt_1 \tag{3.2}$$

And the probability of a correlated count occurring at t_2 given the count at t_1 is:

$$p_2(t_2)\, dt_2 = \frac{E}{\tau_f} n_1(t_2 - t_0)\, dt_2 \tag{3.3}$$

where E is the detector efficiency in counts per fission, $\tau_f = \frac{1}{v\Sigma_f}$ is the mean lifetime for fission (τ_f is related to the prompt neutron generation time by $\Lambda = 1/v\tau_f$), v is the neutron velocity and Σ_f is the macroscopic fission cross-section.

Using Equation 2.37 for n_1 and assuming that $n_0 = \nu$ at t_1 and $n_0 = \nu - 1$ at t_2 (accounting for the loss of the neutron counted at t_1), Equations 3.2 and 3.3 become

$$p_1(t_1)\, dt_1 = \frac{E\nu}{2\tau_f} \left[e^{\alpha_F(t_1 - t_0)} + e^{\alpha_S(t_1 - t_0)} \right] dt_1 \tag{3.4}$$

$$p_2(t_2)\, dt_2 = \frac{E(\nu - 1)}{2\tau_f} \left[e^{\alpha_F(t_2 - t_0)} + e^{\alpha_S(t_2 - t_0)} \right] dt_2 \tag{3.5}$$

where α_F and α_S are the faster and slower prompt neutron decay constants as defined in the previous chapter.

The probability for detecting a count at time t_1 in dt_1 and a correlated count at time t_2 in dt_2 produced from the same fission event is found from the product of the individual probabilities p_0, p_1 and p_2:

$$
\begin{aligned}
&p_0(t_0)\, p_1(t_1) p_2(t_2)\, dt_0 dt_1 dt_2 \\
&\quad = \frac{\dot{F}_0 E^2 \nu (\nu - 1)}{4\tau_f^2} \left[\left(e^{\alpha_F(t_1 - t_0)} + e^{\alpha_S(t_1 - t_0)} \right) \left(e^{\alpha_F(t_2 - t_0)} + e^{\alpha_S(t_2 - t_0)} \right) \right] dt_0 dt_1 dt_2
\end{aligned}
\tag{3.6}
$$

Since the time of the fission event is unknown, this equation is integrated with respect to t_0

from $-\infty$ to the time of the first count, t_1:

$$\left[\int_{-\infty}^{t_1} \frac{E^2 \dot{F}_0 \nu (\nu - 1)}{4\tau_f^2} \left[\left(e^{\alpha_F(t_1-t_0)} + e^{\alpha_S(t_1-t_0)}\right)\left(e^{\alpha_F(t_2-t_0)} + e^{\alpha_S(t_2-t_0)}\right)\right] dt_0\right] dt_1 dt_2 \qquad (3.7)$$

The result is averaged over the neutron fission emission distribution. It is then equated to the probability of a count at t_1, represented as $E\dot{F}_0$, and the probability of a related count at t_2:

$$E\dot{F}_0 p\,(t_2)\,dt_1 dt_2$$
$$= -\frac{E^2 \dot{F}_0 \overline{\nu(\nu-1)}}{4\tau_f^2}\left[\frac{3\alpha_F + \alpha_S}{2\alpha_F(\alpha_F + \alpha_S)}e^{\alpha_F(t_2-t_1)} + \frac{3\alpha_S + \alpha_F}{2\alpha_S(\alpha_F + \alpha_S)}e^{\alpha_S(t_2-t_1)}\right]dt_1 dt_2 \qquad (3.8)$$

Setting $t_1 = 0$ and $t_2 = t$ and solving for $p\,(t)\,dt$, the Rossi-alpha equation for a symmetrical two-region system (ignoring transit time) is:

$$p\,(t)\,dt = Cdt - \frac{E\overline{\nu(\nu-1)}}{2\tau_f^2}\left[\frac{3\alpha_F + \alpha_S}{2\alpha_F(\alpha_F + \alpha_S)}e^{\alpha_F t} + \frac{3\alpha_S + \alpha_F}{2\alpha_S(\alpha_F + \alpha_S)}e^{\alpha_S t}\right]dt \qquad (3.9)$$

where the probability for an uncorrelated count has been included via the term Cdt.

Often, the Rossi-alpha equation is presented with grouped coefficients for simplicity. Simplifying,

$$p\,(t) = A_0 + A_1 e^{\alpha_F t} + A_2 e^{\alpha_S t} \qquad (3.10)$$

where

$$A_0 = C$$
$$A_1 = -\frac{E\overline{\nu(\nu-1)}}{4\tau_f^2}\frac{3\alpha_F + \alpha_S}{\alpha_F(\alpha_F + \alpha_S)} \qquad (3.11)$$
$$A_2 = -\frac{E\overline{\nu(\nu-1)}}{4\tau_f^2}\frac{3\alpha_S + \alpha_F}{\alpha_S(\alpha_F + \alpha_S)}$$

The two-region Rossi-alpha equation reveals the sum-of-two-exponentials behavior expected from a coupled system when the transit time is ignored. If the transit time were to be considered,

the Rossi-alpha equation would contain four exponentials; however, the ability to observe the decay constants associated with the transit time is questionable at best [23].

For an asymmetrical system, the Rossi-alpha equation is:

$$p\left(t\right)dt = Cdt + \frac{E\overline{\nu\left(\nu-1\right)}}{4\tau_f^2 D^2}\left[\left(\frac{AB}{\alpha_F+\alpha_S}-\frac{A^2}{2\alpha_F}\right)e^{\alpha_F t} + \left(\frac{AB}{\alpha_F+\alpha_S}-\frac{B^2}{2\alpha_S}\right)e^{\alpha_S t}\right]dt \quad (3.12)$$

where

$$A = \alpha_S - \alpha_1$$
$$B = \alpha_F - \alpha_1 \quad (3.13)$$
$$D = \alpha_S - \alpha_F$$

and α_1 is the prompt neutron decay constant for the isolated Region 1. The full derivation for the asymmetrical case is provided in Appendix B.

3.3 Rossi-Alpha Measurements

Rossi-alpha measurements are simple to perform but require slightly complex analysis of the resulting counts. The data are divided up into time windows on the order of the average neutron chain length. Within each window, the time difference Δt between two counts is determined and binned based on a pre-selected time bin width. A smaller Δt between two counts indicates a higher likelihood that those counts are correlated in time and therefore came from the same initial fission event. The histogram created by these data is fitted with a single exponential function if the system follows single-point kinetics or a sum-of-two-exponentials function if the system follows coupled-core kinetics (without transit time considerations). It is common for the histogram for a single-point system to be plotted on a log-log scale such that the data can be fit with a straight line, making for simpler analysis. This is no longer possible when more than one exponential is involved since the function can no longer be linearized and a nonlinear least squares fit method
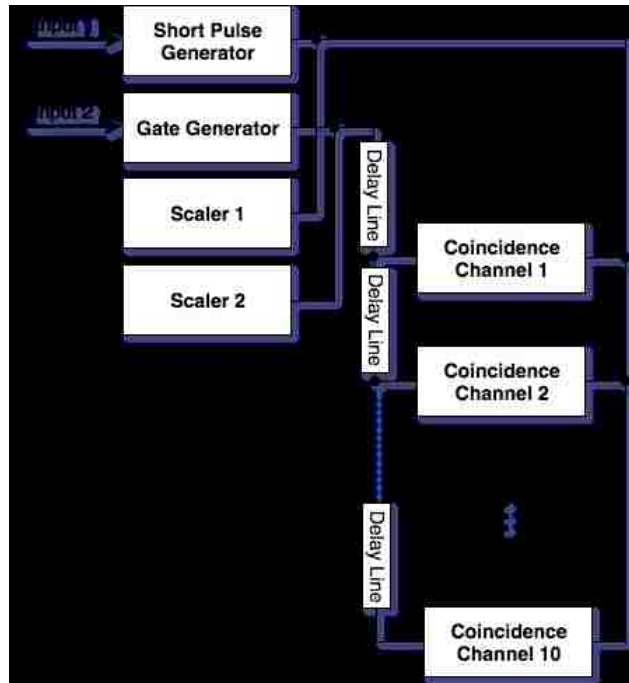
Figure 3.1: Detection system schematic of the time analyzer for a historical Rossi-alpha measurement.

must be used instead.

3.3.1 List-Mode Data

Historical Rossi-alpha measurements had to rely on best estimates for the time bin width and were limited by the capabilities of the instrumentation. Time window sizes and time bin widths were predetermined and were set using gating hardware; therefore, only a single analysis method and a single time window and time bin width could be applied to each measurement. Orndoff said the time bin width should be "some fraction of $l/(1 - k_p)$," where l is the prompt neutron lifetime and k_P is the prompt multiplication factor. In Orndoff's analyzer, e.g., ten channels, each of a predetermined time bin width of either $0.25\,\mu s$ or $0.5\,\mu s$, recorded the counts from the multiplying system. The time window width was therefore limited to either $250\,\mu s$ or $500\,\mu s$. Fig. 3.1 shows Orndoff's analyzer for the original Rossi-alpha measurements [53].

Modern detection systems record list-mode data, which involves assigning a time stamp relative
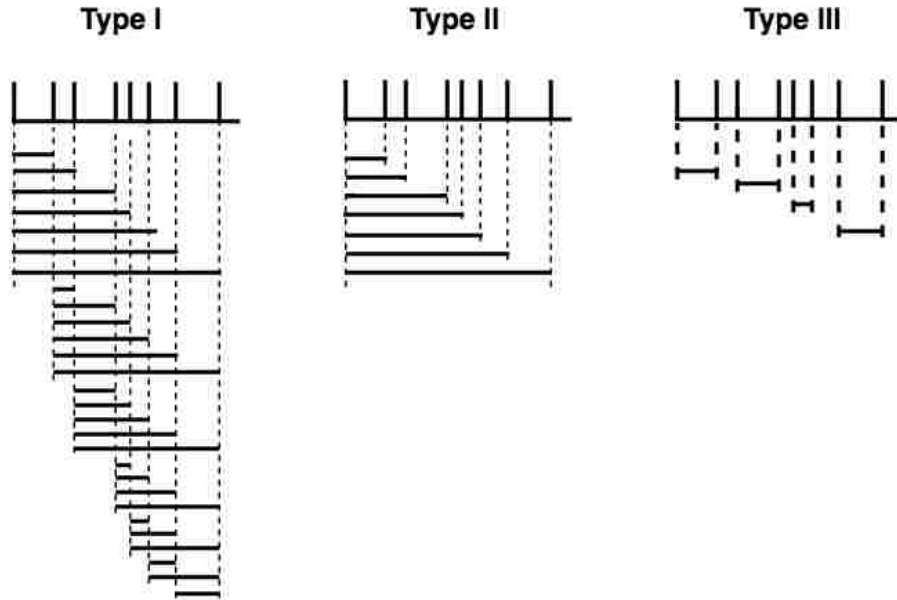
Figure 3.2: Type I, II and III binning methods.

to the start of the measurement to each detector pulse. These systems are often limited by the tick size; for example, the LANL list-mode module has a tick size of $100\,\text{ns}$ [54]. The tick size determines the minimum time bin width that can be used.

3.3.2 Type I, II and III Binning Methods

List-mode data not only allow for the analysis method to be chosen at a later time, it also facilitates the selection of the binning method and optimal bin size for Rossi-alpha measurements. There are three types of binning techniques used in Rossi-alpha analysis, labeled Type I, II and III binning [55]. Figure 3.2 provides a visual comparison of all three methods.

With Type I binning, a new time window is opened for each count such that there might be a lot of overlap of time windows. Since it is unknown which counts are due to fission events and which counts are not, this method arguably provides the most statistically sound results by providing the most thorough combing of the data.

Type II binning is similar to Type I, except that the next time window is not opened until immediately after the previous one closes. Both Type II and Type I binning methods will provide

the same alpha values according to Hansen; however, the coefficient(s) in front of the exponential term(s) will be smaller for the Type II method [55].

Type III binning is the method historically used [56], but it is also the least efficient and it can lead to deviations from the true value of alpha [55]. The first count triggers the time window to open, the next count closes the window, and the time difference between the two counts is recorded. A new window is not opened again until after the next sequential count arrives. This process is repeated until the end of the total measurement time is reached. Unlike the other two binning methods, no fixed time window is used in this method.

Chapter 4

Computational Analysis for Predicting the Coupled-Core Prompt Neutron Decay Constants and Coupling Time Constants

One of the primary focuses of this research is to determine the predictive capabilities of the Los Alamos National Laboratory's MCNP6 code for loosely-coupled reactor behavior. Computational analysis for predicting the prompt neutron decay constants with MCNP6 is accomplished by running a simulation of the full system in analog mode and parsing the time-stamped counts (list-mode data) from the output. The simulated list-mode data are processed in the same manner as the measured data and the prompt neutron decay constants are obtained. This process is repeated with each region in isolation to determine the regional decay constants. A set of criticality calculations are run with the kinetics option and tallies invoked to gather kinetics parameters. A tally ratio is also obtained from which the individual coupling time constants can be teased out of the results from the first simulation. This process will be explained in further detail.

4.1   MCNP®6

The MCNP (Monte Carlo N-Particle) version 6.1.1 code was used for the neutron transport simulations in this research [57]. MCNP6 is a three-dimensional continuous-energy Monte Carlo radiation transport code developed at Los Alamos National Laboratory that can simulate a variety of problems from power reactor design to shielding to radiation dosimetry. It has been heavily

benchmarked for both criticality and fixed-source calculations.

Monte Carlo particle transport codes such as `MCNP6` determine various integral parameters by tracking a number of individual particles from birth to death until an adequate number has been sampled. As an example, in a nuclear reactor system, a source neutron enters the system and causes a fission event from which several neutrons are born. A Monte Carlo code banks all but one of those neutrons for tracking at a later time. The unbanked neutron is then followed through its lifetime within the system and its various reactions with matter are analyzed. The distance traveled and each interaction are sampled from probability distributions obtained from a nuclear data library such as the widely-used Evaluated Nuclear Data File (ENDF) library or from physics models. The neutron will continue to be tracked until it crosses the problem boundary; i.e., it "leaks" from the system or it is absorbed, at which point it is "killed." Once the neutron is terminated in either of these situations, the next neutron is pulled from the particle bank and tracked in the same manner. Though each particle experiences a very different series of events within the system, the average behavior of the particles can be extracted when a large number of particle lifetimes are simulated.

The `ptrac` (Particle TRACk) option in `MCNP6` allows the user to choose from a variety of outputs that can be printed to a separate file including time-tagged events such as neutron captures in a Helium-3 detector or proton-recoil events in a plastic scintillator. In the present analysis, a direct comparison to measured data was desired, so analog tracking was selected such that pure time-tagged counts would be recorded in the `ptrac` output file. The `ptrac` file must be written in binary format; the time stamps suffer from significant truncation in the ASCII output and are not suitable for neutron noise analysis methods [58].

A simulation utilizing the `ptrac` option cannot be run in message-passing interface (MPI) mode. This would usually render the option unusable for even the simplest problems because the run time for an analog problem would be on the scale of days or weeks, but an in-house perturbation code, `mcnp_pstudy` [59], was developed that has the capability of breaking up an `MCNP6` problem and running brute-force "in parallel" calculations. Division of the problem with `mcnp_pstudy` results in multiple `ptrac` output files which must then be parsed and combined
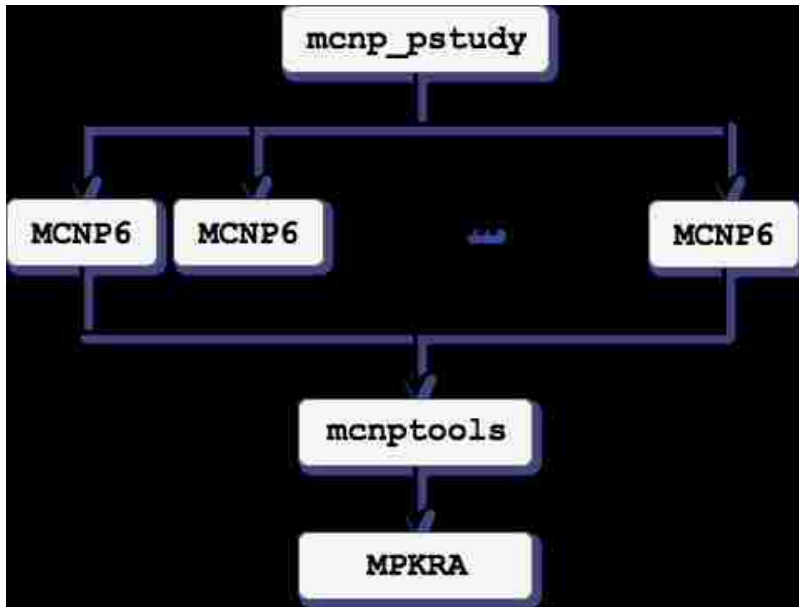
Figure 4.1: Workflow for MCNP6 simulation of list-mode data for Rossi-alpha analysis.

into a single list-mode-like data file. List-mode files contain two columns of data: the first column lists the cell number where the event of interest occurred (i.e., the detector volume) and the second column lists the time stamp when the event occurred. This is accomplished with mcnptools, a post-processing toolkit that allows not only ptrac files but also MCNP6's mctal and meshtal files to be easily processed [60]. The time stamp for each count and the cell number where each count occurred is parsed from the ptrac file and saved to a text file in ASCII format.

Once the list-mode file is created, it is processed through a multipoint kinetics Rossi-alpha code, described in the next section, that was developed for this research. The data are nearly identical to measured data except that the simulated data do not experience a detector dead time nor are the time stamps limited by the resolution of the detection system. The simulated counts could be considered those from a "perfect" or "ideal" measurement. However, these data are processed in the same way as measured data; it is expected that the results will be more precise, but accuracy depends on the quality of the nuclear data libraries and physics models used. A visual description of the workflow is shown in Figure 4.1.

4.2   Rossi-Alpha List-Mode Data Processing Code `MPKRA`

The list-mode data files were processed using multipoint Rossi-alpha analysis with the Multi-Point Kinetics Rossi-Alpha (`MPKRA`) code.

4.2.1   Description of `MPKRA`

The `MPKRA` code, included in Appendix C, was written in `Python` and was developed to process the list-mode data files, calculate the time differences between counts, bin the time differences to create a histogram, and fit to it a sum-of-exponentials curve with the user's choice of the number of exponentials (up to three exponentials can be fit at this time). The user provides the name of the list-mode file to be processed, the total measurement time in seconds, the time window width and time bin width, both in microseconds, and the number of exponentials to fit. A second option within the code will run the data through a number of different time bin widths and output the results to a text file. The optimal time bin width can then be determined by the user. This option omits the histogram plots.

Measured data are recorded sequentially in time; however, `MCNP6 ptrac` data are not sequential since `MCNP6` tracks an individual particle throughout its entire lifetime and records data before tracking the next banked particle. The data in the list-mode file output generated from the `MCNP6` simulation must first be ordered sequentially in time before Rossi-alpha analysis can be performed. Once the data are ordered, the code selects the first count, starts the time window, and calculates the time difference between the first count and each subsequent count until the end of the time window is reached. It moves to the next sequential count after the first count and repeats the process for a new time window (Type I binning). This is repeated until the end of the data file is reached. The time differences are binned based on the pre-selected time bin width and are then plotted in a histogram like the one shown in Figure 4.2

The nonlinear least-squares fit (NLSQ) of the histogram is accomplished in two steps. The Levenberg-Marquardt method, which is the method used by `Python`'s `curve_fit` package [61],

is used to fit a sum-of-exponentials curve to the data; however, this method requires a fairly accurate initial guess for the fit parameters, which are assumed to be unknown in the Rossi-alpha analysis. The data are converted to Legendre-space to obtain an initial guess for the parameters from a similar curve fit [62]. The results from the Legendre fit are not used because the fit is sometimes susceptible to oscillations at the ends of the plot, which puts the accuracy of the results in doubt.

Once the initial guesses are obtained, they can be input into `curve_fit` to determine the best sum-of-exponentials fit for the data. The error of each fit parameter is assumed to be one standard deviation which is calculated from the covariance matrix. The process from binning to best fit is repeated for various time bin widths.

4.2.2 Computing Hardware

All of the `MCNP6` simulations were run on LANL's Moonlight cluster. Moonlight consists of 308 compute nodes; each node contains two Eight Core Intel Xeon SandyBridge E5-2607 2.6 GHz processors for a total of 16 cores per node. There are 32 GB of RAM available to each node. Each node also houses two Nvidia Tesla M2090 GPU cards to increase the computing power. In total, Moonlight's peak computing performance is 488 teraflops.

Most jobs are limited to 8-hour run times, therefore the use of `mcnp_pstudy` to break up a `ptrac` simulation was essential in completing the simulations for this research. For each simulation, anywhere from 16 cores (1 node) to 200 cores (~13 nodes) were used depending on the complexity of the model, the measurement time, and the modeled system's proximity to delayed critical.

Once the runs were finished and the `ptrac` files were converted into ASCII list-mode files using `mcnptools`, they were transferred to a MacBook Air with a 2.2 GHz Intel Core i7 and 8GB RAM for processing with `MPKRA`. This system can handle between 5e6 to 20e6 counts, depending on the count rate of the original simulation, with the `MPKRA` code in its current configuration. The system lacks the memory to handle larger data sets. This was a good test in computational

46
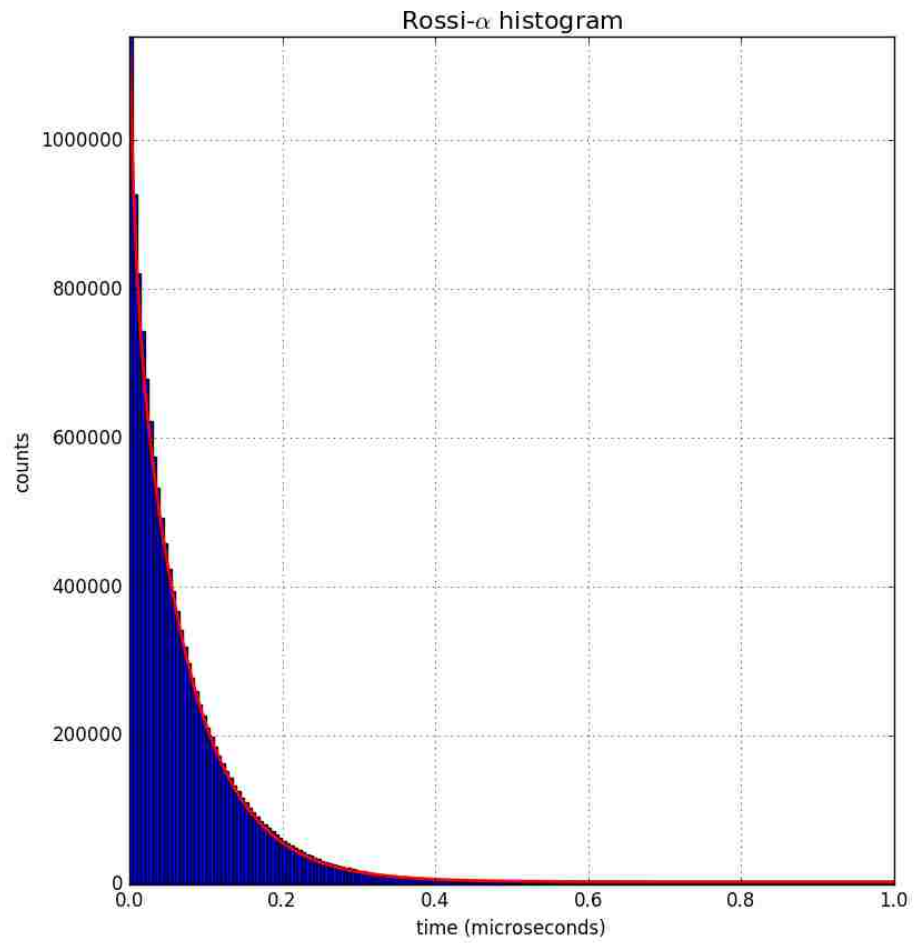
Figure 4.2: A sample Rossi-alpha histogram plot generated by the MPKRA code.

Prompt Neutron Decay Constant (10^4 inverse seconds)				
Benchmark	Measurement	MCNP5 (Mosteller)	MCNP6 kopts	MCNP6 ptrac
Jezebel-Pu	-64 ± 1	-65 ± 1	-63 ± 1	-65.082 ± 0.004
Jezebel-U233	-100 ± 1	-108 ± 1	-103 ± 2	-109.525 ± 0.009
THOR	-19 ± 1	-20 ± 1	-21.0 ± 0.4	-19.48 ± 0.02

Table 4.1: Benchmark results for `MPKRA` using `MCNP6`/`ptrac` results.

capability since noise analysis is used in field measurements where a small portable computer may be the only thing available if rapid analysis is desired.

4.2.3 `MPKRA` Benchmarking

The results from `MPKRA` are compared to several of the delayed critical benchmarks listed in [63] to verify that the code is processing the list-mode data and performing the Rossi-alpha binning and data fit correctly. Each benchmark model was run as a `kcode` criticality calculation with the `kopts` option invoked and separately as a fixed source calculation with the `ptrac` option enabled. The `kopts` point kinetics option calculates the system-wide kinetics parameters β_{eff}, Λ and the delayed critical α_{DC}. The results of the `MCNP6`/`kopts` and `MCNP6`/`ptrac` simulations using ENDF/B-VII.0 are compared to the historical measurements and Mosteller's `MCNP5` 1.60/`kopts`/ENDF/B-VII.0 simulation results in Table 4.1. The results obtained from the `ptrac` method agree quite well with the values from the benchmarks.

4.3 Effect of the Time Bin Width on the Determination of the Prompt Neutron Decay Constants

For many systems near delayed critical or in which the prompt neutron decay constant is "slow," e.g., large or thermal systems, the size of the time bin has a minimal effect on the determination of the decay constant. However, the observation of faster prompt neutron decay constants, such as those seen in highly subcritical bare metal single-region systems, can be quite dependent on the

Prompt Neutron Decay Constant (μsec^{-1})			
Density (g/cm^3)	kcode	ptrac	C/E
19.604	-136.550 ± 0.005	-127.90 ± 0.02	1.068
20.0	-125.714 ± 0.005	-129 ± 1	0.974
21.0	-104.956 ± 0.004	-104.06 ± 0.07	1.009
22.0	-83.371 ± 0.004	-83.90 ± 0.04	0.994
23.0	-63.591 ± 0.005	-65.1 ± 0.2	0.977
24.0	-43.289 ± 0.005	-43.95 ± 0.09	0.985
25.0	-23.511 ± 0.006	-24.30 ± 0.02	0.967
26.0	-4.15 ± 0.03	-5.170 ± 0.004	0.803

Table 4.2: Comparison of the prompt neutron decay constants determined from `kcode` and from Rossi-alpha analysis of `ptrac` list-mode data using the optimum time bin width for various artificial densities of a plutonium sphere.

time bin width as can be seen in Figure 4.3. In this example, the density of a plutonium sphere was artificially varied to modify the subcritical level (density was chosen as the parameter for modification so that differences in the leakage rates due to geometry changes could be avoided). The resulting prompt neutron decay constant was plotted for two constant time bin widths, chosen to be $0.25\,\mu$s from historical measurements and $0.025\,\mu$s, and for the optimal time bin width (selection of the optimal time bin width will be discussed later). The decay constants agree well when the plutonium sphere is more dense (closer to critical), but when it becomes "deeply subcritical," the decay constant found from the $0.25\,\mu$s-binned data deviates significantly from the "true" value and falsely levels out at a constant decay constant for the more subcritical cases. The $0.025\,\mu$s-binned data provide a better estimate of the decay constant; however, the magnitude of the decay constant is underestimated for the more subcritical cases and the difference increases with subcriticality. The "optimal" time bin widths, which are around 0.001 to $0.005\,\mu$s for these cases, estimate decay constants very close to those inferred from `kcode` calculations. Table 4.2 compares the decay constant found by minimizing the fit error to the decay constant calculated from the equation $\alpha = \frac{k(1-\beta)-1}{k\Lambda}$ using values for k, β and Λ from `MCNP6` `kcode` calculations with the `kopts` kinetics option invoked.

Figure 4.4 shows the "measured" value of the prompt neutron decay constant as a function of the size of the time bin width for the plutonium sphere density cases. The decay constant increases
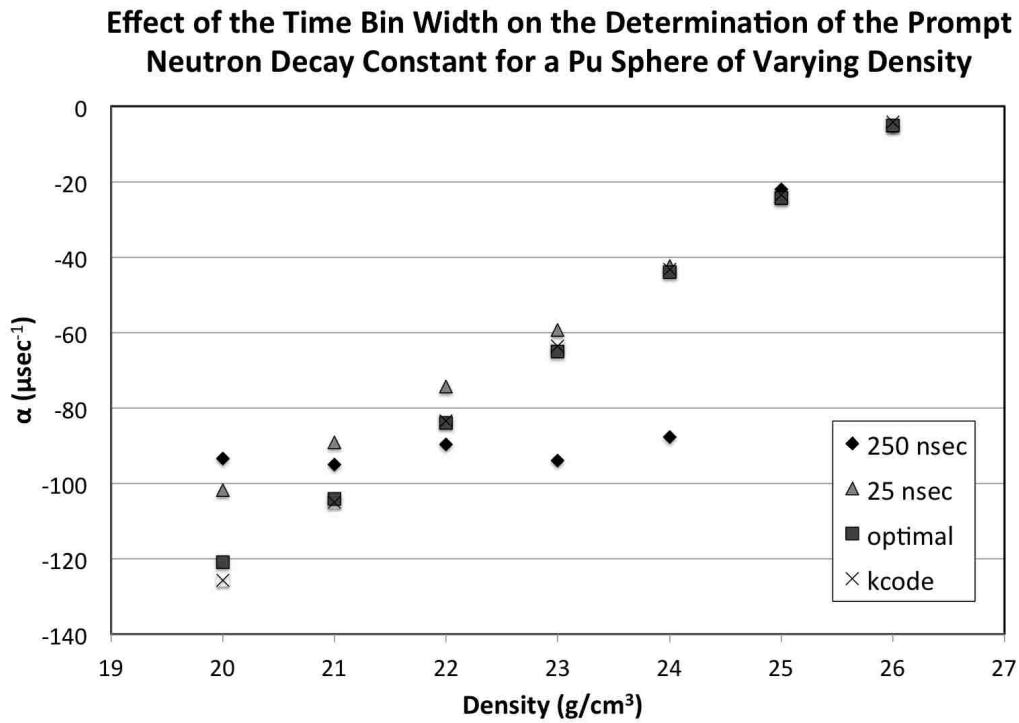
Figure 4.3: Prompt neutron decay constants determined using the optimal bin width and $0.25\,\mu s$ and $0.025\,\mu s$ bin widths for various artificial densities of a plutonium sphere.

Predicted Prompt Neutron Decay Constant as a Function of the Time Bin Width for a Pu Sphere of Various Densities
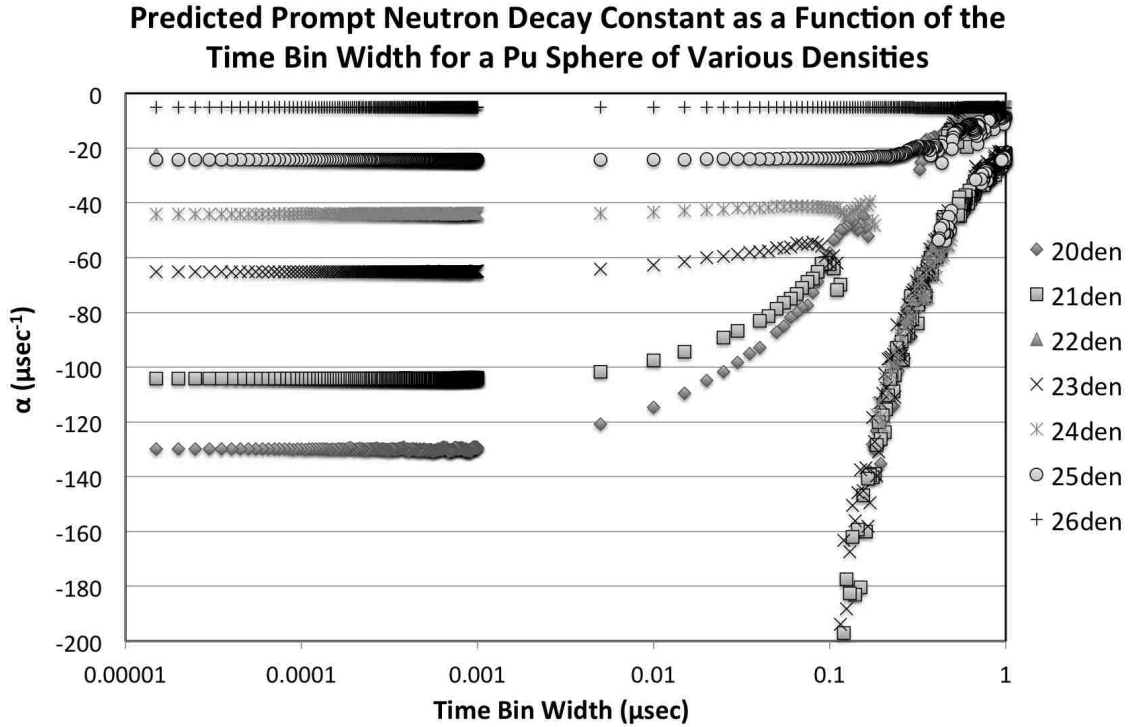
Figure 4.4: Effect of time bin width for varying levels of subcriticality for a plutonium sphere.

in magnitude as the bin size decreases until it levels out at the correct value. The deeper the subcriticality, the smaller the time bin width needed to obtain the correct decay constant.

4.4 Computational Analysis of Symmetrical and Asymmetrical HEU Cylinders

An initial study of the feasibility of using the `MCNP6/ptrac` method for predicting the response expected in a Rossi-alpha measurement of a coupled bare metal system was performed. For this, the coupled highly enriched uranium (HEU) cylinders experiments by J. Mihalczo [1] were simulated. These experiments were chosen because they are one of the few measurements of a coupled subcritical bare metal system conducted and they are similar to the planned experiment that will be described in the next chapter.

Simplified versions of the experiments were modeled in `MCNP6`: they include the two HEU
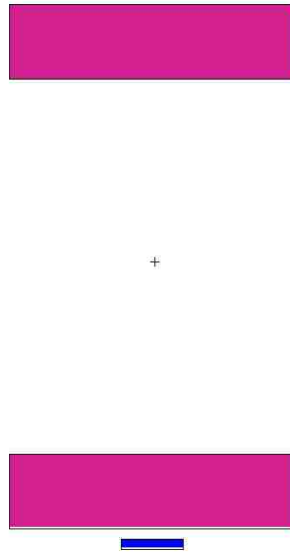
Figure 4.5: `MCNP 6` model of the symmetrical HEU cylinders experiment.

cylinders without the support structure, a point source emitting 10^7 neutrons per second located 1.0 cm above the center of the upper cylinder, and a 6.0 cm long by 6.0 cm wide by 1.0 cm thick neutron absorption detector located 1.0 cm below the center of the lower cylinder as shown in Figure 4.5. The density of the detector was artificially increased to obtain enough counts in a reasonable amount of simulation time.

Several asymmetrical configurations were also modeled to observe the expected behavior for an asymmetrical system and to test methods for the determination of the coupling coefficients. The diameter of the upper cylinder was modeled at 20.0, 24.0, 32.0 and 36.0 cm while the lower cylinder was kept at a constant 27.94 cm in the first set. In the second set, the lower cylinder retained a thickness of 7.314 cm while the upper cylinder was modeled at 8.0, 7.0, 6.314, and 5.314 cm.

Each simulation was run for a 300 second "count time." Anywhere from 1.5e7 counts for the most subcritical system to 2.5e8 counts for the least subcritical system were recorded. The deeper the subcritical level, the longer the count time needed to observe the correct prompt neutron decay constants; ideally, the cases with the most separation and/or the least amount of mass should have

	α_{iso} (μsec^{-1})		
Experiment	Measured	MCNP6/ptrac	C/E
8.255 cm	-5.05	-5.168 ± 0.002	1.02
7.314 cm	-16.70	-17.15 ± 0.02	1.03
6.676 cm	-25.26	-25.85 ± 0.02	1.02
6.042 cm	-34.55	-36.65 ± 0.03	1.06

Table 4.3: Prompt neutron decay constant for an isolated HEU cylinder determined from historical measurements [1] and from MCNP6/ptrac simulations.

longer count times.

4.4.1 Results for the Symmetrical HEU Cylinders

It was mentioned in Chapter 1 that two methods were used to measure the decay constants. The first method involved placing two detectors on the same region and fitting a sum-of-two-exponentials curve to the data. The second method required first measuring the slower decay constant by placing a detector on each cylinder and fitting a single exponential curve to the data. The faster decay constant was then determined from a measurement similar to that performed for the first method; the slower decay constant was plugged in to the sum-of-two-exponentials fit and the resulting faster decay constant was determined. The first method shall be referred to as Method A and the second shall be Method B. Method A was used in the MCNP6/ptrac simulations.

A comparison of the MCNP6/ptrac results to the original measurements are shown in Tables 4.3 through 4.5. Table 4.3 shows good agreement between the ptrac results and the measured values for a single HEU cylinder from each configuration. The results inferred from the ptrac calculations for the coupled configurations using Method A are much closer to the results obtained from Mihalczo's measurements using Method B. The discrepancies between the measured and the ptrac results can be explained by the effect of the size of the time bin width described earlier. Mihalczo's instrumentation was limited to $0.25\,\mu$s bin widths, which was shown to result in underestimation of the magnitude of the decay constants as subcriticality increased.

	α_S (μsec^{-1})		
Experiment	Measured - Method A	Measured - Method B	MCNP6/ptrac
8.255 cm	-0.932 ± 0.008	—	-1.5083 ± 0.0007
7.314 cm	-9.90 ± 0.24	-10.34 ± 0.07	$-11.01 \pm .06$
6.676 cm	-15.29 ± 0.58	-15.73 ± 0.09	-16.80 ± 0.05
6.042 cm	-17.58 ± 1.79	-21.18 ± 0.48	-22.1 ± 0.2

Table 4.4: Slower prompt neutron decay constant from historical measurements [1] and from MCNP6/ptrac.

	α_F (μsec^{-1})		
Experiment	Measured - Method A	Measured - Method B	MCNP6/ptrac
8.255 cm	—	—	-10.92 ± 0.05
7.314 cm	-20.40 ± 1.47	-23.41 ± 0.69	-28.3 ± 0.4
6.676 cm	-33.9 ± 2.3	-35.71 ± 1.06	-38.4 ± 0.2
6.042 cm	-36.31 ± 2.72	-44.29 ± 2.1	-48.9 ± 0.4

Table 4.5: Faster prompt neutron decay constant from historical measurements [1] and from MCNP6/ptrac.

The coupling time constants for the symmetrical system are easy to determine using Equation 2.32. The coupling constants determined from the slower prompt neutron decay constant for the four original symmetrical cases are shown in Table 4.6 along with the measured values. The coupling time constants listed in [1] were inferred from the coupling coefficients, ϵ, which were determined from a Monte Carlo calculation. In the previous research, it was assumed that ϵ could be determined by calculating the difference between the system of interest and a reference system of the same diameter and separation distance at delayed critical.

$\gamma\ (\mu sec^{-1})$		
Cylinder Thickness (cm)	Measured	`MCNP6`/`ptrac`
8.255	3.950	3.660 ± 0.002
7.314	4.117	6.14 ± 0.06
6.676	4.188	9.05 ± 0.05
6.042	4.278	14.6 ± 0.2

Table 4.6: Comparison of the coupling time constant determined from `MCNP6`/`ptrac` calculations for the measured symmetrical cases from [1].

4.4.2 Comparison of the Prompt Neutron Decay Constants and Coupling Time Constants Determined from **kcode** and from **ptrac** Calculations for Symmetrical HEU Cylinders

In light of the differences between the values of the coupling constants reported in [1] and those inferred from the `ptrac` simulations, the prompt neutron decay constants and the coupling time constants inferred from `MCNP6` criticality calculations are compared to those computed from the `ptrac` simulations for the symmetrical HEU cylinders. For the `kcode` method, the following equations were used to determine the parameters:

$$\alpha_j = \frac{k_j - 1}{k_j \Lambda_j} - \frac{\beta_{j,eff}}{\Lambda_j} \tag{4.1}$$

$$\gamma_{jk} = \frac{k_{jk}\left(1 - \beta_{j,eff}\right)}{k_j \Lambda_j} \tag{4.2}$$

where $k_{jk} = k_{eff} - k_j$, k_{eff} is the effective multiplication factor for the coupled system and k_j is the multiplication factor for the isolated Region j. The slower and faster prompt neutron decay constants are found from Equation 2.32.

Figure 4.6 shows that the difference between the prompt neutron decay constants for the isolated cylinders from the eigenvalue calculation and from the `ptrac` calculation are not very significant, indicating that the prompt neutron decay constant determined from a `kcode` calculation may be an acceptable estimate of the prompt neutron decay constant for single-region systems
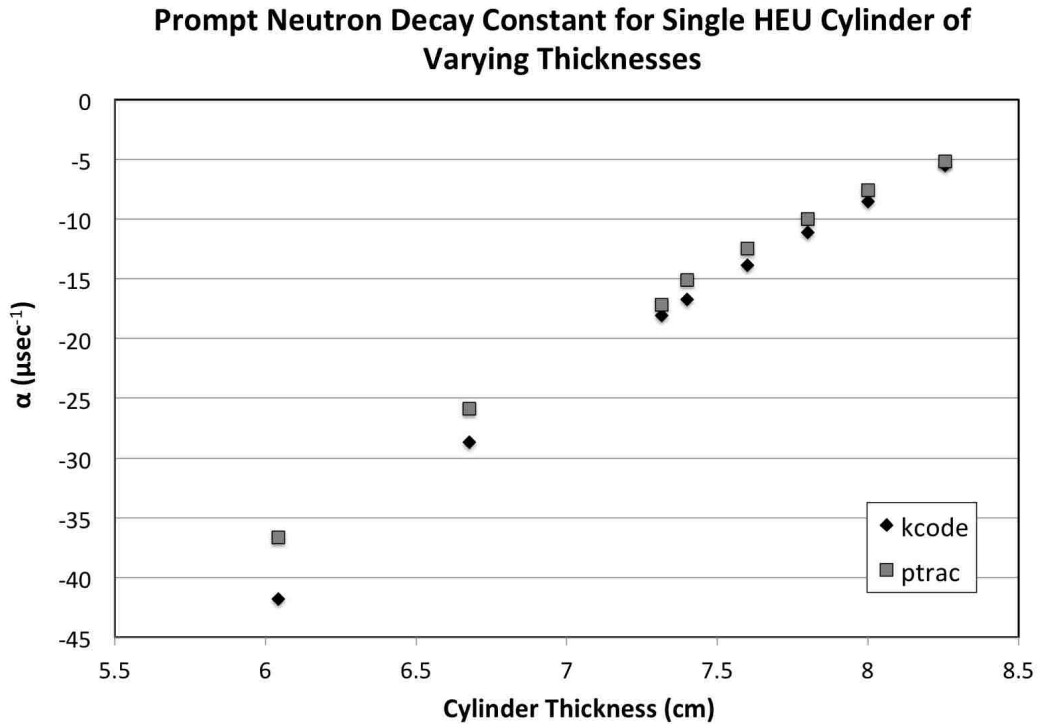
Figure 4.6: Comparison of the prompt neutron decay constant for an isolated cylinder inferred from `kcode` and from `ptrac` simulations for varying HEU cylinder thicknesses.

above an effective multiplication of about 0.9 (this was also shown in the Pu sphere density cases described earlier: the `kcode` results matched the optimal time bin width results quite well up to an effective multiplication of around 0.8). Extra cases between the critical configuration and the 7.314 cm case are included to show the growth in the deviation as the system becomes more subcritical.

The difference between the results from each method are more significant when the coupled system is considered. The results for the critical configuration (8.255 cm) agree quite well; however, as the system becomes more subcritical, the slower decay constant determined from the `kcode` method increases in magnitude much more rapidly than that determined via the `ptrac` method while the faster decay constant decreases as seen in Figure 4.7. The slower prompt neutron decay constant exhibits a difference of nearly 70% between the `kcode` and the `ptrac` values for the most subcritical configuration.

The difference is amplified in the coupling constants as shown in Figure 4.8. If the coupling
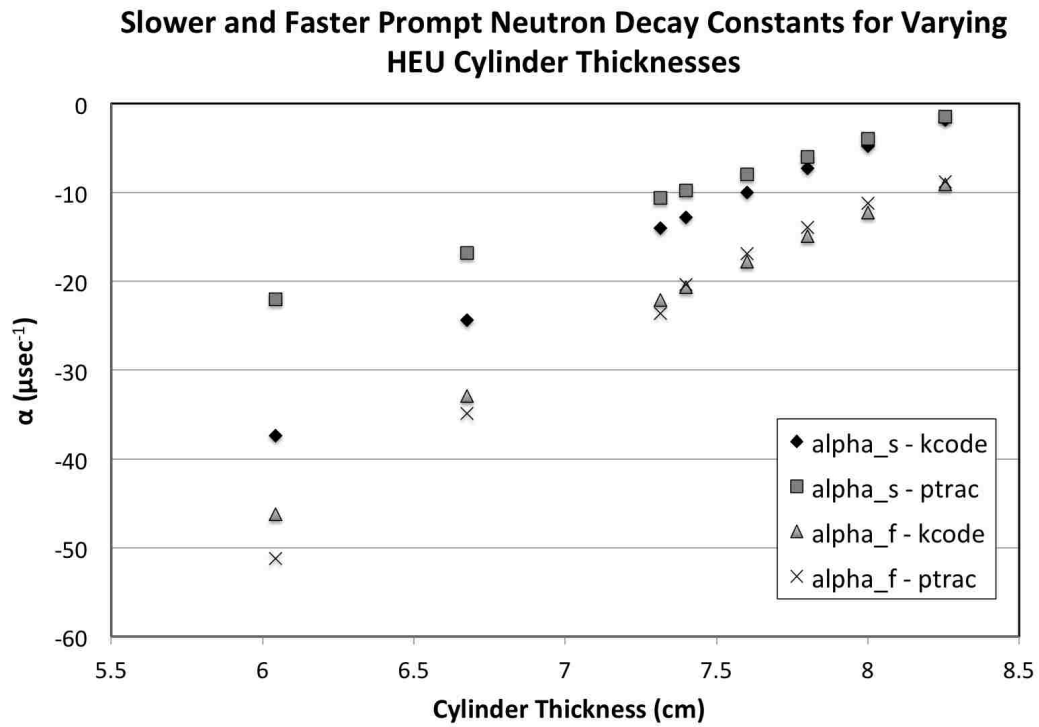
Figure 4.7: Comparison of the slower and the faster prompt neutron decay constants inferred from `kcode` and from `ptrac` simulations for varying HEU cylinder thicknesses.

	γ (μsec^{-1})			
Experiment	Measured	Meas - from α_S	ptrac	kcode
8.255 cm	3.95	—	3.660 ± 0.004	3.66 ± 0.01
7.314 cm	4.117	6.8	6.14 ± 0.07	4.02 ± 0.01
6.676 cm	4.188	9.97	9.05 ± 0.06	4.22 ± 0.01
6.042 cm	4.278	16.97	14.6 ± 0.2	4.87 ± 0.01

Table 4.7: Coupling time constants from historical measurements [1] and from MCNP6 ptrac and kcode calculations.

constants reported in [1] had been calculated using the same method used in this research, the results would be much closer to those listed for the ptrac method, as shown in Table 4.7.

4.4.3 Comparison of Multipoint and Single-Point Kinetics for Symmetrical Cylinders

For the critical configuration, the slower decay constant found using multipoint kinetics and the decay constant determined using single-point kinetics are nearly equivalent, which could cause one to think that the system can be adequately described by single-point kinetics and that the faster decay constant is merely a higher spatial harmonic. However, as the cylinder thickness decreases and the system becomes more subcritical and more loosely coupled, the single-point kinetics decay constant increases in magnitude faster than the slower multipoint kinetics decay constant. At 12.94 cm of separation, the assembly has a k_{eff} of 0.99864, and at 36.94 cm, it is reduced to 0.93319. This behavior is visually represented in Figure 4.9

Figure 4.10 shows the same trend between the slower decay constant from multipoint kinetics analysis and the single decay constant from single-point kinetics as the separation distance increases between the two 7.314 cm thick cylinders.

4.4.4 Results for the Asymmetrical HEU Cylinders

Two different sets of asymmetrical configurations were analyzed to thoroughly observe the effects of asymmetry on the prompt neutron decay constants. In the first set, the diameter of the upper

Plot of the Coupling Time Constants for Varying HEU Cylinder Thickness
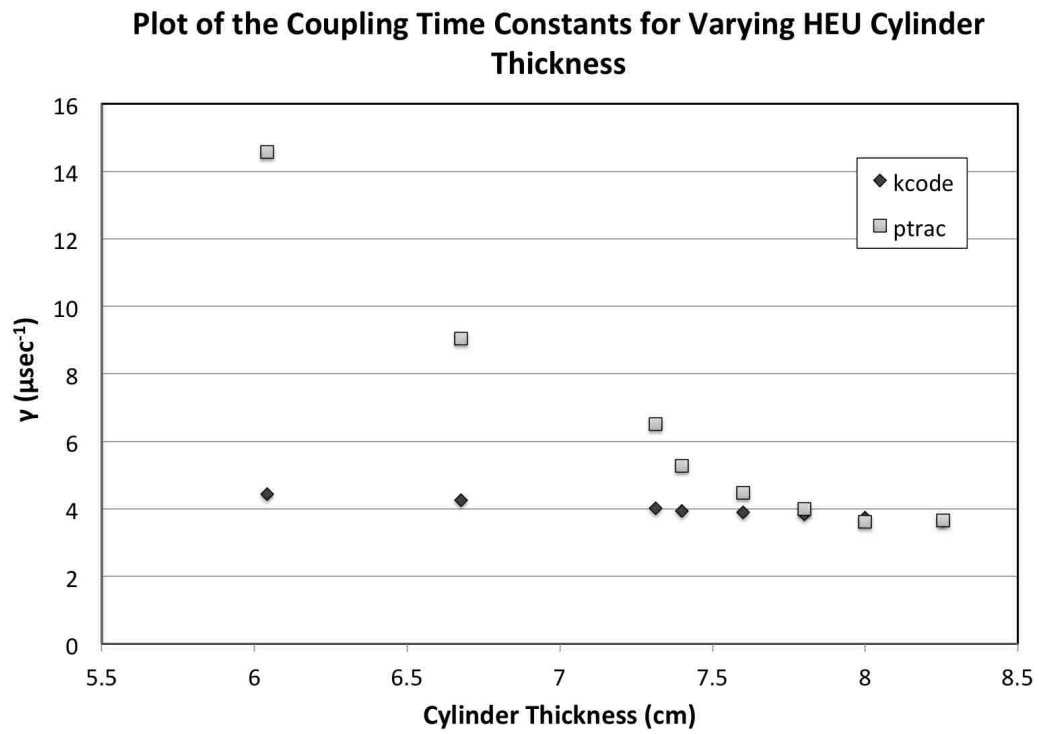
Figure 4.8: Comparison of the coupling time constants inferred from `kcode` and from `ptrac` simulations for varying cylinder thicknesses for the symmetrical HEU cylinders.
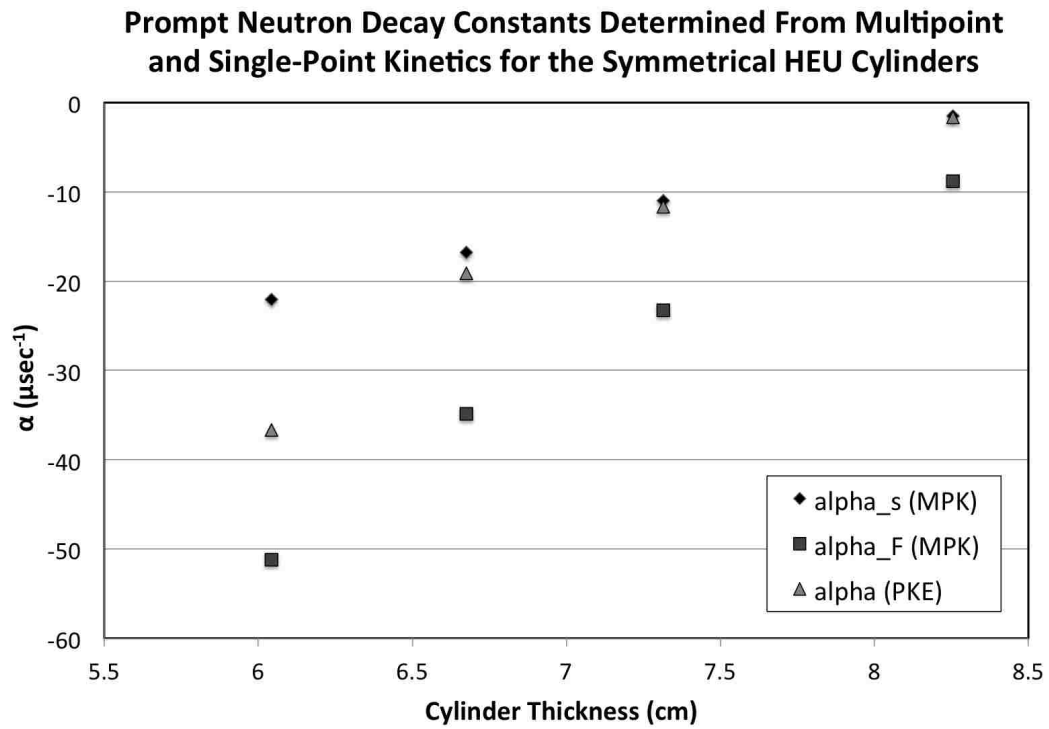
Figure 4.9: Comparison of the prompt neutron decay constants determined using multipoint kinetics and single-point kinetics for the measured symmetrical configurations.

Slower MPK and PKE Prompt Neutron Decay Constants as a Function of Separation Distance, Symmetrical HEU Cylinders
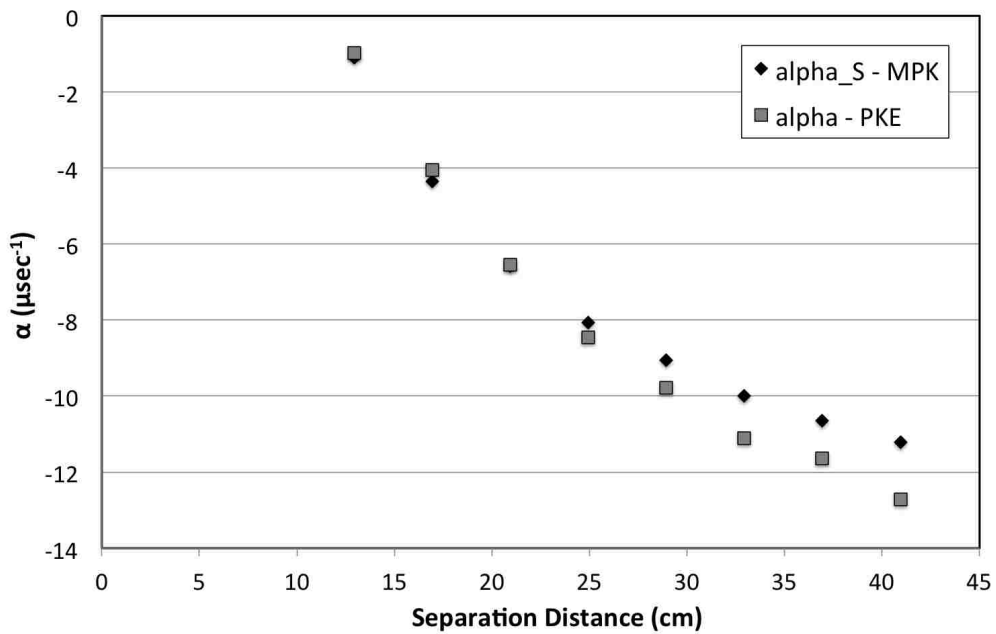
Figure 4.10: Comparison of the prompt neutron decay constants determined using multipoint kinetics and single-point kinetics for the measured symmetrical configurations.

Upper Cylinder Diameter (cm)	k_{eff}	α_S (μsec^{-1})	α_F (μsec^{-1})
20.0	0.91510	-14.928 ± 0.009	-49.6 ± 0.4
24.0	0.92009	-13.13 ± 0.02	-32.4 ± 0.2
27.94 (symm)	0.93319	-11.01 ± 0.06	-28.3 ± 0.4
32.0	0.95275	-7.761 ± 0.005	-24.08 ± 0.03
36.0	0.97066	-5.190 ± 0.002	-22.84 ± 0.02

Table 4.8: Prompt neutron decay constants for the asymmetrical configurations with the diameter of the upper cylinder modified.

cylinder was modified while that of the lower cylinder was held at a constant 27.94 cm for the 7.314 cm thick cylinders. For the second set, the thickness of the upper cylinder was varied while that of the lower cylinder was kept at 7.314 cm. The separation distance for all cases was 36.94 cm.

The prompt neutron decay constants for the cases in which the diameter of the upper cylinder was changed are shown in Table 4.8 and Figure 4.11. As the asymmetry increases, the difference between the faster and the slower decay constants increases. As the subcriticality increases, the faster decay constant increases in magnitude faster while the slower decay constant experiences a decrease in the rate of growth of its magnitude.

Similarly, the prompt neutron decay constants for the configurations in which the thickness of the upper cylinder was modified differ more as the asymmetry increases. Unlike the modified diameter cases, the faster decay constant appears to follow more of a straight-line trend as the system becomes more subcritical. More cases should be run to determine whether the faster decay constant for the 5.314 cm case is an outlier or truly representative of the behavior of the system. The decay constants for the modified thickness configurations are shown in Table 4.9 and Figure 4.12.
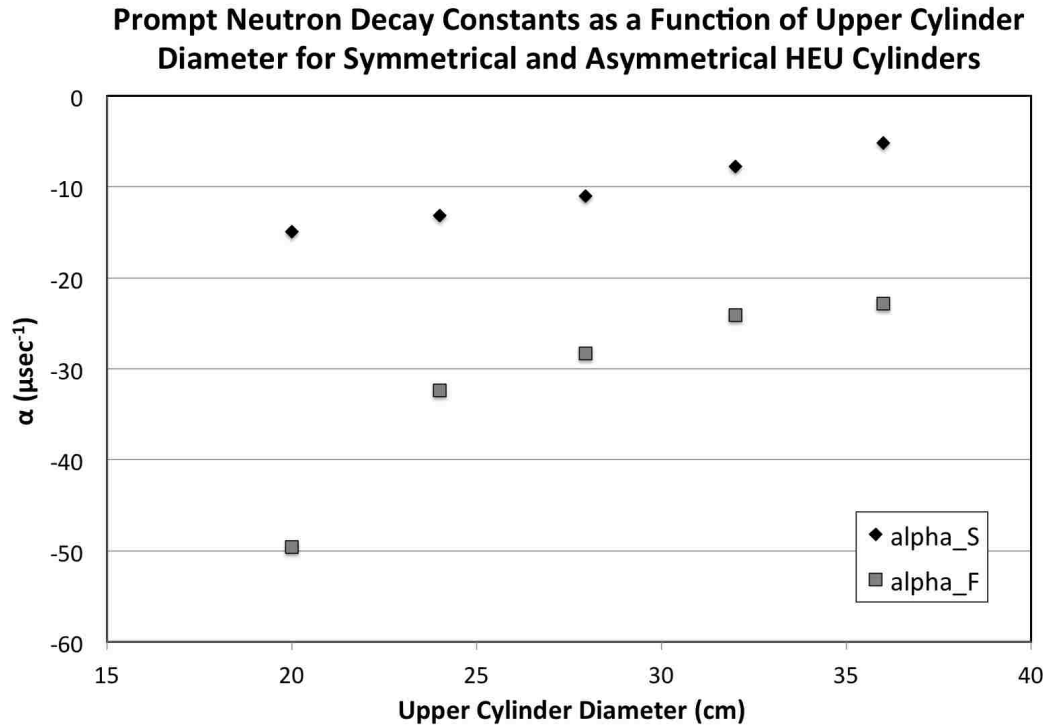
Figure 4.11: Comparison of the prompt neutron decay constants for the asymmetrical HEU cylinders with the diameter of the upper cylinder modified.

Upper Cylinder Thickness (cm)	k_{eff}	α_S (μsec^{-1})	α_F (μsec^{-1})
8.0	0.96759	-5.991 ± 0.005	-21.26 ± 0.04
7.314 (symm)	0.93319	-10.64 ± 0.05	-25.5 ± 0.3
7.0	0.92724	-11.82 ± 0.02	-28.3 ± 0.1
6.314	0.92070	-13.59 ± 0.01	-34.5 ± 0.2
5.314	0.91803	-14.52 ± 0.01	-42.0 ± 0.3

Table 4.9: Prompt neutron decay constants for the asymmetrical configurations with the thickness of the upper cylinder modified.
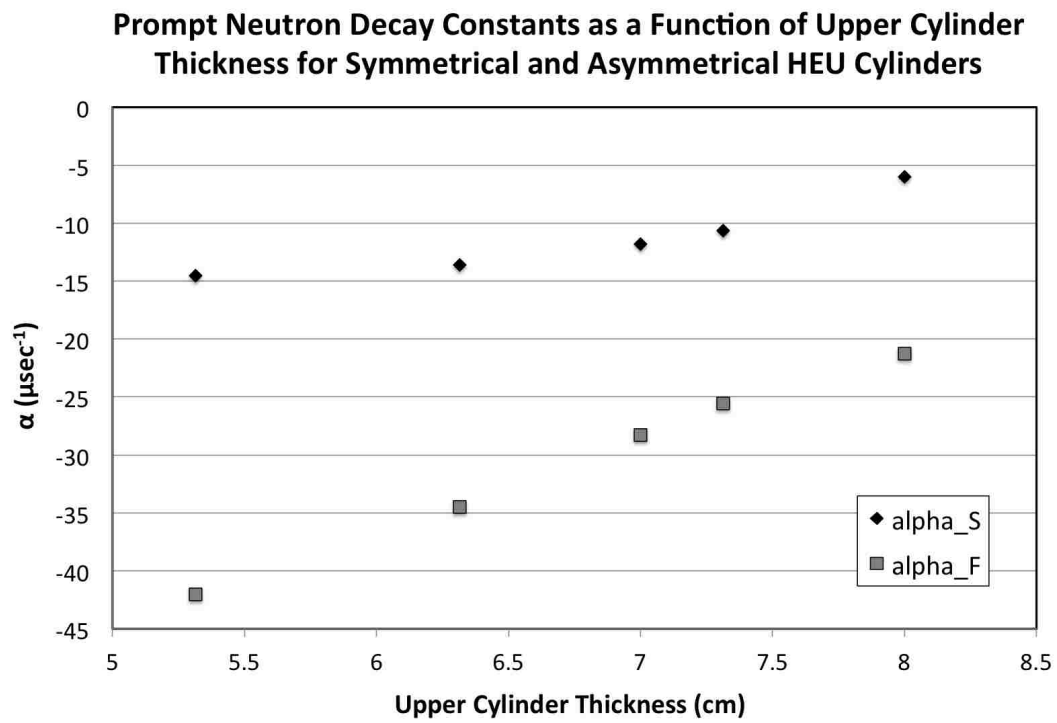
Figure 4.12: Comparison of the prompt neutron decay constants for the asymmetrical HEU cylinders with the thickness of the upper cylinder modified.

α_F (μsec^{-1})			
Cylinder Thickness (cm)	Calculated	NLSQ	% Difference
7.314	-23.29 ± 0.07	-25.54 ± 0.26	9.66
6.676	-34.90 ± 0.06	-38.43 ± 0.18	10.11
6.042	-51.94 ± 0.20	-48.87 ± 0.38	5.91

Table 4.10: Comparison of the faster prompt neutron decay constant found using the calculational method and the nonlinear least squares fit method to the measured values for the symmetrical HEU cylinders cases.

4.4.5 Alternative Determination of the Faster Prompt Neutron Decay Constant

The results reveal the difficulty in finding the faster prompt neutron decay constant via the NLSQ method. Since the slower prompt neutron decay constant can be found much easier with much less fluctuation between time bin width choices, it can be used in Equation 2.35 along with the isolated core decay constants to calculate α_F. Tables 4.10 through 4.12 compare the faster decay constant found via Equation 2.36 to that found using the NLSQ method and to the measured values. It should be noted, however, that Equation 2.35 does not account for the transit time between regions and therefore the calculated α_F may not be representative of the true faster decay constant if transit time is significant.

4.4.6 Effect of Separation Distance on the Multipoint Kinetics Parameters

Previously it was mentioned that as a two-region system becomes more tightly coupled, it approaches the single-point kinetics regime. Figs. 4.13 and 4.14 show that as the separation distance decreases, and thus the system becomes more tightly coupled, the slower prompt neutron decay constant becomes even slower and the faster prompt neutron decay constant increases in magnitude. At small separation distances, the slower decay constant determined from multipoint kinetics and the decay constant found by applying single-point kinetics are essentially the same.

α_F (μsec^{-1})			
Upper Cylinder Diameter (cm)	Calculated	NLSQ	% Difference
36.0	-20.33	-22.84	12.35
32.0	-21.43	-24.08	12.37
24.0	-28.11	-32.38	15.19
20.0	-36.66	-49.61	35.32

Table 4.11: Comparison of the faster prompt neutron decay constant found using the calculational method to the nonlinear least squares fit method for the asymmetrical case with the upper cylinder diameter modified.

α_F (μsec^{-1})			
Upper Cylinder Thickness (cm)	Calculated	NLSQ	% Difference
8.0	-19.31	-21.26	10.10
7.0	-26.00	-28.27	8.73
6.314	-35.43	-34.49	2.65
5.314	-58.70	-42.01	28.43

Table 4.12: Comparison of the faster prompt neutron decay constant found using the calculational method to the nonlinear least squares fit method for the asymmetrical case with the upper cylinder diameter modified.
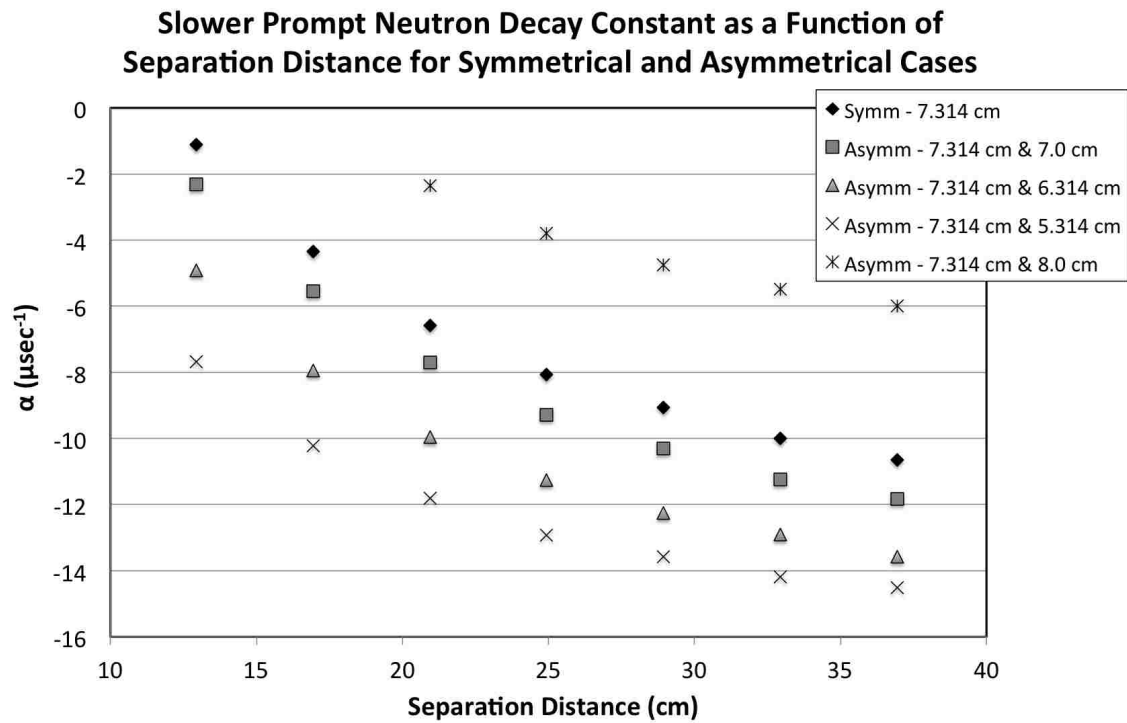
Figure 4.13: Comparison of the slower prompt neutron decay constants for the symmetrical and asymmetrical (modified thickness) HEU cylinders at various separation distances.
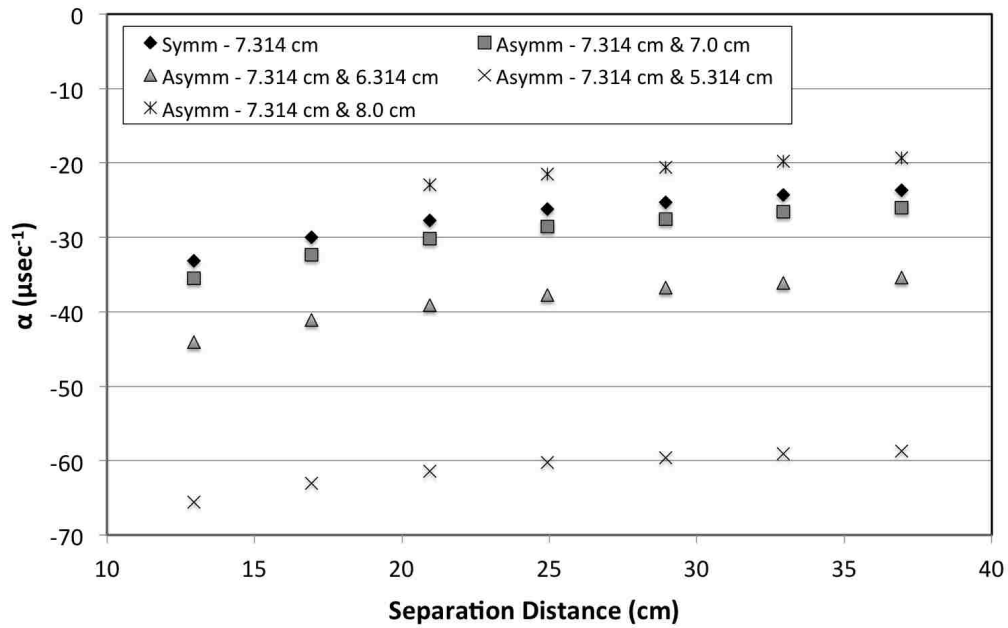
Figure 4.14: Comparison of the faster prompt neutron decay constants for the symmetrical and asymmetrical (modified thickness) HEU cylinders at various separation distances.

Upper Cylinder Thickness (cm)	Separation Distance (cm)
8.0	205.3
7.314	76.3
7.0	62.6
6.314	54.0
5.314	51.2

Table 4.13: Estimated separation distance at which the two-region system experiences complete decoupling for the symmetrical and asymmetrical HEU cylinders cases.

On the other hand, as the system becomes more loosely coupled to the point that coupling disappears altogether, the system can no longer be described by multipoint kinetics. At that point, each region falls under the single-point kinetics domain and must be analyzed individually. For a symmetrical system, the slower and faster prompt neutron decay constants will both converge on the isolated region decay constant; for an asymmetrical system, the slower decay constant will approach that of the system with the smaller negative reactivity while the faster decay constant will approach that of the system with the larger negative reactivity. Instead of being linear, the rate at which the coupled system decay constants converge on the individual decay constants decreases exponentially as the separation distance increases.

An estimate of the separation distance at which complete decoupling occurs can be obtained from the separation distance plots. The isolated region decay constant is set as the y-intercept value of the equation determined from a logarithmic fit to the data points. Solving for x, the separation distance at which complete decoupling is expected to occur is found. Table 4.13 shows the estimated decoupling distances for the symmetrical and asymmetrical cases of the HEU cylinders.

4.4.7 Determination of the Coupling Coefficients for Asymmetrical Systems from Measured Data

The coupling coefficients for the asymmetrical system are determined using the following process. First, the regional prompt neutron decay constants, α_1 and α_2, are found from separate `ptrac` simulations using single-point kinetics analysis. The coupled case is then run and the faster and

γ_{jk} (μsec^{-1})		
Upper Cylinder Diameter (cm)	γ_{12}	γ_{21}
36.0	7.9412 ± 0.0005	4.7872 ± 0.0004
32.0	7.2606 ± 0.0006	5.5309 ± 0.0004
27.94 (symm)	6.137 ± 0.002	6.137 ± 0.002
24.0	5.6784 ± 0.0006	7.7652 ± 0.0008
20.0	4.6604 ± 0.0006	9.3022 ± 0.0009

Table 4.14: Coupling time constants determined from the slower prompt neutron decay constant for the asymmetrical cases for various upper cylinder diameters.

slower prompt neutron decay constants are determined from the NLSQ fit of the multipoint kinetics Rossi-alpha curve. A `kcode` calculation is then run with an F4 tally to determine the total neutron population in each region and an F1 tally to count the number of particles entering each region. The ratio of particles entering a region to the total neutron population in the other region is determined. The fraction of this ratio to the sum of both ratios (for two regions) determines the fraction of the total coupling neutrons that reach the region of interest. The product of the coupling coefficients, determined from Equation 2.33 using the regional and slower decay constants found from the `ptrac` simulations, is multiplied by these fractions to determine the individual coupling time constant for each region. Tables 4.14 and 4.15 show the coupling time constants determined using this method for the asymmetrical HEU cylinders configurations. Figure 4.15 shows the coupling time constants for the modified upper cylinder diameter cases; it is easily seen in this plot that as the asymmetry increases, the difference between the coupling time constants incsreases.

Similar to the faster and slower decay constants, the coupling coefficients exhibit an exponentially decreasing trend as the separation distance increases. These trends are visually represented in the individual coupling constants plotted in Figure 4.16 and in the product of the coupling constants shown in Figure 4.17. For the 8.0 cm configuration, both coupling time constants are smaller than the coupling coefficient for the symmetrical case. For the more subcritical cases, the coupling constants become larger. For the more asymmetrical cases, the separation between the coupling constants increases as expected.

**Coupling Time Constants as a Function of Upper Cylinder Diameter for Symmetrical and Asymmetrical HEU Cylinders**
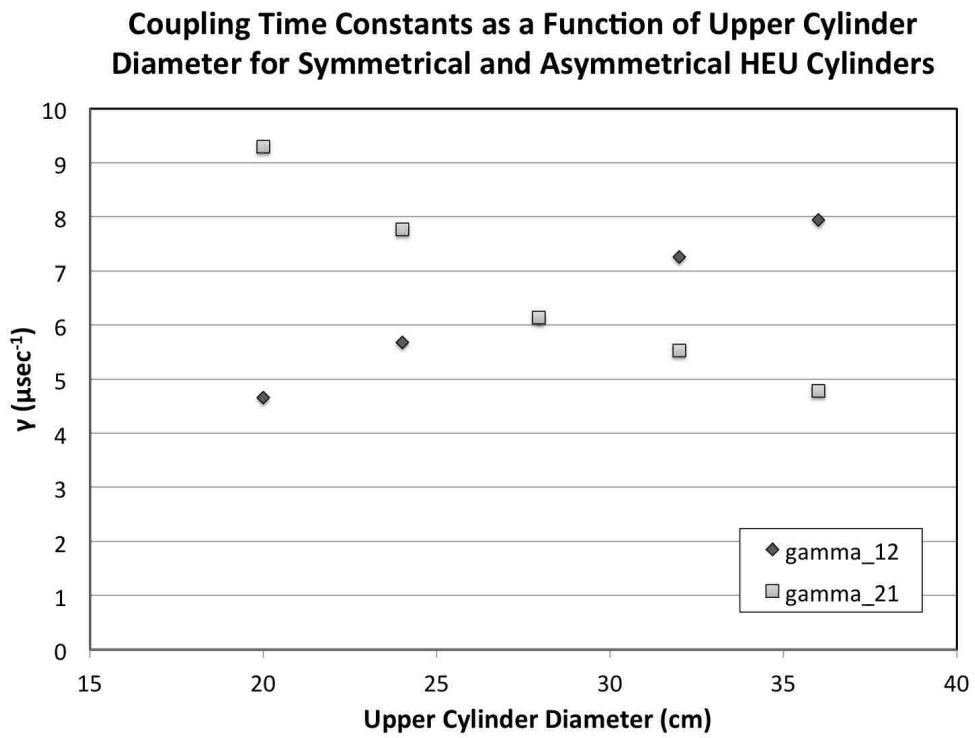
Figure 4.15: Comparison of the coupling time constants for the asymmetrical HEU cylinders with the diameter of the upper cylinder modified.

γ_{jk} (μsec^{-1})		
Separation Distance (cm)	γ_{12}	γ_{21}
8.0 cm		
20.94	8.8880 ± 0.0007	9.6449 ± 0.0007
24.94	7.3345 ± 0.0008	7.9616 ± 0.0009
28.94	6.2318 ± 0.0009	6.780 ± 0.001
32.94	5.348 ± 0.001	5.811 ± 0.001
36.94	4.713 ± 0.002	5.122 ± 0.002
7.0 cm		
12.94	16.1244 ± 0.0007	16.8960 ± 0.0007
16.94	12.9331 ± 0.0009	13.6009 ± 0.0009
20.94	10.796 ± 0.001	11.354 ± 0.001
24.94	9.220 ± 0.001	9.705 ± 0.002
28.94	8.224 ± 0.002	8.641 ± 0.002
32.94	7.279 ± 0.002	7.659 ± 0.002
36.94	6.697 ± 0.002	7.039 ± 0.003
6.314 cm		
12.94	17.6153 ± 0.0009	17.6898 ± 0.0009
16.94	13.175 ± 0.001	13.223 ± 0.001
20.94	10.197 ± 0.002	10.231 ± 0.002
24.94	8.260 ± 0.002	8.272 ± 0.002
28.94	7.016 ± 0.002	7.019 ± 0.002
32.94	5.935 ± 0.003	5.936 ± 0.003
36.94	4.926 ± 0.003	5.696 ± 0.004
5.314 cm		
12.94	18.506 ± 0.002	24.790 ± 0.002
16.94	15.444 ± 0.002	20.597 ± 0.003
20.94	13.354 ± 0.002	17.742 ± 0.003
24.94	11.721 ± 0.003	15.509 ± 0.004
28.94	10.709 ± 0.003	14.167 ± 0.004
32.94	9.706 ± 0.004	12.782 ± 0.005
36.94	9.134 ± 0.004	11.953 ± 0.005

Table 4.15: Coupling time constants determined from the slower prompt neutron decay constant for the modified upper cylinder thickness asymmetrical cases for various separation distances.

Figure 4.16: Plot of the coupling time constants for each case for the 7.314 cm symmetrical system and various asymmetrical systems.
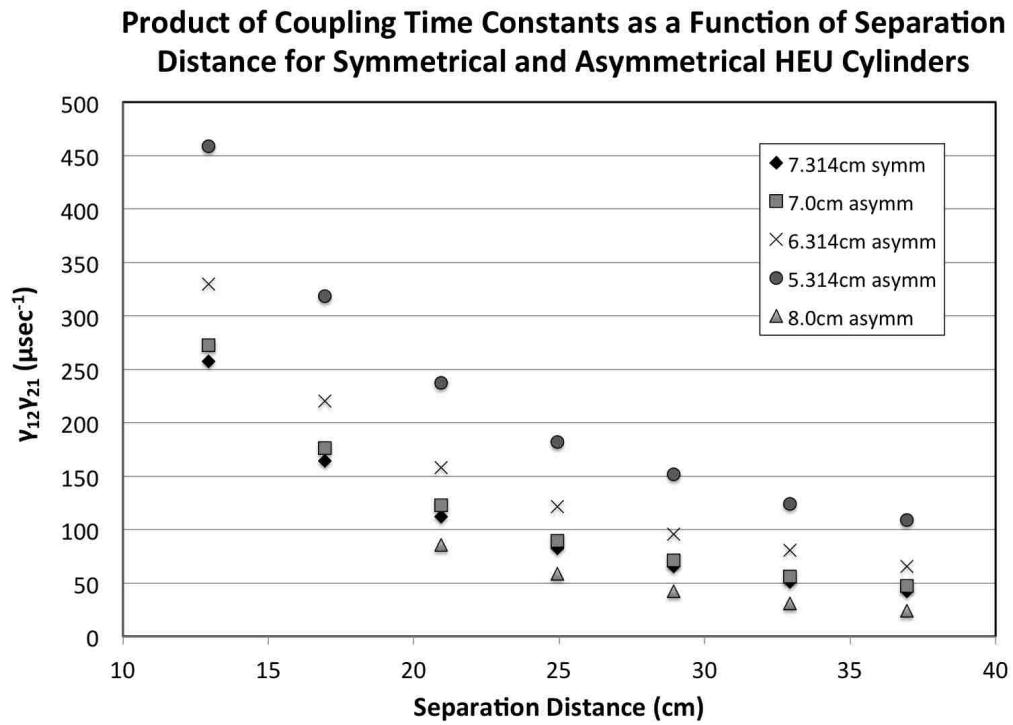
Figure 4.17: Plot of the product of the coupling time constants for each case for the 7.314 cm symmetrical system and various asymmetrical systems.
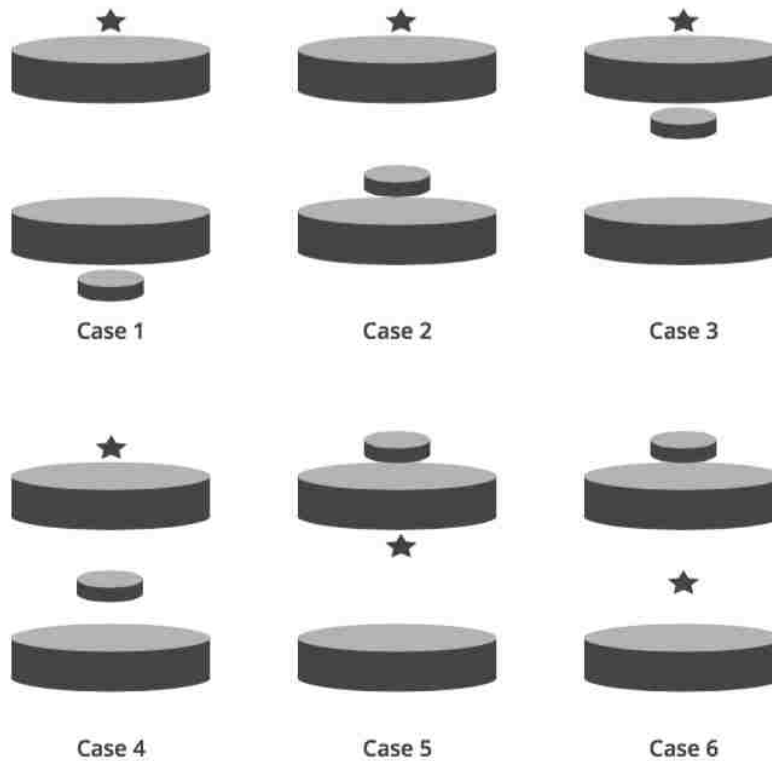
Figure 4.18: Detector and source locations for each case for the symmetrical HEU cylinders (Not to scale).

4.4.8 Effect of Detector Placement on the Measurement of the Coupled Prompt Neutron Decay Constants

Theoretically, the location of the detector should have no effect on the measurement of the prompt neutron decay constants. Measurements by Farinelli and Pacilio have shown this to be true except when the detector is located at the centerpoint between two symmetrical cores, at which point the faster decay constant is not observable [28]. It is unknown if and at what location this should also occur in an asymmetrical system. A series of simulations were run for both the symmetrical 7.314 cm thick HEU cylinders and for the 5.314 cm asymmetrical configuration analyzed in the previous section. Figures 4.18 and 4.19 show the detector placement for each case for the symmetrical and the asymmetrical systems, respectively.

Figures 4.20 and 4.21 show the expected response due to detector location. The error bars
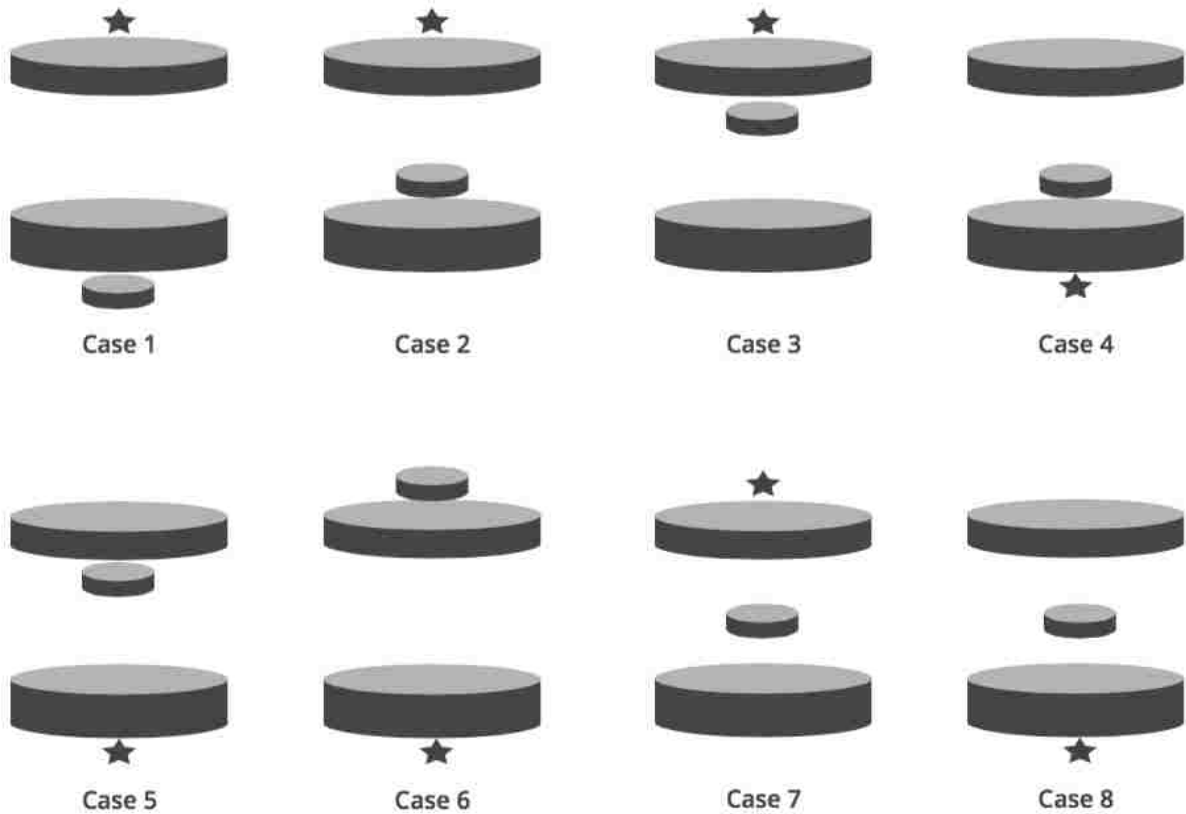
Figure 4.19: Detector location for each case for the asymmetrical HEU cylinders (Not to scale).

for most of the data points are too small to be seen. The values of the "measured" prompt neu-tron decay constants are independent of detector location except for when the detector is placed equidistant between the regions for both the symmetrical and asymmetrical configurations. When the detector is located in the center of the system, the slower decay constant is still observed; how-ever, the faster decay constant cannot be seen. The faster prompt neutron decay constant for the symmetrical case and for Case 8 for the asymmetrical system is approximately zero within error. Case 7 for the asymmetrical system includes large errors for most of the time bin widths, which leads the author to believe that the value with the minimum error is spurious. This shows that a small error does not necessarily guarantee a correct value and that the researcher must be cognizant of their measurement technique to ensure that the results are realistic.
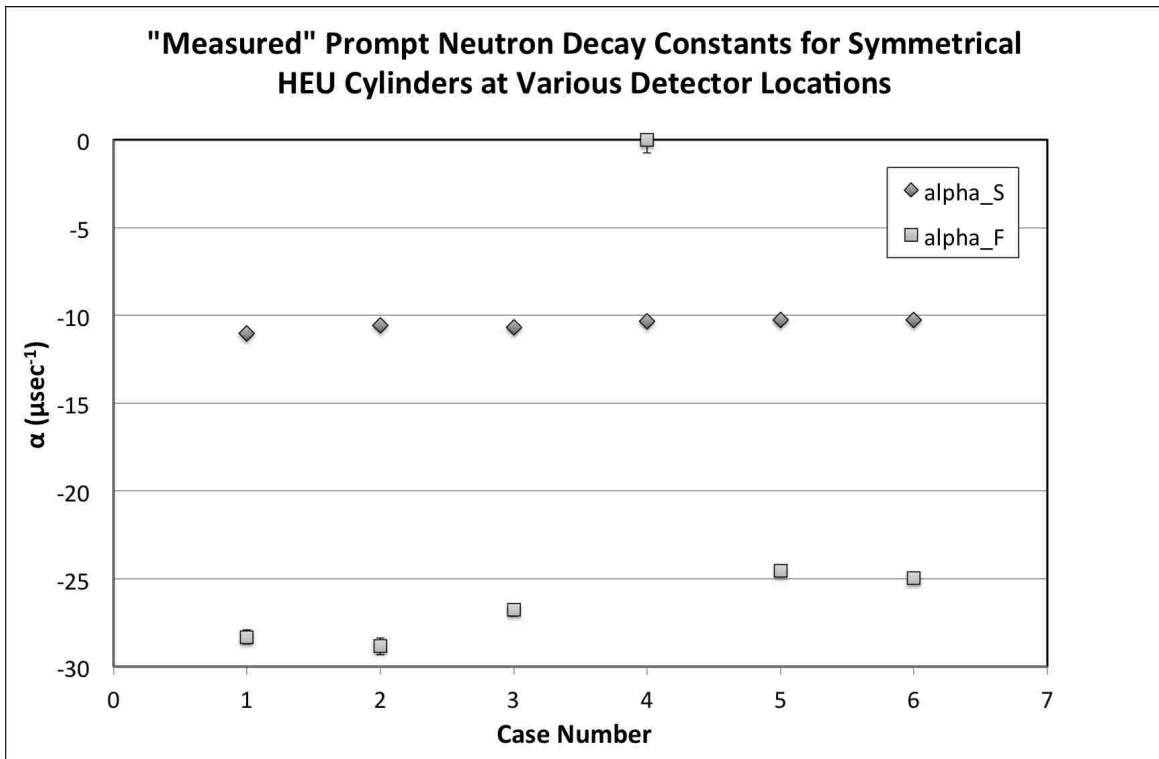
Figure 4.20: Plot of the prompt neutron decay constants for each case for the symmetrical system.
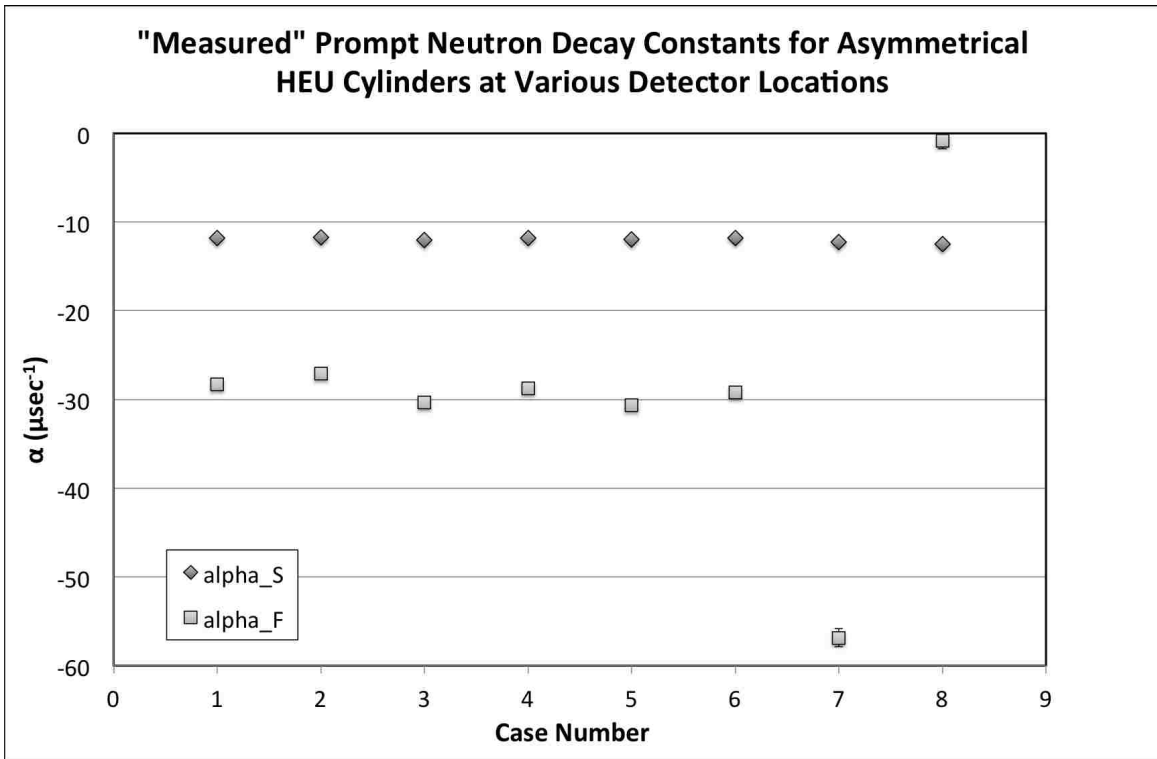
Figure 4.21: Plot of the prompt neutron decay constants for each case for the asymmetrical system (error bars are too small to be seen).

Chapter 5

Preliminary Subcritical Coupled-Core Simulations in Support of the Final Measurement Design

The feasibility of an asymmetrical, fast, bare metal coupled-core experiment for verification of the computational process described in the previous chapter is examined here. Preliminary simulations for a simplified version of two asymmetrical configurations of the Rocky Flats Shells experiment are conducted. A symmetrical system will also be measured as a base case. The goal is to observe both prompt neutron decay constants and infer the coupling coefficients for each configuration. The measurements are planned to be performed either late 2017 or early 2018.

5.1   Description of the Coupled Core System

Los Alamos National Laboratory has some very unique facilities and capabilities that most other laboratories and research centers do not have, not the least being the experimental critical assemblies housed at the National Criticality Experiments Research Center (NCERC) in Nevada. These assemblies are used for various experiments such as subcritical and approach-to-critical measurements. Among the available assemblies are a few systems that can be used for coupled-core measurements. For this research, the Rocky Flats Shells mounted on the Planet vertical lift assembly were chosen for the ease in modifying the geometry and mass of the multiplying material and in separating the two cores.

Figure 5.1: Rocky Flats Shells [3].

5.1.1 The Rocky Flats HEU Shells

The Rocky Flats Shells are a set of nesting hemispherical HEU metal shells that were manufactured for critical experiments at the Rocky Flats facility in Colorado in the 1960s [2]. There are 80 shells in total, numbered sequentially from the smallest to largest diameters: the odd-numbered shells stack to form one half of a sphere and the even-numbered shells stack to form the other half. A subset of the shells is shown in Figure 5.1.

The Rocky Flats Shells 33 through 64 stacked in a symmetrical configuration will be measured as a base case. Two asymmetrical configurations, one with Shell 64 removed and the other with Shells 62 and 64 removed, will be measured for verification of the computational methods outlined in the previous chapter. The inner and outer diameters and the masses corresponding to the shell numbers are listed in Table 5.1. The total mass for all 32 shells is 116,446 g. The isotopic composition of the Rocky Flats Shells from measurements performed in 1971 is shown in Table 5.2. The average density of the HEU is 18.65 g/cm^3 [2].

The shells will be unmoderated and unreflected such that the neutron spectrum will remain relatively hard; i.e., the neutrons will be within the fast energy regime. Compared to a total mass of 22.1 to 53.6 kg for the HEU cylinders studied in Chapter 4, the Rocky Flats Shells contain more mass at around 116 kg for the symmetrical case. However, since the convex surface of each region faces away from the other region, high neutron leakage is expected that will not contribute to the coupling. The concave inner surface will also lead to higher non-contributing leakage and

Shell Number	Inner Diameter (mm)	Outer Diameter (mm)	Mass (g)
33	70.060	73.296	1949
34	70.098	73.338	1951
35	73.417	76.658	2134
36	73.428	76.665	2130
37	76.824	80.027	2349
38	76.711	80.027	2342
39	80.128	83.364	2527
40	80.075	83.292	2511
41	83.462	86.683	2722
42	83.443	86.680	2741
43	86.782	89.996	2945
44	86.764	89.995	2953
45	90.095	93.328	3188
46	90.104	93.329	3179
47	93.418	96.667	3442
48	93.432	96.683	3450
49	96.771	99.999	3656
50	96.775	100.001	3658
51	100.119	103.340	3912
52	100.104	103.336	3918
53	103.445	106.696	4207
54	103.427	106.685	4208
55	106.743	110.009	4464
56	106.773	110.013	4461
57	110.113	113.348	4733
58	110.112	113.315	4729
59	113.439	116.660	5003
60	113.444	116.670	5025
61	116.765	119.987	5323
62	116.785	120.015	5326
63	120.108	123.358	5660
64	120.111	123.363	5650

Table 5.1: Inner and outer diameters and masses of the Rocky Flats Shells 33-64 [2].

Isotope	wt%
U-234	1.02
U-235	93.16
U-236	0.47
U-238	5.35

Table 5.2: Isotopic composition of Rocky Flats Shells [2].

also to neutrons that exit and re-enter the same region. The complexity in the system geometry leads to complexity in the analysis of the coupling coefficients for the asymmetrical cases. The high leakage also results in far more subcritical individual regions, indicating a faster response and larger coupling coefficients than that observed for the HEU cylinders. The deep subcriticality of the individual regions will test both the computational method and the detection system.

Removing either an innermost or outermost shell not only changes the amount of fissile mass, it also changes the geometry of the system, resulting in two factors that contribute to the system asymmetry. The symmetrical configuration is critical when the two halves are brought together. Removal, rather than addition, of shells means that the system will become more subcritical when combined in the asymmetric configurations.

5.1.2   The Planet Vertical Lift Assembly

The Rocky Flats Shells will be placed on the Planet light-duty, screw-type vertical lift assembly which has a lower support that moves vertically in relation to a fixed upper support. The upper support plate is a 2.54 cm thick, 114.3 cm by 114.3 cm 6061-T6 aluminum plate with a 44.2 cm by 44.2 cm center cut-out. The lower support is a 78.7 cm by 78.7 cm, 2.54 cm-thick 6061-T6 aluminum plate. The separation distance between the two cores is controlled via the lower support [4]. Fig. 5.2 shows Planet in operation during a non-related measurement.

Figure 5.2: The Planet vertical lift assembly (shown here with the Class Foils experiment) [4].

5.2 Detection System

For these simulated measurements, the Rossi-alpha of the neutron signature will be measured. Rossi-alpha analysis relies only on count rates; determination of the neutron energy spectrum or any other information is not necessary. Therefore, an ideal detection system is one that produces neutron counts based on termination events within the detector volume and is insensitive to gamma rays. High-density polyethylene-moderated Helium-3 (^{3}He) detectors are one of the most efficient neutron-termination-event-type detectors for counting fast neutron systems, but because the neutrons scatter and slow down in the polyethylene at different rates, the absolute time after leaking from the core is not preserved. An unmoderated detector system must be used for these measurements to preserve the fission emission time distribution.

5.2.1 Helium-3 Detectors and List-Mode Acquisition

The experiments were modeled with a set of unmoderated ^{3}He proportional counters. ^{3}He is an isotope of Helium containing two protons and one neutron within its nucleus. The neutron shortage

makes ^{3}He very susceptible to neutron absorption, making it an ideal gas for neutron detection. ^{3}He detectors produce counts via the ^{3}He[n,p]^{3}H reaction in which a neutron is absorbed by a ^{3}He nucleus and a proton and a ^{3}H ion are produced. The proton and the negatively-charged ^{3}H ion subsequently ionize the surrounding gas, creating ion pairs consisting of electrons and positively-charged ions. The electrons migrate to the anode, causing an electrical pulse, while the positive ions are drawn toward the cathode. Each pulse created by a neutron absorption event is recorded as a single count [64].

Without moderation, ^{3}He detectors are very inefficient for fast neutron counting and thus large measurement times are needed to obtain enough counts to provide acceptable statistics. This inefficiency is partially explained by Figure 5.3, which shows the microscopic neutron absorption cross-section for ^{3}He compared to other reaction cross-sections as a function of incident neutron energy. As the neutron energy increases, the absorption cross-section decreases: ^{3}He is only 0.5% as effective in absorbing a neutron at 1.0 MeV than a neutron at 0.025 eV (the energy of a thermalized neutron). As the incident neutron energy increases, the elastic scattering reaction starts to compete with absorption, eventually overtaking it as the dominant reaction for neutron energies above 0.1 MeV. Secondly, the low density of gaseous detectors means that a neutron encountering a nuclei target is a rather rare event, so many neutrons can easily pass through the detector volume without being detected.

Six GE Reuter-Stokes ^{3}He tubes of the type shown in Figure 5.4 are available for list-mode measurements. Each tube is less than 12.7 cm long with a detection volume 9.53 cm in length and 0.64 cm in diameter. The detection volume contains ^{3}He gas pressurized to 40 atmospheres. The active length is 7.62 cm.

The list-mode data acquisition system used by Los Alamos for coincidence counting is a custom-built module containing a preamplifier, amplifier, high voltage source and 32 channels. Each ^{3}He counter is connected to a single channel. The bin size is 100 nsec and the maximum count rate that can be measured is 300,000 counts per second (cps). Binary list-mode data is output from the module, which can then be processed using a variety of analysis methods [54]. The
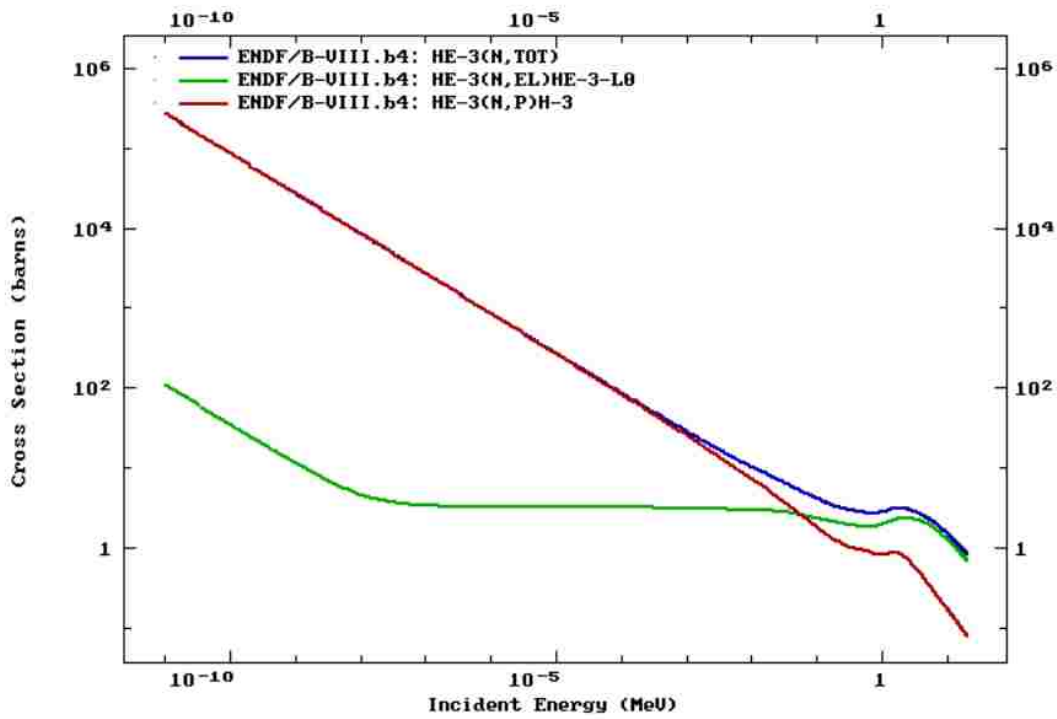
Figure 5.3: Microscopic absorption, elastic scattering, and total cross-sections for ^{3}He as a function of incident neutron energy [5].

Figure 5.4: Helium-3 proportional counter [6].
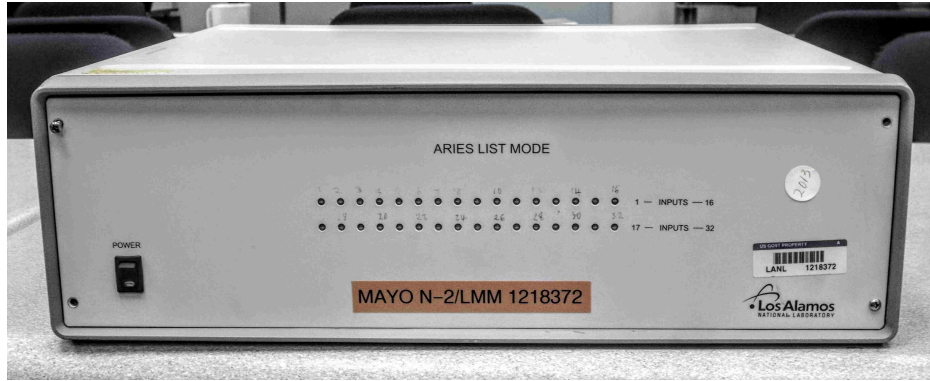
Figure 5.5: LANL list-mode module.

list-mode module is shown in Fig. 5.5.

5.3 `MCNP 6` Modeling

Three shell configurations were modeled using `MCNP 6`: one symmetrical configuration with shells 33-64 and two asymmetrical configurations, one with shells 33-63 and the other with shells 33-61 and 63. The two hemispheres were modeled with the curved surfaces facing away from each other such that when they are brought together, they create a hollow, spherical core as shown in Figure 5.6. Each configuration was modeled at various separation distances to observe the change in coupling. The count times were 500 seconds for all configurations.

The preliminary simulations contained only the Rocky Flats Shells, a point source, and an artificial detector. This provided a starting point for the design of the experiment. Both the source and the detector are identical to the source and detector modeled in the HEU cylinders simulations. Each configuration was modeled at 0.0 (closed), 1.0, 2.5, 5.0, 7.5, 10.0, 15.0 and 20.0 cm of separation measured from the flat surface of the lower hemisphere to the flat surface of the upper hemisphere. Two examples of the `MCNP 6` input file for the asymmetrical Rocky Flats Shells 33 through 63 configuration at a 5.0 cm separation distance, one for the `ptrac` calculation and one for the `kcode` calculation with tallies, are provided in Appendix D.
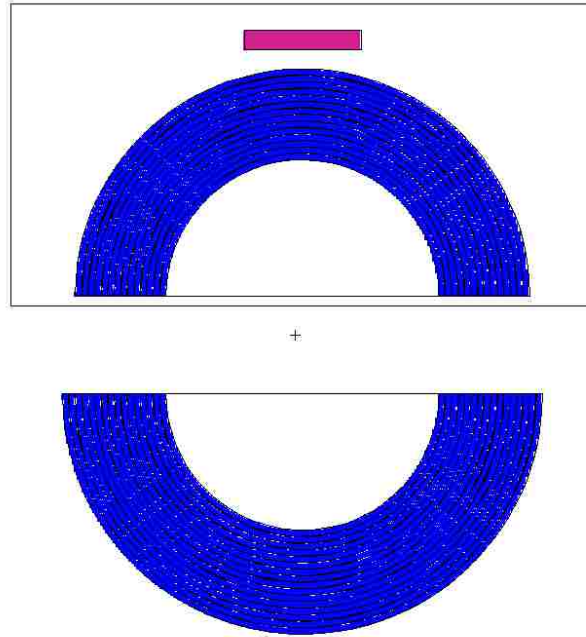
Figure 5.6: `MCNP6` model for the preliminary simulations of the Rocky Flats shells.

5.3.1 Results of the Preliminary Simulations for Incremental Separation Distances

The prompt neutron decay constants for the preliminary simulations are shown in Tables 5.3 through 5.5 and Figure 5.7. As with the HEU cylinders test, the models suggest that the slower prompt neutron decay constant for the coupled Rocky Flats Shells is easily observed. However, the faster prompt neutron decay constant is much more difficult to determine than for the HEU cylinders due to the deep subcriticality of the individual regions. Longer count times were run to try to narrow down the results with little success. The calculational method for determining the faster decay constant was therefore utilized.

As with the HEU cylinders, the Rocky Flats Shells decay constants appear to converge towards the isolated region decay constants as the separation distance increases. The estimated distances at which the systems exhibit complete decoupling are listed in Table 5.6.

Tables 5.7 through 5.9 and Figure 5.8 show the coupling time constants at various separation

Separation Distance (cm)	k_{eff}	α_S (μsec^{-1})	α_F (μsec^{-1})
2.5	0.94955	-6.387 ± 0.003	-68.90 ± 0.09
5.0	0.91146	-10.817 ± 0.007	-64.47 ± 0.09
7.5	0.88246	-14.57 ± 0.02	-60.72 ± 0.09
10.0	0.86519	-16.81 ± 0.03	-58.5 ± 0.1
15.0	0.83895	-21.06 ± 0.06	-54.2 ± 0.1
20.0	0.82482	-21.70 ± 0.09	-53.6 ± 0.1

Table 5.3: Results from the preliminary simulations for the prompt neutron decay constants for the symmetrical Rocky Flats Shells 33-64 configuration. $\alpha_{iso} = -37.64 \mu sec^{-1}$.

Separation Distance (cm)	k_{eff}	α_S (μsec^{-1})	α_F (μsec^{-1})
2.5	0.93065	-8.479 ± 0.005	-75.53 ± 0.04
5.0	0.89186	-13.06 ± 0.01	-70.95 ± 0.04
7.5	0.86548	-16.77 ± 0.03	-67.23 ± 0.04
10.0	0.84717	-18.92 ± 0.05	-65.09 ± 0.04
15.0	0.82390	-22.61 ± 0.07	-61.40 ± 0.04
20.0	0.81164	-24.2 ± 0.1	-59.82 ± 0.04

Table 5.4: Results from the preliminary simulations for the prompt neutron decay constants for the asymmetrical Rocky Flats Shells 33-63 configuration. $\alpha_1 = -37.64 \mu sec^{-1}$; $\alpha_2 = -46.37 \mu sec^{-1}$.

Separation Distance (cm)	k_{eff}	α_S (μsec^{-1})	α_F (μsec^{-1})
2.5	0.91302	-10.77 ± 0.01	-81.05 ± 0.05
5.0	0.87577	-15.16 ± 0.02	-76.66 ± 0.05
7.5	0.85117	-18.12 ± 0.03	-73.69 ± 0.05
10.0	0.83429	-20.39 ± 0.04	-71.43 ± 0.05
15.0	0.81426	-23.76 ± 0.08	-68.06 ± 0.05
20.0	0.80394	-26.9 ± 0.1	-64.94 ± 0.05

Table 5.5: Results from the preliminary simulations for the prompt neutron decay constants for the asymmetrical Rocky Flats Shells 33-61+63 configuration. $\alpha_1 = -37.64 \mu sec^{-1}$; $\alpha_2 = -54.17 \mu sec^{-1}$.
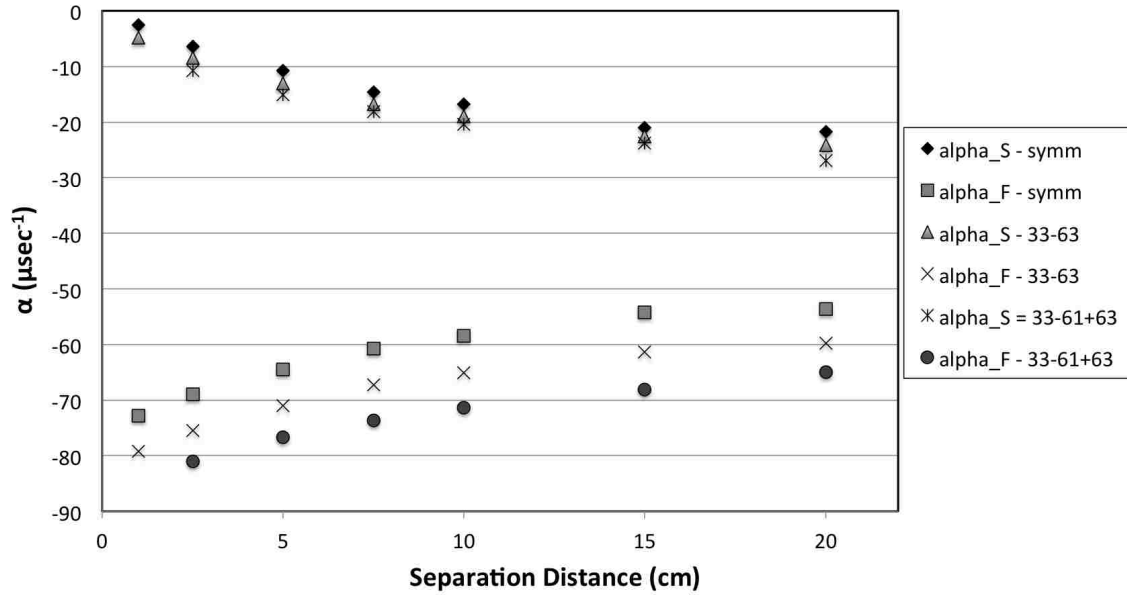
Figure 5.7: Plot of the results from the preliminary simulations for the prompt neutron decay constants for each case for the Rocky Flats Shells at various separation distances.

Configuration	Separation Distance (cm)
33-64	209.2
33-63	156.5
33-61+63	89.9

Table 5.6: Estimated separation distance at which the system exhibits complete decoupling.

Separation Distance (cm)	γ (μsec^{-1})
2.5	31.26 ± 0.05
5.0	26.83 ± 0.05
7.5	23.08 ± 0.05
10.0	20.83 ± 0.06
15.0	16.58 ± 0.08
20.0	16.0 ± 0.1

Table 5.7: Coupling time constants for the symmetrical Rocky Flats Shells 33-64 configuration.

Separation Distance (cm)	γ_{12} (μsec^{-1})	γ_{21} (μsec^{-1})
2.5	31.248 ± 0.002	35.361 ± 0.003
5.0	26.540 ± 0.002	30.861 ± 0.003
7.5	22.608 ± 0.003	27.314 ± 0.004
10.0	20.103 ± 0.003	25.573 ± 0.005
15.0	15.572 ± 0.003	22.934 ± 0.007
20.0	12.889 ± 0.004	23.15 ± 0.01

Table 5.8: Coupling time constants for the asymmetrical Rocky Flats Shells 33-63 configuration.

distances for the symmetrical and asymmetrical cases. The coupling constants for the symmetrical system lie between those for the asymmetrical systems as expected. The coupling constants for the more subcritical region (γ_{21}) are larger than those for the less subcritical region (γ_{12}) as was seen with the HEU cylinders. Interestingly, the coupling constants for the more subcritical region appear to reach an asymptotic value of around -30 μs^{-1} as the separation distance increases for the 33-61+63 configuration. It is believed that this represents the beginning of the transition between loose coupling and complete decoupling.

5.3.2   Limitations of the List-Mode Data Acquisition System

The time resolution of the LANL list-mode acquisition system may not be fast enough for the Rossi-alpha measurements of the coupled Rocky Flats Shells. The slower prompt neutron decay

Separation Distance (cm)	γ_{12} (μsec^{-1})	γ_{21} (μsec^{-1})
2.5	30.087 ± 0.002	38.762 ± 0.003
5.0	25.345 ± 0.002	34.612 ± 0.004
7.5	21.801 ± 0.002	32.279 ± 0.005
10.0	18.827 ± 0.003	30.959 ± 0.007
15.0	13.922 ± 0.004	30.32 ± 0.02
20.0	9.713 ± 0.002	30.24 ± 0.04

Table 5.9: Coupling time constants for the asymmetrical Rocky Flats Shells 33-61+63 configuration.
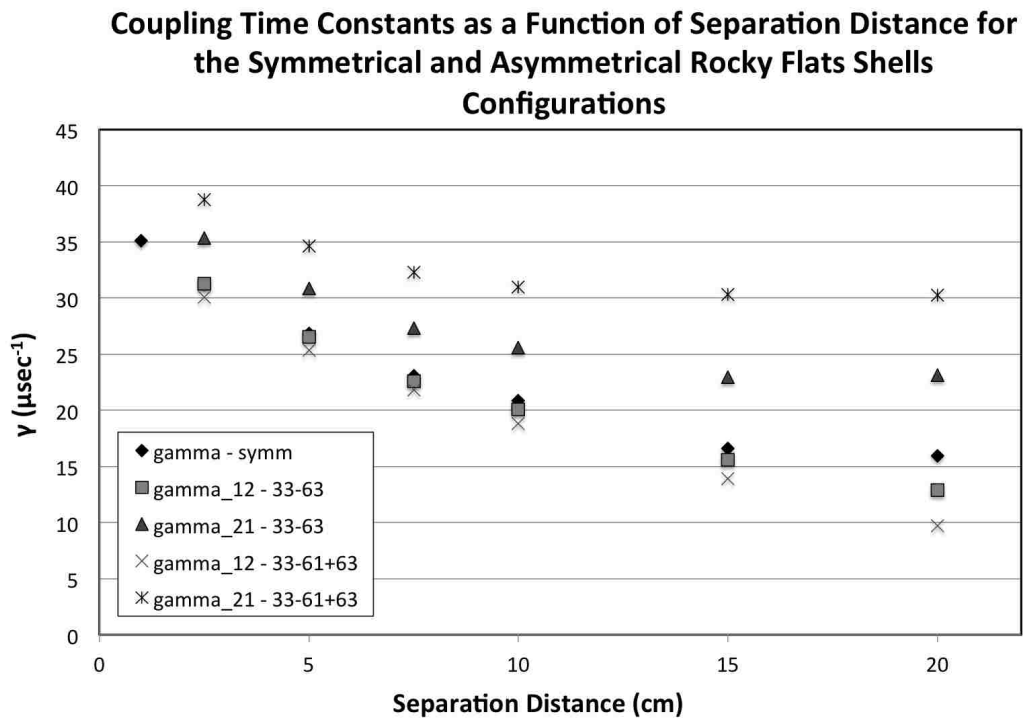
Figure 5.8: Plot of the coupling time constants for each case for the Rocky Flats Shells at various separation distances.

Prompt Neutron Decay Constants (μsec^{-1})				
Separation Distance (cm)	α_S (optimal time bin width)	α_S ($\Delta t = 0.1\mu$sec)	α_F (optimal time bin width)	α_F ($\Delta t = 0.1\mu$sec)
33-64 Symmetrical Configuration				
2.5	-6.387	-6.263	-80.648	-41.528
5.0	-10.817	-10.675	-61.764	-47.112
7.5	-14.567	-13.377	-85.215	-38.473
10.0	-16.814	-15.438	-78.356	-43.142
15.0	-21.062	-26.678	-83.011	~ 0
20.0	-21.697	-29.647	-66.012	~ 0
33-63 Asymmetrical Configuration				
2.5	-8.479	-8.318	-79.602	-42.464
5.0	-13.055	-12.410	-86.756	-41.007
7.5	-16.775	-14.925	-98.099	-39.638
10.0	-18.915	-15.116	-89.298	-35.262
15.0	-22.610	-29.411	-88.341	~ 0
20.0	-24.188	-32.501	-81.744	~ 0
33-61+63 Asymmetrical Configuration				
2.5	-10.773	-10.109	-116.544	-38.026
5.0	-15.159	-13.892	-106.618	-39.667
7.5	-18.124	-16.127	-97.775	-40.932
10.0	-20.391	-26.729	-96.871	~ 0
15.0	-23.762	-31.600	-95.017	~ 0
20.0	-26.881	-34.985	-97.408	~ 0

Table 5.10: Prompt neutron decay constants determined from the optimal time bin width compared to those determined using the minimum bin width measurable by the LANL list-mode data acquisition system.

constant for the less subcritical configurations may be observable; however, the true faster decay constant will not be observable for any configuration. Table 5.10 lists the decay constants found at a time bin width of $0.1\,\mu$s compared to those determined using the optimum time bin width. The method utilizing the α_F determined from calculation may be used for the less subcritical systems, but the difference between the true α_S and the one determined from the $0.1\,\mu$s time bin width is too great to obtain a good estimate of α_F or the coupling time constants. Another measurement system may need to be considered for these measurements.
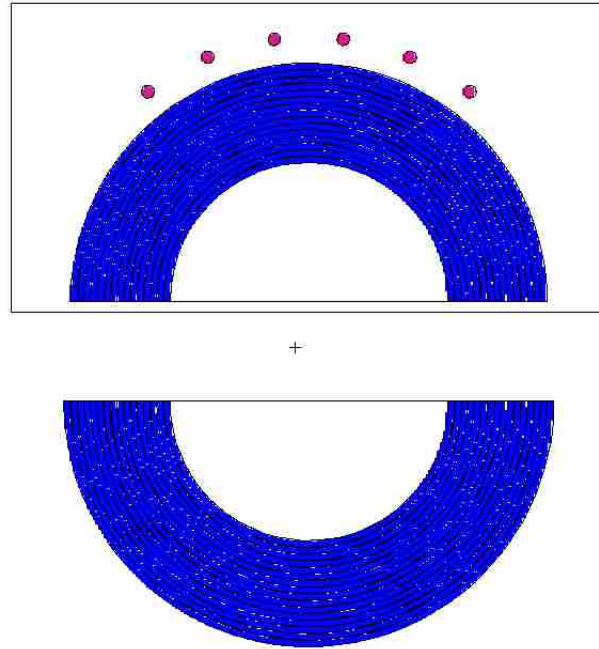
Figure 5.9: `MCNP 6` model of the Rocky Flats Shells with six ³He tubes.

5.3.3 Limitations of the Helium-3 Proportional Counters

The Rocky Flats Shells were then modeled with "real" ³He detectors to obtain an estimate of the count rate for each configuration at each separation distance. Six detectors with the properties listed for the GE Reuter-Stokes tubes were placed at 15 degree increments at 1.0 cm from the outer edge of the upper assembly as shown in Figure 5.9. The results shown in Table 5.11 reveal the low count rates expected from the small ³He tubes. The count time required to obtain 5e6 counts with six tubes would be about 2.7 hours for the 33-63 asymmetrical configuration at a separation distance of 2.5 cm. For the most asymmetrical system, 33-61+63, at the farthest separation distance, the count time would need to be around 27 hours.

Count Rates (counts/sec)			
Separation Distance (cm)	33-64 Symm Config	33-63 Asymm Config	33-61+63 Asymm Config
2.5	94.5	85.8	66.7
5.0	44.2	45.4	38.4
20.0	10.8	5.6	8.6

Table 5.11: Count rates determined from MCNP 6 for a single ^{3}He proportional counter for each Rocky Flats Shells configuration.

Chapter 6

Conclusions

6.1 Summary

This research focused on attempting to predict the dual-mode prompt neutron decay constants for a coupled asymmetrical bare metal multiplying system from simulated Rossi-alpha measurements. Following the formulation for coupled reactor systems developed by G. C. Baldwin, a general set of multipoint kinetics equations were derived with a focus on subcritical reactor systems. The analytical solutions to these equations reveal relationships between the dual-mode prompt neutron decay constants, the isolated region decay constants, and the coupling time constants that are then used to find the latter from measured values of the former.

Results from the computational analysis using `MCNP6` with the `ptrac` capability were compared to historical measurements for a symmetrical bare metal HEU system. The understanding obtained from this analysis was then applied to the preliminary modeling of a modern asymmetrical experiment utilizing the Rocky Flats Shells. A method to separate the asymmetrical coupling time constants, which cannot be individually obtained purely from Rossi-alpha measurements, was developed utilizing ratios of `MCNP6` flux and leakage calculations.

The slower prompt neutron decay constant seen in the dual-mode decay behavior of the coupled systems is easily observed in Rossi-alpha experiments for a wide range of time bin widths. However, the faster prompt neutron decay constant is difficult to observe and requires much smaller time bin widths than those regularly used in historical Rossi-alpha measurements. The deeper the

95

subcritical level of a system (or of its isolated regions), the smaller the time bin width needed to observe the correct faster decay constant. This leads to larger discrepancies in the results and also puts into question the ability of any existing measurement system to observe these parameters. For the LANL list-mode data acquisition system coupled to bare ^{3}He proportional counter tubes, the subcritical, coupled, bare metal system is too fast to measure using the method involving the determination of the faster decay constant via the curve fit.

If the mathematical relationship between the coupled-core decay constants and the isolated region decay constants is used to find the faster decay constant instead of relying on the Rossi-alpha sum-of-exponentials curve fit, then the limitations caused by the requirement of a small time bin width are eased. However, deeply subcritical systems may still be difficult or impossible to measure with the current LANL list-mode data acquisition system.

The behavior of fast bare metal systems as the separation distance is changed was studied. The systems became more loosely coupled as the separation distance increased as expected, evidenced by the decrease in magnitude of the coupling time constants. For the asymmetrical systems, the value of the slower decay constant approached that of the less subcritical region in isolation while the value of the faster decay constant approached that of the more subcritical region in isolation as the separation distance was increased. By extrapolating the trend out to the point of complete decoupling ($\alpha_S = \alpha_1$ and $\alpha_F = \alpha_2$), the separation distance at which decoupling is expected to occur was found.

A very preliminary design for future coupled-core measurements with the Rocky Flats Shells was developed. The simulations revealed the possible inability of the helium-3/list mode module measurement system to obtain enough counts in a reasonable amount of time to correctly observe the coupled decay constants in most of the planned configurations.
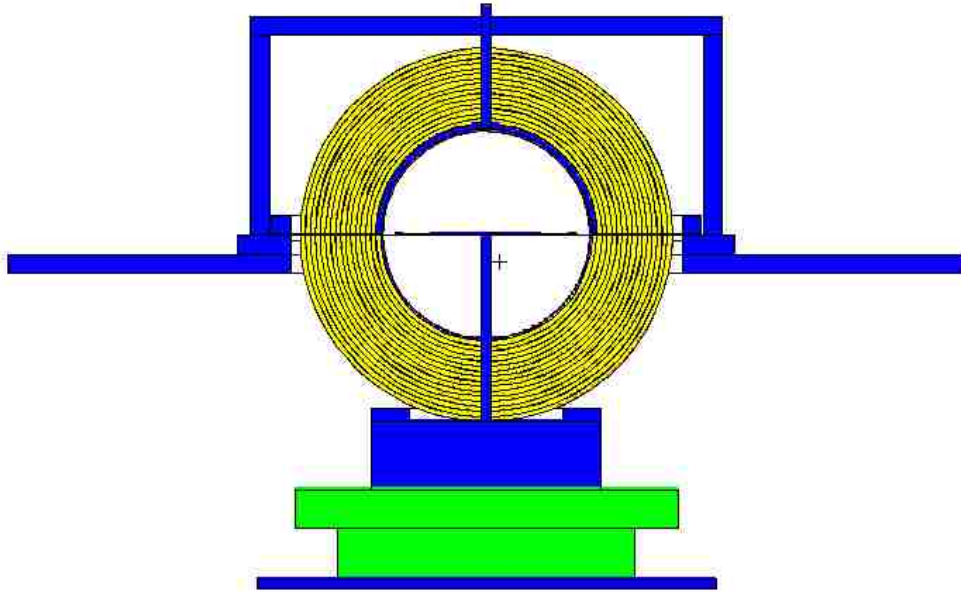
Figure 6.1: `MCNP6` model of the Rocky Flats Shells for IER-153.

6.2 Future Work

The coupled-core measurements are intended as an add-on to the integral experiment IER-153 planned for late 2017. IER-153 is designed to measure the fission spectrum of U-235 on the Rocky Flats Shells using activation foils [3]. An `MCNP6` model of the experimental configuration with support structure is shown in Figure 6.1. It was explained in [3] that room return is negligible, so the room is not included in the model. The support structure for the experiment prevents "ideal" placement of the external source and the detector, but since it was shown in the previous chapter that source and detector locations do not affect the response as long as they are not centrally placed, this is not expected to negatively impact the measurements. The detector will be located on the upper assembly slightly off from center next to the bridge support structure. The neutron source, either PoBe or AmBe, will be placed on the concave inner surface of the lower assembly. The three configurations detailed earlier will be measured. The separation distances at which measurements will be taken are 2.5, 5, 7.5 and 10 cm.

The Rocky Flats Shells experiments are scheduled for either late 2017 or early 2018. These measurements will validate the predictive capabilities of the computational method for asymmetrical systems developed in this research. The complex geometry and high neutron leakage will test various aspects of this method, particularly the determination of the faster prompt neutron decay constant from a curve fit to the Rossi-alpha histogram. The minimum count rate and total number of counts needed to observe the true prompt neutron decay constants need to be determined.

In light of the observation from the simulation results that the helium-3 detection system may not be fast enough for these measurements, simulations involving scintillation detectors will be conducted. Scintillation detectors tend to have a much smaller resolution than proportional counters and are therefore more appropriate for measuring fast, bare metal systems.

The Legendre-space transform method for nonlinear least squares fitting will be explored further. This appears to be a promising method that is not only less computationally intensive, but also provides better estimates of the fit parameters than traditional methods in many situations. The fact that initial guesses for the parameters are not needed makes it even more appealing for Rossi-alpha analysis. The reason for the oscillations in some of the fits to the Rossi-alpha histograms will be studied. Additionally, a goodness-of-fit assessment for the fitted models will be applied.

Appendices

Appendix A

Analytical Solution of the Two-Region Kinetics Equations for an Asymmetrical System

The solution of the two-region kinetics equations for an asymmetrical system is shown here.

The general point kinetics equations for a loosely-coupled two-region system ignoring delayed neutrons, external source and transit time are:

$$\frac{dn_1(t)}{dt} = \alpha_1 n_1(t) + \gamma_{12} n_2(t)$$
$$\frac{dn_2(t)}{dt} = \alpha_2 n_2(t) + \gamma_{21} n_2(t)$$

(A.1)

The parameters were defined in Chapter 2. The Laplace transform method was used in Chapter 2 to obtain the equations for the prompt neutron decay constants; here the matrix method will be used. The equations can be rewritten as:

$$\frac{d}{dt} \begin{bmatrix} n_1(t) \\ n_2(t) \end{bmatrix} = \begin{bmatrix} \alpha_1 & \gamma_{12} \\ \gamma_{21} & \alpha_2 \end{bmatrix} \begin{bmatrix} n_1(t) \\ n_2(t) \end{bmatrix}$$

(A.2)

First, the eigenvalues of the equations are found by solving the determinant of the coefficient matrix:

$$det \begin{bmatrix} \alpha_1 - \lambda & \gamma_{12} \\ \gamma_{21} & \alpha_2 - \lambda \end{bmatrix} = 0$$

(A.3)

$$(\alpha_1 - \lambda)(\alpha_2 - \lambda) - \gamma_{12}\gamma_{21} = 0 \tag{A.4}$$

$$\alpha_1\alpha_2 - (\alpha_1 + \alpha_2)\lambda + \lambda^2 - \gamma_{12}\gamma_{21}$$

Solving for the roots:

$$\lambda_{1,2} = \frac{1}{2}(\alpha_1 + \alpha_2) \pm \frac{1}{2}\sqrt{(-(\alpha_1 + \alpha_2))^2 - 4(\alpha_1\alpha_2 - \gamma_{12}\gamma_{21})}$$

$$\lambda_{1,2} = \frac{1}{2}(\alpha_1 + \alpha_2) \pm \frac{1}{2}\sqrt{(\alpha_1 - \alpha_2)^2 + 4\gamma_{12}\gamma_{21}} \tag{A.5}$$

The roots, again, are the slower and the faster prompt neutron decay constants, α_S and α_F. Replacing λ with α_S and solving for the eigenvectors:

$$\begin{bmatrix} \alpha_1 - \alpha_S & \gamma_{12} \\ \gamma_{21} & \alpha_2 - \alpha_S \end{bmatrix} \begin{bmatrix} \eta_1 \\ \eta_2 \end{bmatrix} = \begin{bmatrix} 0 \\ 0 \end{bmatrix} \tag{A.6}$$

$$(\alpha_1 - \alpha_S)\,n_1 + \gamma_{12}n_2 = 0$$

$$\gamma_{21}n_1 + (\alpha_2 - \alpha_S)\,n_2 = 0 \tag{A.7}$$

Only one equation needs to be solved to find the eigenvectors. Solving the first equation:

$$\eta_1 = \frac{\gamma_{12}}{\lambda_S - \alpha_1}\eta_2 \tag{A.8}$$

$$\vec{\eta} = \begin{bmatrix} \dfrac{\gamma_{12}}{\alpha_S - \alpha_1}\eta_2 \\ \eta_2 \end{bmatrix} \rightarrow \vec{\eta}^{(1)} = \begin{bmatrix} \dfrac{\gamma_{12}}{\alpha_S - \alpha_1} \\ 1 \end{bmatrix}, \eta_2 = 1 \tag{A.9}$$

The eigenvector for α_F is similarly found:

$$\vec{\eta} = \begin{bmatrix} \dfrac{\gamma_{12}}{\alpha_F - \alpha_1}\eta_2 \\ \eta_2 \end{bmatrix} \rightarrow \vec{\eta}^{(2)} = \begin{bmatrix} \dfrac{\gamma_{12}}{\alpha_F - \alpha_1} \\ 1 \end{bmatrix}, \eta_2 = 1 \tag{A.10}$$

The general solution is then written as

$$\vec{n}(t) = C_1 e^{\alpha_S t} \begin{bmatrix} \dfrac{\gamma_{12}}{\alpha_S - \alpha_1} \\ 1 \end{bmatrix} + C_2 e^{\alpha_F t} \begin{bmatrix} \dfrac{\gamma_{12}}{\alpha_F - \alpha_1} \\ 1 \end{bmatrix} \tag{A.11}$$

To find the coefficients C_1 and C_2, the initial conditions are applied:

$$\begin{bmatrix} n_{1,0} \\ n_{2,0} \end{bmatrix} = \vec{n}(0) = C_1 \begin{bmatrix} \dfrac{\gamma_{12}}{\alpha_S - \alpha_1} \\ 1 \end{bmatrix} + C_2 \begin{bmatrix} \dfrac{\gamma_{12}}{\alpha_F - \alpha_1} \\ 1 \end{bmatrix} \tag{A.12}$$

$$n_{1,0} = \frac{\gamma_{12}}{\alpha_S - \alpha_1} C_1 + \frac{\gamma_{12}}{\alpha_F - \alpha_1} C_2$$

$$\tag{A.13}$$

$$n_{2,0} = C_1 + C_2$$

Solving for C_1 and C_2:

$$C_1 = \frac{\dfrac{\gamma_{12}}{\alpha_F - \alpha_1} n_{2,0} - n_{1,0}}{\dfrac{\gamma_{12}}{\alpha_F - \alpha_1} - \dfrac{\gamma_{12}}{\alpha_S - \alpha_1}}$$

$$\tag{A.14}$$

$$C_2 = \frac{n_{1,0} - \dfrac{\gamma_{12}}{\alpha_S - \alpha_1} n_{2,0}}{\dfrac{\gamma_{12}}{\alpha_F - \alpha_1} - \dfrac{\gamma_{12}}{\alpha_S - \alpha_1}}$$

Setting $A = \alpha_S - \alpha_1$, $B = \alpha_F - \alpha_1$, and $D = \alpha_S - \alpha_F$, the coefficients become

$$C_1 = \frac{A}{D}\left(n_{2,0} - \frac{B}{\gamma_{12}} n_{1,0}\right)$$

$$\tag{A.15}$$

$$C_2 = \frac{B}{D}\left(\frac{A}{\gamma_{12}} n_{1,0} - n_{2,0}\right)$$

The solutions to the coupled kinetics equations for an asymmetrical system are thus:

$$\vec{n}\left(t\right) = \frac{A}{D}\left(n_{2,0} - \frac{B}{\gamma_{12}}n_{1,0}\right)e^{\alpha_S t}\begin{bmatrix}\frac{\gamma_{12}}{A}\\1\end{bmatrix} + \frac{B}{D}\left(\frac{A}{\gamma_{12}}n_{1,0} - n_{2,0}\right)e^{\alpha_F t}\begin{bmatrix}\frac{\gamma_{12}}{B}\\1\end{bmatrix} \qquad \text{(A.16)}$$

$$n_1\left(t\right) = \frac{\gamma_{12}}{D}\left[\left(n_{2,0} - \frac{B}{\gamma_{12}}n_{1,0}\right)e^{\alpha_S t} - \left(n_{2,0} - \frac{A}{\gamma_{12}}n_{1,0}\right)e^{\alpha_F t}\right] \qquad \text{(A.17)}$$

$$n_2\left(t\right) = \frac{A}{D}\left(n_{2,0} - \frac{B}{\gamma_{12}}n_{1,0}\right)e^{\alpha_S t} - \frac{B}{D}\left(n_{2,0} - \frac{A}{\gamma_{12}}n_{1,0}\right)e^{\alpha_F t} \qquad \text{(A.18)}$$

Appendix B

Derivation of the Rossi-alpha Equation for an Asymmetrical System

The derivation for the Rossi-alpha autocorrelation equation for an asymmetrical system shown in Equation 3.12 is shown here.

Setting $n_{1,0} = n_0$ and $n_{2,0} = 0$, Equation A.17 becomes

$$n_1\left(t\right) = \frac{A}{D}n_0 e^{\alpha_F t} - \frac{B}{D}n_0 e^{\alpha_S t} \tag{B.1}$$

Following the same method outlined in Chapter 3, the probability for a count in t_1 about dt_1 is

$$p\left(t_1\right)dt_1 = \frac{\epsilon}{\tau_f}\left[\frac{A}{D}n_0 e^{\alpha_F(t_1-t_0)} - \frac{B}{D}n_0 e^{\alpha_S(t_1-t_0)}\right] \tag{B.2}$$

and the probability for a count at t_2 about dt_2 is

$$p\left(t_2\right)dt_2 = \frac{\epsilon}{\tau_f}\left[\frac{A}{D}n_0 e^{\alpha_F(t_2-t_0)} - \frac{B}{D}n_0 e^{\alpha_S(t_2-t_0)}\right] \tag{B.3}$$

If at t_1, $n_0 = \nu$ and at t_2, $n_0 = \nu - 1$, then the equations become

$$p\left(t_1\right)dt_1 = \frac{\epsilon\nu}{\tau_f D}\left[Ae^{\alpha_F(t_1-t_0)} - Be^{\alpha_S(t_1-t_0)}\right] \tag{B.4}$$

$$p\left(t_2\right)dt_2 = \frac{\epsilon\left(\nu-1\right)}{\tau_f D}\left[Ae^{\alpha_F(t_2-t_0)} - Be^{\alpha_S(t_2-t_0)}\right] \tag{B.5}$$

The product of $p(t_0)$, $p(t_1)$ and $p(t_2)$ is

$$p(t_0)\, p(t_1)\, p(t_2)\, dt_0 dt_1 dt_2$$
$$= \frac{\dot{F}\epsilon^3 \nu (\nu - 1)}{\tau_f^2 D^2} \left(Ae^{\alpha_F(t_1 - t_0)} - Be^{\alpha_S(t_1 - t_0)} \right) \left(Ae^{\alpha_F(t_2 - t_0)} - Be^{\alpha_S(t_2 - t_0)} \right) dt_1 dt_2 \qquad \text{(B.6)}$$

Multiplying the exponential terms:

$$A^2 e^{\alpha_F(t_1 - t_0) + \alpha_S(t_2 - t_0)} - ABe^{\alpha_S(t_1 - t_0) + \alpha_F(t_2 - t_0)}$$
$$- ABe^{\alpha_F(t_1 - t_0) + \alpha_S(t_2 - t_0)} + B^2 e^{\alpha_S(t_1 - t_0) + \alpha_S(t_2 - t_0)} \qquad \text{(B.7)}$$

Next, Equation B.6 is integrated with respect to t_0 from $-\infty$ to t_1 and averaged over the neutron fission emission distribution. The integral is

$$\int_{-\infty}^{t_1} [A^2 e^{\alpha_F(t_1 + t_2 - 2t_0)} - ABe^{\alpha_S t_1 + \alpha_F t_2 - t_0(\alpha_F + \alpha_S)}$$
$$- ABe^{\alpha_F t_1 + \alpha_S t_2 - t_0(\alpha_F + \alpha_S)} + B^2 e^{\alpha_S(t_1 + t_2 - 2t_0)}] dt_0 \qquad \text{(B.8)}$$

which becomes upon integrating,

$$-\frac{A^2}{2\alpha_F} e^{\alpha_F(t_2 - t_1)} + \frac{AB}{\alpha_F + \alpha_S} e^{\alpha_F(t_2 - t_1)} + \frac{AB}{\alpha_F + \alpha_S} e^{\alpha_S(t_2 - t_1)} - \frac{B^2}{2\alpha_S} e^{\alpha_S(t_2 - t_1)} \qquad \text{(B.9)}$$

Grouping the integration results, plugging it back into the original probability equation and setting $t_1 = 0$ and $t_2 = t$,

$$\epsilon \dot{F}_0 p(t)\, dt = \frac{\epsilon^2 \dot{F}_0 \overline{\nu (\nu - 1)}}{4\tau_f^2 D^2} \left[\left(\frac{AB}{\alpha_F + \alpha_S} - \frac{A^2}{2\alpha_F} \right) e^{\alpha_F t} + \left(\frac{AB}{\alpha_F + \alpha_S} - \frac{B^2}{2\alpha_S} \right) e^{\alpha_S t} \right] dt \quad \text{(B.10)}$$

And then solving for $p(t)\, dt$ and including a term, Cdt, for the accidental neutron correlations:

$$p(t)\, dt = Cdt + \frac{\epsilon \overline{\nu (\nu - 1)}}{4\tau_f^2 D^2} \left[\left(\frac{AB}{\alpha_F + \alpha_S} - \frac{A^2}{2\alpha_F} \right) e^{\alpha_F t} + \left(\frac{AB}{\alpha_F + \alpha_S} - \frac{B^2}{2\alpha_S} \right) e^{\alpha_S t} \right] dt \quad \text{(B.11)}$$

Appendix C

MPKRA Python Code

MPKRA.py main code. See Ref. [65] for the Legendre transform and curve fit expfit source code.

```python
#!/usr/bin/env python

# Rossi-alpha analysis of list-mode data
import numpy as np
import matplotlib.pyplot as plt
# traditional nonlinear least squares fitting
from lmfit import minimize, Parameters, report_fit
# Conversion to Legendre polynomials + nonlinear LSQ fitting
from expfit import expfit
from Binning import binning
from scipy.optimize import curve_fit
from textwrap import wrap


if __name__ == '__main__':

    filename = raw_input("Enter list-mode filename: ")
    output_filename = raw_input("Enter desired output filename: ")

    while True:
        try:
            method = int(raw_input("Enter 1 for single time bin
                width analysis. Enter 2 for multiple time bin
                width analysis: "))
            if method == 1:
                break
            if method == 2:
                break
```

```python
        except ValueError:
            print "Value needs to be either 1 or 2."
while True:
    try:
        count_time = float(raw_input("Enter total count time
            of problem in seconds: "))
        count_time = count_time * 10**6
        break
    except ValueError:
        print "Count time must be a numerical value."
while True:
    try:
        observation_window = float(raw_input("Enter the desired
            observation window in microseconds: "))
        break
    except ValueError:
        print "Time window must be a numerical value."
if method == 1:
    while True:
        try:
            bin_width = float(raw_input("Enter the desired time
                bin width in microseconds: "))
            break
        except ValueError:
            print "Time bin width must be a numerical value."
while True:
    try:
        number_exponentials = int(raw_input("Enter the number
            of exponentials desired for the data fit: "))
        break
    except ValueError:
        print "This must be a positive integer greater than
            zero."


def single_exponential(t,A0,A1,alpha1):
    return A0 + A1*np.exp(alpha1*t)

def double_exponential(t,A0,A1,alpha1,A2,alpha2):
    return A0 + A1*np.exp(alpha1*t) + A2*np.exp(alpha2*t)

def triple_exponential(t,A0,A1,A2,A3,alpha1,alpha2,alpha3):
    return A0 + A1*np.exp(alpha1*t) + A2*np.exp(alpha2*t)
        + A3*np.exp(alpha3*t)
```

```python
# process input file
time_list = []
with open(filename) as file:
    lines = [line.split() for line in file]
    lines_sorted = sorted(lines, key=lambda row: float(row[1]))
    for line in lines_sorted:
        time_shakes = float(line[1])
        time_usec = time_shakes * .01
        if (time_usec > count_time):
            break
        else:
            time_list.append(time_usec)
time = np.asarray(time_list)

# analyze set of time bin widths

delta_t, num_seq = binning(time,observation_window,count_time)
print "number of sequences: ", num_seq


# histogram
number_windows = int(count_time / observation_window)
print "number of observation windows", number_windows


if method == 1:

    number_bins = int(observation_window / bin_width)
    print "number of observation windows", number_windows
    print "number of bins per window", number_bins
    hist, bin_edges = np.histogram(delta_t, number_bins)
    print "histogram array", hist
    print "bin edges", bin_edges

    # Nonlinear LSQ fitting

    m = 40  # number of Legendre polynomial modes
    t = np.linspace(0,observation_window,number_bins)
    x = np.linspace(-1,1,number_bins)


    bin_centers = []
    for i in range(len(bin_edges)-1):
        bin_centers.append(bin_edges[i+1] - bin_edges[i])
```

```
# Legendre polynomial fitting
print "length of t", len(t)
fit = expfit(t,m,number_exponentials)
a0 = np.ones(number_exponentials+1)

print "length of histogram", len(hist)
A,B,alpha,aopt = fit.getOptCoeffs(hist,a0)
y = fit.getCurrentState()
s = fit.getStandardError(number_bins,hist,y)

# scipy curve_fit fitting
if number_exponentials == 1:
    popt, pcov = curve_fit(single_exponential, t, hist,
        p0=[A,B[0],alpha[0]])
if number_exponentials == 2:
    popt, pcov = curve_fit(double_exponential, t, hist,
        p0=[A,B[0],alpha[0],B[1],alpha[1]], maxfev=10000)
if number_exponentials == 3:
    popt, pcov = curve_fit(triple_exponential, t, hist,
        p0=[A,B[0],alpha[0],B[1],alpha[1],B[2],alpha[2]],
        maxfev=100000)
print "covariance matrix", pcov

N = len(bin_edges)

# ACTUAL mean and variance for Rossi-alpha distribution
background_counts = A  # counts PER HIST BAR
# subtract background counts from histogram
net_counts = []
time_sep_prob_i = []
x_i = []
mean_separation_time = 0
sum_net_counts = 0
total_prob = 0
for i in range(N-1):
    net_counts.append(hist[i] - background_counts)
    if net_counts[i] <= 0:
        net_counts[i] = 0
    sum_net_counts = sum_net_counts + net_counts[i]
for i in range(N-1):
    time_sep_prob_i.append(net_counts[i] / sum_net_counts)
    total_prob = total_prob + time_sep_prob_i[i]
    x_i.append(bin_edges[i+1] * bin_width)
```

```
        mean_separation_time = mean_separation_time + x_i[i]
            * time_sep_prob_i[i]
print "mean separation time is ", mean_separation_time,
        "microseconds"
# ACTUAL variance
variance_rossi = 0
for i in range(N-1):
    variance_rossi = variance_rossi + ((x_i[i] -
        mean_separation_time)**2) * time_sep_prob_i[i]
print "variance is ", variance_rossi, "microseconds"



# error calculations
perr = np.sqrt(np.diag(pcov))
# standard error of the estimate ("goodness of fit"
    determination)
sum_y_diff_sq = 0

if number_exponentials == 1:
    for i in range(N-1):
        y_i = hist[i]
        y_fit_i = popt[0]+popt[1]*np.exp(popt[2]
            *bin_edges[i])
        sum_y_diff_sq = sum_y_diff_sq + (y_i - y_fit_i)**2
if number_exponentials == 2:
    for i in range(N-1):
        y_i = hist[i]
        y_fit_i = popt[0]+popt[1]*np.exp(popt[2]
            *bin_edges[i])+popt[3]*np.exp(popt[4]
            *bin_edges[i])
        sum_y_diff_sq = sum_y_diff_sq + (y_i - y_fit_i)**2
if number_exponentials == 3:
    for i in range(N-1):
        y_i = hist[i]
        y_fit_i = popt[0]+popt[1]*np.exp(popt[2]
            *bin_edges[i])+popt[3]*np.exp(popt[4]
            *bin_edges[i])+popt[5]*np.exp(popt[6]
            *bin_edges[i])
        sum_y_diff_sq = sum_y_diff_sq + (y_i - y_fit_i)**2
std_err_curve_fit = np.sqrt(sum_y_diff_sq / N)



# report results to terminal window
np.set_printoptions(formatter={'float': lambda x:
    format(x, '6.4E')})
```

```python
print "time window size: ", observation_window,
    "microseconds"
print "time bin width: ", bin_width, "microseconds"
print "measurement time: ", int(count_time / 10**6),
    "seconds"
print "total number of counts recorded: ",
    len(time_list)
cps = len(time_list) / (count_time / 10**6)
print "average count rate: ", cps, "counts per second"
inv_cps = 1 / cps
print "inverse counts per second: ", inv_cps

if number_exponentials == 1:
    print "Scipy curve_fit best parameters
        (+/- 1 sigma): "
    print "A0: ", popt[0], "+/-", perr[0]
    print "A1: ", popt[1], "+/-", perr[1]
    print "alpha1: ", popt[2], "+/-", perr[2], "/usec"
    print "alpha1 (in inverse seconds): ", popt[2]
        * 10**6
    print "Standard error of the curve_fit fit is: ",
        std_err_curve_fit, "counts."

    print "Legendre polynomial fitting best
        parameters:"
    print "A0: ", A
    print "A1: ", B[0]
    print "alpha1: ", alpha[0], "/usec"
    print "Standard error of the Legendre-sapce fit
        is: ", s, "counts."

if number_exponentials == 2:
    print "Scipy curve_fit best parameters
        (+/- 1 sigma): "
    print "A0: ", popt[0], "+/-" , perr[0]
    print "A1: ", popt[1], "+/-", perr[1]
    print "A2: ", popt[3], "+/-", perr[3]
    print "alpha1: ", popt[2], "+/-", perr[2], "/usec"
    print "alpha2: ", popt[4], "+/-", perr[4], "/usec"
    print "Standard error of the curve_fit: ",
        std_err_curve_fit, "counts."

    print "Legendre polynomial fitting best parameters:"
    print "A0: ", A
```

```
        print "A1: ", B[0]
        print "A2: ", B[1]
        print "alpha1: ", alpha[0], "/usec"
        print "alpha2: ", alpha[1], "/usec"
        print "Standard error of the Legendre-space fit
            is: ", s, "counts."


    if number_exponentials == 3:
        print "Scipy curve_fit best parameters
            (+/- 1 sigma): "
        print "A0: ", popt[0], "+/-" , perr[0]
        print "A1: ", popt[1], "+/-", perr[1]
        print "A2: ", popt[3], "+/-", perr[3]
        print "A3: ", popt[5], "+/-", perr[5]
        print "alpha1: ", popt[2], "+/-", perr[2], "/usec"
        print "alpha2: ", popt[4], "+/-", perr[4], "/usec"
        print "alpha3: ", popt[6], "+/-", perr[6], "/usec"
        print "Standard error of the curve_fit fit is: ",
            std_err_curve_fit, "counts."


        print "Legendre polynomial fitting best parameters:"
        print "A0: ", A
        print "A1: ", B[0]
        print "A2: ", B[1]
        print "A3: ", B[2]
        print "alpha1: ", alpha[0], "/usec"
        print "alpha2: ", alpha[1], "/usec"
        print "alpha3: ", alpha[2], "/usec"
        print "Standard error of the Legendre-space fit
            is: ", s, "counts."


# PLOTS
plt.title(r'Rossi-$\alpha$ histogram', fontsize=16)
plt.bar(bin_edges[:-1], hist, width=bin_width)
if number_exponentials == 1:
    plt.plot(t,single_exponential(t,popt[0],popt[1],
        popt[2]), 'r-', lw=2)
if number_exponentials == 2:
    plt.plot(t,double_exponential(t,popt[0],popt[1],
        popt[2],popt[3],popt[4]), 'r-', lw=2)
plt.xlim(0.0,observation_window)
plt.xlabel('time (microseconds)')
plt.ylim(0.0, max(hist)+10)
plt.ylabel('counts')
plt.show()
```

```python
if method == 2:

    file = open("%s" % output_filename, "w")
    if number_exponentials == 1:
        file.write("%-8s %16s %16s\n" %("bin size","alpha 1",
            "error"))

    if number_exponentials == 2:
        file.write("%-8s %16s %16s %16s %16s\n" %("bin size",
            "alpha 1","error","alpha 2","error"))

    if number_exponentials == 3:
        file.write("%-8s %16s %16s %16s %16s %16s\n"
            %("bin size","alpha 1","error","alpha 2","error",
            "alpha 3","error"))

    for bin_width in np.arange(1, 0.001, -0.005):
        print "bin width", bin_width
        number_bins = int(observation_window / bin_width)
        hist, bin_edges = np.histogram(delta_t, number_bins)

        m = 40  # number of Legendre polynomial modes
        t = np.linspace(0,observation_window,number_bins)
        x = np.linspace(-1,1,number_bins)


        bin_centers = []
        for i in range(len(bin_edges)-1):
            bin_centers.append(bin_edges[i+1] - bin_edges[i])


        # Legendre polynomial fitting
        print "length of t", len(t)
        fit = expfit(t,m,number_exponentials)
        a0 = np.ones(number_exponentials+1)

        print "length of histogram", len(hist)
        A,B,alpha,aopt = fit.getOptCoeffs(hist,a0)
        y = fit.getCurrentState()
        s = fit.getStandardError(number_bins,hist,y)


        # scipy curve_fit fitting
        if number_exponentials == 1:
```

```python
        popt, pcov = curve_fit(single_exponential, t,
            hist, p0=[A,B[0],alpha[0]])
    if number_exponentials == 2:
        popt, pcov = curve_fit(double_exponential, t,
            hist, p0=[A,B[0],alpha[0],B[1],alpha[1]],
            maxfev=100000000)
    if number_exponentials == 3:
        popt, pcov = curve_fit(triple_exponential, t,
            hist, p0=[A,B[0],alpha[0],B[1],alpha[1],
            B[2],alpha[2]],maxfev=100000)


N = len(bin_edges)

# error calculations
perr = np.sqrt(np.diag(pcov))
# print "curve_fit error", perr
# standard error of the estimate ("goodness of fit"
      determination)
sum_y_diff_sq = 0

if number_exponentials == 1:
    for i in range(N-1):
        y_i = hist[i]
        y_fit_i = popt[0]+popt[1]*np.exp(popt[2]
            *bin_edges[i])
        sum_y_diff_sq = sum_y_diff_sq
            + (y_i - y_fit_i)**2
if number_exponentials == 2:
    for i in range(N-1):
        y_i = hist[i]
        y_fit_i = popt[0]+popt[1]*np.exp(popt[2]
            *bin_edges[i])+popt[3]*np.exp(popt[4]
            *bin_edges[i])
        sum_y_diff_sq = sum_y_diff_sq
            + (y_i - y_fit_i)**2
if number_exponentials == 3:
    for i in range(N-1):
        y_i = hist[i]
        y_fit_i = popt[0]+popt[1]*np.exp(popt[2]
            *bin_edges[i])+popt[3]*np.exp(popt[4]
            *bin_edges[i])+popt[5]*np.exp(popt[6]
            *bin_edges[i])
        sum_y_diff_sq = sum_y_diff_sq
            + (y_i - y_fit_i)**2
std_err_curve_fit = np.sqrt(sum_y_diff_sq / N)
```

```python
# report results to terminal window
np.set_printoptions(formatter={'float': lambda x:
    format(x, '6.4E')})


print "time window size: ", observation_window,
    "microseconds"
print "time bin width: ", bin_width, "microseconds"
print "measurement time: ", int(count_time / 10**6),
    "seconds"
print "total number of counts recorded: ",
    len(time_list)
cps = len(time_list) / (count_time / 10**6)
print "average count rate: ", cps, "counts per second"
inv_cps = 1 / cps
print "inverse counts per second: ", inv_cps


if number_exponentials == 1:
    print "Scipy curve_fit best parameters
        (+/- 1 sigma): "
    print "A0: ", popt[0], "+/-", perr[0]
    print "A1: ", popt[1], "+/-", perr[1]
    print "alpha1: ", popt[2], "+/-", perr[2], "/usec"
    print "Standard error of the curve_fit fit is: ",
        std_err_curve_fit, "counts."

    print "Legendre polynomial fitting best
        parameters:"
    print "A0: ", A
    print "A1: ", B[0]
    print "alpha1: ", alpha[0], "/usec"
    print "Standard error of the Legendre-sapce fit
        is: ", s, "counts."


if number_exponentials == 2:
    print "Scipy curve_fit best parameters
        (+/- 1 sigma): "
    print "A0: ", popt[0], "+/-" , perr[0]
    print "A1: ", popt[1], "+/-", perr[1]
    print "A2: ", popt[3], "+/-", perr[3]
    print "alpha1: ", popt[2], "+/-", perr[2], "/usec"
    print "alpha2: ", popt[4], "+/-", perr[4], "/usec"
```

```python
        print "Standard error of the curve_fit: ",
            std_err_curve_fit, "counts."

        print "Legendre polynomial fitting best
            parameters:"
        print "A0: ", A
        print "A1: ", B[0]
        print "A2: ", B[1]
        print "alpha1: ", alpha[0], "/usec"
        print "alpha2: ", alpha[1], "/usec"
        print "Standard error of the Legendre-space fit
            is: ", s, "counts."


    if number_exponentials == 3:
        print "Scipy curve_fit best parameters
            (+/- 1 sigma): "
        print "A0: ", popt[0], "+/-" , perr[0]
        print "A1: ", popt[1], "+/-", perr[1]
        print "A2: ", popt[3], "+/-", perr[3]
        print "A3: ", popt[5], "+/-", perr[5]
        print "alpha1: ", popt[2], "+/-", perr[2], "/usec"
        print "alpha2: ", popt[4], "+/-", perr[4], "/usec"
        print "alpha3: ", popt[6], "+/-", perr[6], "/usec"
        print "Standard error of the curve_fit fit is: ",
            std_err_curve_fit, "counts."

        print "Legendre polynomial fitting best
            parameters:"
        print "A0: ", A
        print "A1: ", B[0]
        print "A2: ", B[1]
        print "A3: ", B[2]
        print "alpha1: ", alpha[0], "/usec"
        print "alpha2: ", alpha[1], "/usec"
        print "alpha3: ", alpha[2], "/usec"
        print "Standard error of the Legendre-space fit
            is: ", s, "counts."


    if number_exponentials == 1:
        file.write("%-8s %16s %16s\n" %(bin_width,popt[2]
            ,perr[2],))

    if number_exponentials == 2:
```

```python
        file.write("%-8s %16s %16s %16s %16s\n"
            %(bin_width,popt[2],perr[2],popt[4],perr[4]))

    if number_exponentials == 3:
        file.write("%-8s %16s %16s %16s %16s %16s %16s\n"
            %(bin_width,popt[2],perr[2],popt[4],perr[4],
            popt[6],perr[6]))


file.write("time window size: %s microseconds\n"
    %(observation_window))
msmt_time = int(count_time / 10**6)
file.write("measurement time: %s seconds\n" %(msmt_time))
total_counts = len(time_list)
file.write("total number of counts recorded: %s\n"
    %(total_counts))
cps = len(time_list) / (count_time / 10**6)
file.write("average count rate: %s counts per second\n"
    %(cps))
inv_cps = 1 / cps
file.write("inverse counts per second: %s\n" %(inv_cps))

file.close()
```

Binning.py subroutine

```python
#!/usr/bin/env python

import numpy as np
cimport numpy as np

def binning(np.ndarray[double, ndim=1] time,
      double time_bin_window,double count_time):

    '''
        This module imports the sorted time array/list and
        performs the Rossi-alpha time binning. It returns
        the Rossi-alpha histogram.

        '''
    delta_t_hist = []
    cdef:
        double t1, t2
        int i, j, m, n, count
    count = 0
    n = len(time)
    for i in range(n):
        t1 = time[i]
        if (t1+time_bin_window > count_time):
            break
        else:
            m = i+1
            if (m >= n):
                break
            t2 = time[m]
            while (t2-t1 <= time_bin_window and m < n):
                delta_t_hist.append(t2-t1)
                m += 1
                if (m >= n):
                    break
                t2 = time[m]
                count += 1
        print "test 1", count
    print "test 2", count
    return (delta_t_hist, count)
```

Appendix D

`MCNP 6` Input File - Rocky Flats Shells

Input file for the Rocky Flats Shells asymmetrical 33-63 configuration.

```
Rocky Flats Shells 33-63
c @@@   options = -mcnp "mcnpexe -6"
c @@@   options = -msub_opts "-l walltime=8:00:00"
c @@@   options = -ppn 16
c @@@    RNSEED = (2*int(rand(100000000000))+1)
c @@@    CNTTME = 1000
c @@@ SHCNTTME = (CNTTME * 1e8)
c @@@     CASES = 400
c @@@       NPS = (int((CNTTME * 1e7)/CASES))
c @@@    REPEAT = repeat CASES
c
c
c Rocky Flats Shells - 32 shells (16 per half)
c  Assembly lower-half (odd-numbered shells)
3030   0                      -3030  -5000     $ Void
3031   30  -18.675   3030  -3031  -5000     $ Shell 33
3032   0                3031  -3032  -5000     $ Void
3033   30  -18.675   3032  -3033  -5000     $ Shell 35
3034   0                3033  -3034  -5000     $ Void
3035   30  -18.675   3034  -3035  -5000     $ Shell 37
3036   0                3035  -3036  -5000     $ Void
3037   30  -18.675   3036  -3037  -5000     $ Shell 39
3038   0                3037  -3038  -5000     $ Void
3039   30  -18.675   3038  -3039  -5000     $ Shell 41
3040   0                3039  -3040  -5000     $ Void
3041   30  -18.675   3040  -3041  -5000     $ Shell 43
3042   0                3041  -3042  -5000     $ Void
3043   30  -18.675   3042  -3043  -5000     $ Shell 45
3044   0                3043  -3044  -5000     $ Void
```

```
3045   30   -18.675   3044   -3045   -5000       $ Shell 47
3046   0                      3045   -3046   -5000       $ Void
3047   30   -18.675   3046   -3047   -5000       $ Shell 49
3048   0                      3047   -3048   -5000       $ Void
3049   30   -18.675   3048   -3049   -5000       $ Shell 51
3050   0                      3049   -3050   -5000       $ Void
3051   30   -18.675   3050   -3051   -5000       $ Shell 53
3052   0                      3051   -3052   -5000       $ Void
3053   30   -18.675   3052   -3053   -5000       $ Shell 55
3054   0                      3053   -3054   -5000       $ Void
3055   30   -18.675   3054   -3055   -5000       $ Shell 57
3056   0                      3055   -3056   -5000       $ Void
3057   30   -18.675   3056   -3057   -5000       $ Shell 59
3058   0                      3057   -3058   -5000       $ Void
3059   30   -18.675   3058   -3059   -5000       $ Shell 61
3060   0                      3059   -3060   -5000       $ Void
3061   30   -18.675   3060   -3061   -5000       $ Shell 63
c
c Assembly upper-half (even-numbered shells)
4030   0                              -4030   5000   u=2   $ Void
4031   30   -18.675   4030   -4031   5000   u=2   $ Shell 34
4032   0                      4031   -4032   5000   u=2   $ Void
4033   30   -18.675   4032   -4033   5000   u=2   $ Shell 36
4034   0                      4033   -4034   5000   u=2   $ Void
4035   30   -18.675   4034   -4035   5000   u=2   $ Shell 38
4036   0                      4035   -4036   5000   u=2   $ Void
4037   30   -18.675   4036   -4037   5000   u=2   $ Shell 40
4038   0                      4037   -4038   5000   u=2   $ Void
4039   30   -18.675   4038   -4039   5000   u=2   $ Shell 42
4040   0                      4039   -4040   5000   u=2   $ Void
4041   30   -18.675   4040   -4041   5000   u=2   $ Shell 44
4042   0                      4041   -4042   5000   u=2   $ Void
4043   30   -18.675   4042   -4043   5000   u=2   $ Shell 46
4044   0                      4043   -4044   5000   u=2   $ Void
4045   30   -18.675   4044   -4045   5000   u=2   $ Shell 48
4046   0                      4045   -4046   5000   u=2   $ Void
4047   30   -18.675   4046   -4047   5000   u=2   $ Shell 50
4048   0                      4047   -4048   5000   u=2   $ Void
4049   30   -18.675   4048   -4049   5000   u=2   $ Shell 52
4050   0                      4049   -4050   5000   u=2   $ Void
4051   30   -18.675   4050   -4051   5000   u=2   $ Shell 54
4052   0                      4051   -4052   5000   u=2   $ Void
4053   30   -18.675   4052   -4053   5000   u=2   $ Shell 56
4054   0                      4053   -4054   5000   u=2   $ Void
4055   30   -18.675   4054   -4055   5000   u=2   $ Shell 58
```

```
4056   0                   4055  -4056  5000  u=2   $ Void
4057   30  -18.675  4056  -4057  5000  u=2   $ Shell 60
4058   0                   4057  -4058  5000  u=2   $ Void
4059   30  -18.675  4058  -4059  5000  u=2   $ Shell 62
4062   0                  -601 (-5000:4059)  #7500  u=2   $ Void
c
c RF Shells - top
6000   0                  -604 fill=2
                          trcl (2.5 0.0 0.0)
c
c Detectors - upper half
c
7500  12  -1.0  -7510  u=2
c
c External Void Regions
8000   0                  -9000  (3061:5000)  #6000
8001   0                   9000

c Rocky Flats Shells
c Odd-numbered shells
3000   so  2.0126      $ IR - shell 3
3001   so  2.3371      $ OR - shell 3
3002   so  2.3475      $ IR - shell 5
3003   so  2.6696      $ OR - shell 5
3004   so  2.6800      $ IR - shell 7
3005   so  3.0035      $ OR - shell 7
3006   so  3.0127      $ IR - shell 9
3007   so  3.3352      $ OR - shell 9
3008   so  3.3437      $ IR - shell 11
3009   so  3.6697      $ OR - shell 11
3010   so  3.6798      $ IR - shell 13
3011   so  4.0025      $ OR - shell 13
3012   so  4.0168      $ IR - shell 15
3013   so  4.3381      $ OR - shell 15
3014   so  4.3457      $ IR - shell 17
3015   so  4.6697      $ OR - shell 17
3016   so  4.6786      $ IR - shell 19
3017   so  5.0045      $ OR - shell 19
3018   so  5.0173      $ IR - shell 21
3019   so  5.3372      $ OR - shell 21
3020   so  5.3464      $ IR - shell 23
3021   so  5.6692      $ OR - shell 23
3022   so  5.6794      $ IR - shell 25
3023   so  6.0027      $ OR - shell 25
3024   so  6.0113      $ IR - shell 27
```

```
3025    so  6.3346        $ OR - shell 27
3026    so  6.3451        $ IR - shell 29
3027    so  6.6707        $ OR - shell 29
3028    so  6.6784        $ IR - shell 31
3029    so  7.0025        $ OR - shell 31
3030    so  7.0060        $ IR - shell 33
3031    so  7.3296        $ OR - shell 33
3032    so  7.3417        $ IR - shell 35
3033    so  7.6658        $ OR - shell 35
3034    so  7.6824        $ IR - shell 37
3035    so  8.0027        $ OR - shell 37
3036    so  8.0128        $ IR - shell 39
3037    so  8.3364        $ OR - shell 39
3038    so  8.3462        $ IR - shell 41
3039    so  8.6683        $ OR - shell 41
3040    so  8.6782        $ IR - shell 43
3041    so  8.9996        $ OR - shell 43
3042    so  9.0095        $ IR - shell 45
3043    so  9.3328        $ OR - shell 45
3044    so  9.3418        $ IR - shell 47
3045    so  9.6667        $ OR - shell 47
3046    so  9.6771        $ IR - shell 49
3047    so  9.9999        $ OR - shell 49
3048    so 10.0119        $ IR - shell 51
3049    so 10.3340        $ OR - shell 51
3050    so 10.3445        $ IR - shell 53
3051    so 10.6696        $ OR - shell 53
3052    so 10.6743        $ IR - shell 55
3053    so 11.0009        $ OR - shell 55
3054    so 11.0113        $ IR - shell 57
3055    so 11.3348        $ OR - shell 57
3056    so 11.3439        $ IR - shell 59
3057    so 11.6660        $ OR - shell 59
3058    so 11.6765        $ IR - shell 61
3059    so 11.9987        $ OR - shell 61
3060    so 12.0108        $ IR - shell 63
3061    so 12.3358        $ OR - shell 63
c
c Even-numbered shells
4000    so  2.0126        $ IR - shell 4
4001    so  2.3377        $ OR - shell 4
4002    so  2.3473        $ IR - shell 6
4003    so  2.6698        $ OR - shell 6
4004    so  2.6791        $ IR - shell 8
4005    so  3.0027        $ OR - shell 8
```

```
4006    so   3.0123      $ IR - shell 10
4007    so   3.3351      $ OR - shell 10
4008    so   3.3440      $ IR - shell 12
4009    so   3.6698      $ OR - shell 12
4010    so   3.6801      $ IR - shell 14
4011    so   4.0024      $ OR - shell 14
4012    so   4.0162      $ IR - shell 16
4013    so   4.3376      $ OR - shell 16
4014    so   4.3463      $ IR - shell 18
4015    so   4.6698      $ OR - shell 18
4016    so   4.6783      $ IR - shell 20
4017    so   5.0039      $ OR - shell 20
4018    so   5.0128      $ IR - shell 22
4019    so   5.3358      $ OR - shell 22
4020    so   5.3458      $ IR - shell 24
4021    so   5.6693      $ OR - shell 24
4022    so   5.6790      $ IR - shell 26
4023    so   6.0015      $ OR - shell 26
4024    so   6.0121      $ IR - shell 28
4025    so   6.3344      $ OR - shell 28
4026    so   6.3441      $ IR - shell 30
4027    so   6.6696      $ OR - shell 30
4028    so   6.6792      $ IR - shell 32
4029    so   7.0030      $ OR - shell 32
4030    so   7.0098      $ IR - shell 34
4031    so   7.3338      $ OR - shell 34
4032    so   7.3428      $ IR - shell 36
4033    so   7.6665      $ OR - shell 36
4034    so   7.6711      $ IR - shell 38
4035    so   8.0027      $ OR - shell 38
4036    so   8.0075      $ IR - shell 40
4037    so   8.3292      $ OR - shell 40
4038    so   8.3443      $ IR - shell 42
4039    so   8.6680      $ OR - shell 42
4040    so   8.6764      $ IR - shell 44
4041    so   8.9995      $ OR - shell 44
4042    so   9.0104      $ IR - shell 46
4043    so   9.3329      $ OR - shell 46
4044    so   9.3432      $ IR - shell 48
4045    so   9.6683      $ OR - shell 48
4046    so   9.6775      $ IR - shell 50
4047    so  10.0001      $ OR - shell 50
4048    so  10.0104      $ IR - shell 52
4049    so  10.3336      $ OR - shell 52
4050    so  10.3427      $ IR - shell 54
```

```
4051    so 10.6685        $ OR - shell 54
4052    so 10.6773        $ IR - shell 56
4053    so 11.0013        $ OR - shell 56
4054    so 11.0112        $ IR - shell 58
4055    so 11.3315        $ OR - shell 58
4056    so 11.3444        $ IR - shell 60
4057    so 11.6670        $ OR - shell 60
4058    so 11.6785        $ IR - shell 62
4059    so 12.0015        $ OR - shell 62
c
c "slicing" plane
5000   px  0.0
c
c RF universe - upper shells
600    cx  8.50
601    so  35.0
602    px -0.5
603    px  9.00
604    rpp -0.5 15.0 -15.0 15.0 -15.0 15.0
c
7510 rpp  13.0015 14.0015  -3.0 3.0  -3.0 3.0
c
8000   so  20.0   $ universe boundaries
8001   pz  10.0
c
9000   so  100.0  $ outer limit of problem

mode n
nps NPS
imp:n 1.0 65r 0.0
c
sdef par=n pos=-13.3358 0.0 0.0  erg=4.5  tme=d1
c
si1  0  1000.0e8
sp1  0  1
c
c
ptrac file=bin write=all max=1000000000 event=ter
        filter=7500,icl
c
c He-3
m12    2003.80c   1.0
c
c Uranium metal - RF Shells (1971 isotopics)
m30   92234.80c   0.0102
```

```
       92235.80c    0.9316
       92236.80c    0.0047
       92238.80c    0.0535
c
rand gen=2 seed=RNSEED
cut:n 1000.0e8 j 0  $ run sim in analog mode - no VR
c
fmult 92233 data=1 shift=0 method=0
fmult 92234 data=1 shift=0 method=0
fmult 92235 data=1 shift=0 method=0
fmult 92236 data=1 shift=0 method=0
fmult 92238 data=1 shift=0 method=0
c
totnu
print
```

For the kcode calculations, the data cards are changed to the following:

```
mode n
c
kcode 1000000 1.0  50 250
ksrc -8.8 0.0 0.0
kopts kinetics=yes
c
imp:n 1.0 64r 0.0
c
f01:n  5000
fc01  Leakage into flat surface lower hemi
c01   0.0 1.0
c
f11:n  3030
fc11  Leakage into curved surface lower hemi
c11   0.0 1.0
c
f21:n  6000
fc21  Leakage into flat surface upper hemi
c21   0.0 1.0
c
f31:n  4030
fc31  Leakage into curved surface upper hemi
c31   0.0 1.0
c
f04:n (3031 3032 3033 3034 3035 3036 3037 3038
       3039 3040 3041 3042 3043 3044 3045 3046
       3047 3048 3049 3050 3051 3052 3053 3054
       3055 3056 3057 3058 3059 3060 3061)
fc04  Neutron population in lower hemi
fm04  (1 -2)
c
f14:n (4031 4032 4033 4034 4035 4036 4037 4038
       4039 4040 4041 4042 4043 4044 4045 4046
       4047 4048 4049 4050 4051 4052 4053 4054
       4055 4056 4057 4058 4059)
fc14  Neutron population in upper hemi
fm14  (1 -2)
c
c He-3
m12    2003.80c   1.0
c
c Uranium metal - RF Shells (1971 isotopics)
```

```
m30    92234.80c    0.0102
       92235.80c    0.9316
       92236.80c    0.0047
       92238.80c    0.0535
c
totnu
print
```

Bibliography

[1] J. T. Mihalczo, "Rossi-alpha and pulsed neutron measurements in subcritical coupled uranium-metal cylinders," in *Proceedings of the National Topical Meeting on Coupled Reactor Kinetics* (C. G. Chezem and W. H. Köhler, eds.), (Texas A&M University, College Station, Texas), pp. 484–505, American Nuclear Society, January 1967.

[2] R. E. Rothe, "Extrapolated experimental critical parameters of unreflected and steel-reflected massive enriched uranium metal spherical and hemispherical assemblies," Tech. Rep. INEEL/EXT-97-01401, Idaho National Engineering Laboratory, 1997.

[3] M. White, T. Cutler, T. Grove, W. Myers, and R. Sanchez, "IER 153: Measure the fission neutron spectrum shape using threshold activation detectors. CEDT phase-2 detailed design," Tech. Rep. LA-UR-14-27323, Los Alamos National Laboratory, 2014.

[4] *International Handbook of Evaluated Criticality Safety Benchmark Experiments*, vol. NEA/NSC/DOC(95)03/II. OECD-NEA, 2015.

[5] "National Nuclear Data Center." `https://www.nndc.bnl.gov/exfor/endf00.jsp`. Accessed: 2017-04-27.

[6] G. McKenzie, J. Goda, T. Grove, and R. Sanchez, "Characterization of a polyethylene moderated highly enriched uranium system," Tech. Rep. LA-UR-16-24587, Los Alamos National Laboratory, 2016.

[7] T. Kawai, "Coupled reactor kinetics, (II)," *Journal of Nuclear Science and Technology*, vol. 2, no. 8, pp. 285–295, 1965.

[8] W. M. Stacey, Jr., *Space-Time Nuclear Reactor Kinetics*. New York, New York: Academic Press, 1969.

[9] K. Obaidurrahman and O. P. Singh, "Spatial neutronic coupling aspects in nuclear reactors," *Nuclear Engineering and Design*, vol. 240, pp. 2755–2760, 2010.

[10] R. Avery, "Theory of coupled reactors," in *Proceedings of the Second International Conference on Peaceful Uses of Atomic Energy*, vol. 12, (Geneva, Switzerland), pp. 182–191, 1958.

[11] G. C. Baldwin, "Kinetics of a reactor composed of two loosely coupled cores," *Nuclear Science and Engineering*, vol. 6, pp. 320–327, 1959.

[12] R. G. Cockrell and R. B. Perez, "On the kinetic theory of spatial and spectral coupling of the reactor neutron field," in *Symposium on Neutron Dynamics and Control*, (Tucson, Arizona), April 5-7 1965.

[13] F. T. Adler, S. J. Gage, and G. C. Hopkins, "Spatial and spectral coupling effects in multicore reactor systems," in *Proceedings of the National Topical Meeting on Coupled Reactor Kinetics* (C. G. Chezem and W. H. Köhler, eds.), (Texas A&M University, College Station, Texas), pp. 521–556, American Nuclear Society, January 1967.

[14] M. Komata, "On the derivation of Avery's coupled reactor kinetics equations," *Nuclear Science and Engineering*, vol. 38, pp. 193–204, 1969.

[15] K. Kobayashi, "Rigorous derivation of nodal equations for coupled reactors," *Annals of Nuclear Energy*, vol. 18, no. 1, pp. 13–18, 1991.

[16] Y. Wang, S. Schunert, J. Ortensi, F. Gleicher, B. Baker, G. Youinou, M. DeHart, and R. Martineau, "Derivation of the point-kinetics parameters for the coupled reactors," *Transactions of the American Nuclear Society*, vol. 115, pp. 604–607, 2016.

[17] M. Komata, "An attempt of applying coupled reactor theory," in *Proceedings of the National Topical Meeting on Coupled Reactor Kinetics* (C. G. Chezem and W. H. Köhler, eds.), (Texas A&M University, College Station, Texas), pp. 129–153, American Nuclear Society, January 1967.

[18] P. R. Pluta, "Coupled-core kinetic behavior," in *AEC Symposium Series #7, Neutron Dynamics and Control* (D. L. Hetrick and L. E. Weaver, eds.), pp. 544–565, USAEC Division of Technical Information, 1966.

[19] R. L. Seale, "Coupled core reactors," Tech. Rep. LAMS-2967, Los Alamos Scientific Laboratory, 1964.

[20] G. E. Hansen, "Kinetics equation for a cluster of Rover reactors," Tech. Rep. LA-DC-10338, Los Alamos Scientific Laboratory, 1965.

[21] S. J. Gage, *Investigations of the dynamic behavior of coupled-core nuclear reactors*. PhD thesis, Purdue University, 1966.

[22] C. G. Chezem, G. H. Hansen, H. H. Helmick, and R. L. Seale, "The Los Alamos coupled reactor experience," Tech. Rep. LA-3494, Los Alamos Scientific Laboratory, 1967.

[23] C. G. Chezem and H. H. Helmick, "Pulsed neutron analysis in the Los Alamos coupled reactor experiment," Tech. Rep. LA-3263-MS, Los Alamos Scientific Laboratory, 1965.

[24] C. E. Cohn, "Reflected-reactor kinetics," *Nuclear Science and Engineering*, vol. 13, pp. 12–17, 1962.

[25] R. W. Keaten and C. W. Griffin, "Reflected reactor kinetics," Tech. Rep. NAA-SR-7263, Atomics International, 1963.

[26] G. D. Spriggs, R. D. Busch, and J. G. Williams, "Two-region kinetic model for reflected reactors," *Annals of Nuclear Energy*, vol. 24, no. 3, pp. 205–250, 1997.

[27] A. A. Wasserman, "A simple model for the effect of reflected neutrons upon reactor kinetics," Quarterly Technical Report - SPERT Project IDO-16606, Phillips Petroleum Company, 1960.

[28] U. Farinelli and N. Pacilio, "The bimodal decay of two pulsed-neutron-coupled cores of an organic-moderated and -reflected system," *Nuclear Science and Engineering*, vol. 36, pp. 39–46, 1969.

[29] F. C. Difilippo and R. M. Waldman, "The kinetics of a coupled two-core nuclear reactor," *Nuclear Science and Engineering*, vol. 61, pp. 60–71, 1976.

[30] N. Murata, Y. Yamane, and K. Nishina, "Derivation of Pal-Bell equations for two-point reactors, and its application to correlation measurements," *Annals of Nuclear Energy*, vol. 8, pp. 407–414, 1981.

[31] M. Edelmann, J. Ehrhardt, and W. Väth, "Investigations of the two-detector covariance method for the time measurement of coupled reactor kinetics parameters," *Annals of Nuclear Energy*, vol. 2, pp. 207–216, 1975.

[32] J.-L. Muñoz-Cobo, C. Berglöf, J. Peña, D. Villamarín, and V. Bournos, "Feynman-alpha and Rossi-alpha formulas with spatial and modal effects," *Annals of Nuclear Energy*, vol. 38, pp. 590–600, 2011.

[33] G. Kistner, "Rossi-alpha theory for assemblies with two prompt neutron groups," *Nukleonik*, vol. 7, no. 2, pp. 106–109, 1965.

[34] J. T. Mihalczo, "Prompt-neutron time behavior in delayed-critical coupled uranium-metal cylinders," in *Proceedings of the International Conference on Fast Critical Experiments and Their Analysis*, pp. 237–241, Argonne National Laboratory, October 1966.

[35] J. R. Harries, "Correlation and flux tilt measurements of coupled-core reactor assemblies," Tech. Rep. AAEC/E357, Australian Atomic Energy Commission, January 1976.

[36] F. R. N. McDonnell and M. J. Harris, "Pulsed-source experiments in a reflected coupled-core reactor - II. Core coupling measurements," *Journal of Nuclear Energy*, vol. 26, pp. 129–140, 1972.

[37] A. Belleni-Morante, "Effect of first-flight neutron on coupled reactor kinetics behaviour," *Journal of Nuclear Energy*, vol. 21, pp. 867–870, 1967.

[38] F. R. N. McDonnell and M. J. Harris, "Pulsed-source experiments in a reflected coupled-core reactor - I. Reactivity measurements," *Journal of Nuclear Energy*, vol. 26, pp. 113–128, 1972.

[39] A. E. Waltar and L. Ruby, "Pulsed-source reactivity measurements in a reflected reactor," *Nukleonik*, vol. 10, pp. 70–77, 1967.

[40] A. S. Tai and J. P. Schneeberger, "Neutron transit time measurements on a two-different-core system," *Annals of Nuclear Energy*, vol. 4, pp. 443–448, 1977.

[41] K. Hashimoto, R. Miki, T. Itoh, and T. Shibata, "Derivation of coupling coefficient from rod drop measurements in two-point reactors," *Annals of Nuclear Energy*, vol. 17, no. 12, pp. 667–672, 1990.

[42] E. Viehl, "Zero-power noise analysis in a reactor with two weakly coupled asymmetrical fission zones," *Nuclear Science and Engineering*, vol. 56, pp. 422–427, 1975.

[43] K. O. Ott and R. J. Neuhold, *Introductory Nuclear Reactor Dynamics*. La Grange Park, Illinois: American Nuclear Society, 1985.

[44] A. F. Henry, "The application of reactor kinetics to the analysis of experiments," *Nuclear Science and Engineering*, vol. 3, pp. 52–70, 1958.

[45] P. Bosio, P. Ravetto, M. M. Rostagno, and A. Barzilov, "Multipoint methods in nuclear reactor kinetics," in *ANS International Meeting on Mathematical Methods for Nuclear Applications*, American Nuclear Society, 2001.

[46] S. Dulla, P. Ravetto, M. Carta, and A. D'Angelo, "Kinetic parameters for source driven systems," in *PHYSOR-2006, ANS Topical Meeting on Reactor Physics*, American Nuclear Society, 2006.

[47] W. de Carvalho Gonçalves, A. S. Martinez, and F. C. da Silva, "Point kinetics equations for subcritical systems based on the importance function associated to an external neutron source," *Annals of Nuclear Energy*, vol. 79, pp. 1–8, 2015.

[48] A. Gandini and M. Salvatores, "The physics of subcritical multiplying systems," *Nuclear Science and Technology*, vol. 39, no. 6, pp. 673–686, 2002.

[49] B. E. Simmons and J. S. King, "A pulsed neutron technique for reactivity determination," *Nuclear Science and Engineering*, vol. 3, pp. 595–608, 1958.

[50] G. R. Keepin, *Physics of Nuclear Kinetics*. Reading, Massachusettes: Addison-Wesley, 1965.

[51] J. D. Orndoff, "Prompt neutron periods of metal critical assemblies," *Nuclear Science and Engineering*, vol. 2, pp. 450–460, 1957.

[52] F. de Hoffmann, "Statistical aspects of pile theory," in *The Science and Engineering of Nuclear Power* (C. Goodman, ed.), ch. 9, pp. 103–119, Cambridge: Addison-Wesley, 1949.

[53] R. Uhrig, *Random Noise Techniques in Nuclear Reactor Systems*. New York, New York: Ronald Press, 1970.

[54] T. J. Grove, "LLMM and NRDS: Los Alamos List Mode Module and Neutron Reference Detection System for He-3 and BF3 systems," Tech. Rep. LA-UR-14-21899, Los Alamos National Laboratory, 2014.

[55] G. E. Hansen, "The Rossi alpha method," Tech. Rep. LA-UR-85-4176, Los Alamos National Laboratory, 1985.

[56] N. Ensslin, "Principles of neutron coincidence counting," in *Passive Nondestructive Assay of Nuclear Materials* (D. Reilly, N. Ensslin, and J. Hastings Smith, eds.), ch. 16, pp. 457–491, Washington, D.C.: United States Nuclear Regulatory Commission, 1991.

[57] D. B. Pelowitz, A. J. Fallgren, and G. E. McMath, "MCNP6 user's manual: Code version 6.1.1 beta," Tech. Rep. LA-CP-14-00745, Los Alamos National Laboratory, 2014.

[58] K. Clark, J. Hutchinson, C. J. Solomon, T. Cutler, and A. Sood, "Characterization of the NPOD3 detectors in MCNP5 and MCNP6," *Transactions of the American Nuclear Society*, vol. 111, pp. 861–864, 2014.

[59] F. B. Brown, J. E. Sweezy, and R. B. Hayes, "Monte Carlo parameter studies and uncertainty analysis with MCNP5," Tech. Rep. LA-UR-04-0499, Los Alamos National Laboratory, 2004.

[60] C. J. Solomon, Jr., "The `mcnptools` package," Tech. Rep. LA-UR-14-27075, Los Alamos National Laboratory, 2014.

[61] "scipy.optimize.curve_fit." `https://docs.scipy.org/doc/scipy/reference/generated/scipy.optimize.curve_fit.html`. Accessed: 2016-09-13.

[62] G. Bao and D. Schild, "Fast and accurate fitting and filtering of noisy exponentials in Legendre space," *PLOS One*, vol. 9, 2014.

[63] R. D. Mosteller and B. C. Kiedrowski, "The Rossi-alpha validation suite for MCNP," Tech. Rep. LA-UR-11-5077, Los Alamos National Laboratory, 2011.

[64] G. F. Knoll, *Radiation Detection and Measurement, Second Edition*. New York, New York: John Wiley & Sons, 1989.

[65] G. von Winckel, "Fitting of data with exponential functions." `www.scientificpython.net/blog/fitting-of-data-with-exponential-functions`, 2013.

Curriculum Vitae

Graduate College
University of Nevada, Las Vegas

Kimberly Lynn Klain

Address:

Los Alamos National Laboratory
MS F663
PO Box 1663
Los Alamos, New Mexico 87545

Email:

kclark@lanl.gov

Degrees:

Master of Science, Materials and Nuclear Engineering, 2009
University of Nevada, Las Vegas

Bachelor of Science, Mechanical Engineering, 2006
University of Nevada, Las Vegas

Professional Memberships and Societies:

American Nuclear Society (ANS)
Tau Beta Pi Engineering Honors Society

Internships:

Varian Medical Systems, 2009
Idaho National Laboratory (Faculty-Student Research Team), 2010
Los Alamos National Laboratory, 2011-present

Publications:

K. Klain, "Simulated Rossi-alpha analysis of an asymmetrically coupled bare metal HEU reactor system," *Nuclear Criticality Safety Division Topical*, Carlsbad, NM, 2017 (accepted).

K. Clark, J. Hutchinson, C.J. Solomon, T. Cutler, A. Sood, "Characterization of the NPOD3 detectors in MCNP5 and MCNP6," *ANS Winter Meeting and ANS Transactions*, Anaheim, CA, 2014.

D. Beller, J. Bess, D. Lords, J. Boles, **K. Clark**, A. Santo Domingo, A. Lui, J. Mills, L. Lakeotes, C. Jackson, B. Chase, J.B. Briggs, F. Hua, "The UNLV ATRC criticality benchmark experiment project," *ANS Winter Meeting and ANS Transactions*, Washington, D.C., 2013.

K. Clark, A. Sood, J. Hutchinson, W. Myers, D. Beller, "Comparison of MCNP-based transport codes for subcritical calculations," *ANS Winter Meeting and ANS Transactions*, San Diego, CA, 2012.

J. Bess, M. Marshall, M. Gorham, J. Christensen, J. Turnbull, **K. Clark**, "Current reactor physics benchmark activities at the Idaho National Laboratory," *ANS Winter Meeting and ANS Transactions*, Washington, D.C., 2011.

K. Clark, D. Beller, A. Liu, L. Lakeotes, "Current status of NCSP Subtask 7 subcritical modeling," Nuclear Criticality Safety Program (NCSP) Subcritical Measurement Workshop, Los Alamos National Laboratory, Los Alamos, NM, 2011.

K. Clark, J. Bess, D. Beller, "Criticality validation and reactor physics experiment for the Advanced Test Reactor National Scientific User Facility," *The Materials Society Annual Meeting*, San Diego, CA, 2011.

J. Thota, **K. Clark**, T. Higgins, S. Nelson, B. O'Toole, "Fabrication and analysis of composite ducts for an unmanned aerial vehicle," *International SAMPE Symposium and Exhibition*, Seattle, WA, 2010.

J. Thota, **K. Clark**, B. O'Toole, "Quasistatic and vibration response of prototype composite ducts for aircraft components," *Proceedings of ICCE-17*, Honolulu, HI, 2009.

K. Clark, B. O'Toole, "Development of a prototype composite duct: A comparison of methods and materials," *Proceedings of ICCE-17*, Honolulu, HI, 2009.